




Cite this: *Dalton Trans.*, 2025, **54**, 9803

## Zeolitic imidazolate framework-67-derived chalcogenides as electrode materials for supercapacitors†

Lidong Jiao,<sup>a</sup> Mingshu Zhao,<sup>a</sup>  <sup>✉</sup> Qingyang Zheng,<sup>b</sup> Qingyi Ren,<sup>a</sup> Zhou Su,<sup>a</sup> Min Li<sup>a</sup> and Feng Li<sup>a</sup>

With the rapid development of new energy technologies, hybrid supercapacitors have received widespread attention owing to their advantages of high power density, fast charging/discharging rate and long cycle life. In this case, the selection and design of electrode materials are the key to improving the energy storage performance of supercapacitors. Herein, zeolitic imidazolate framework-67 (ZIF-67) is presented as a good candidate material for the fabrication of supercapacitor electrodes because of its controllable pore size, constant cavity size and large specific area. Moreover, pristine ZIF-67 and ZIF-67-derived porous carbon have shown exemplary performances in supercapacitors. However, they belong to the class of electric double layer capacitor materials and have a lower magnitude of energy storage compared with pseudocapacitor materials. Therefore, to improve the energy density of hybrid supercapacitors, other ZIF-67 derivatives need to be explored, especially chalcogenides. This review mainly reports the application of ZIF-67-derived transition metal chalcogenides (TMCs, C including Oxide, Sulfide, Selenide, Telluride) in supercapacitors. Moreover, the strategies for the preparation of ZIF-67-derived TMCs and their electrochemical performance in supercapacitors are further discussed. Finally, the remaining challenges and future perspectives are highlighted.

Received 23rd October 2024,  
Accepted 22nd April 2025

DOI: 10.1039/d4dt02957g

rsc.li/dalton

### 1. Introduction

With the continuous development of society and the economy, energy storage has become a key element in achieving energy sustainability goals, leading to energy and cost savings.<sup>1–3</sup> Thus, supercapacitors have attracted widespread attention from scientific researchers owing to their advantages of high power density, fast charging/discharging rate and long cycle life.<sup>4–9</sup> However, their relatively low energy density limits their further practical application.<sup>10–12</sup> Therefore, increasing research has been conducted on hybrid supercapacitors because of their charge-storage mechanisms, including both electric double layer capacitance and pseudocapacitance, resulting in better cycling stability than pseudocapacitors and higher energy density than electric double layer capacitors (EDLCs).<sup>13–18</sup> Moreover, there has been growing demand for

both high energy and high power densities in the same material.<sup>19–23</sup>

As a new class of porous crystal materials, metal organic frameworks (MOFs), which are composed of organic ligands and metal cations linked *via* coordination bonds, have been widely studied in the field of nanotechnology and energy storage because of their inherent advantages such as abundant porosity, high specific surface area and controllable topology.<sup>24–26</sup> Moreover, with the development of various synthetic strategies, many new MOFs with a specific topology or architecture have been manufactured and applied as supercapacitor electrode materials.<sup>27,28</sup> In recent years, an increasing number of MOFs have been used as templates or precursors to generate MOF derivatives, such as porous carbon,<sup>29</sup> metal-doped carbon, hydroxides, phosphides<sup>30</sup> and chalcogenides (O,<sup>31</sup> S,<sup>32</sup> Se,<sup>33</sup> and Te<sup>34</sup>). Furthermore, it has been proven that the size, shape and composition of MOF derivatives can be effectively controlled on the basis of their precursors.<sup>35,36</sup> Moreover, various conductive matrices (conductive polymers,<sup>37</sup> carbon-based materials<sup>38,39</sup> and MXene materials<sup>40,41</sup>) have been combined with pristine MOFs or MOF derivatives to improve their conductivity and structural stability during long-term cycling, resulting in promising cycling stability, better rate performance and high specific

<sup>a</sup>School of Physics, Key Laboratory of Shaanxi for Advanced Functional Materials and Mesoscopic Physics, MOE Key Laboratory for Non-equilibrium Synthesis and Modulation of Condensed Matter, Xi'an Jiaotong University, Xi'an, 710049 Shaanxi, China. E-mail: zhaomshu@mail.xjtu.edu.cn; Tel: +86-13186193932

<sup>b</sup>Xi'an High-tech Research Institute, 710025 Xi'an, China

† Electronic supplementary information (ESI) available. See DOI: <https://doi.org/10.1039/d4dt02957g>

capacitance/capacity.<sup>34</sup> However, some of these MOFs are unstable in water and alkaline solutions, which limit their use in supercapacitors.<sup>42</sup>

As a member of metal–organic frameworks, zeolitic imidazolate framework-67 (ZIF-67) is a good candidate material for the fabrication of supercapacitors (as shown in Fig. S1†) because of its controllable pore size, high chemical stability and thermal stability.<sup>43,44</sup> The ZIF-67 material (as shown in Fig. 1) is composed of imidazole and  $\text{Co}^{2+}$ , which can provide a large specific area and abundant oxidation active sites as an electrode material precursor, together with a constant cavity and thermal stability.<sup>45</sup> Thus, ZIF-67 has been considered as a promising electrode material for supercapacitors. For example, Xie *et al.*<sup>46</sup> successfully prepared one-dimensional ZIF-67, which exhibited a much higher charge storage capacity, rate capability and cycling stability than two-dimensional and three-dimensional ZIF-67 because of its abundant linker-missing defects and favorable exposure of cobalt ions as redox active sites. Moreover, due to the drawback of low conductivity of pristine ZIF-67, ZIF-67-derived porous carbon materials are also considered good EDLC materials for supercapacitors. Torad *et al.*<sup>47</sup> synthesized nanoporous carbon *via* the one-step direct carbonization of ZIF-67, which showed a good electrochemical performance of  $238 \text{ F g}^{-1}$  at  $20 \text{ mV s}^{-1}$  in  $0.5 \text{ M H}_2\text{SO}_4$  electrolyte. However, both pristine ZIF-67 (Table S1†) and ZIF-67-derived porous carbon (Table S2†) have a low energy density because they are EDLC materials. Therefore, it is necessary to develop new ZIF-67-derived pseudocapacitors materials to improve the energy density of hybrid supercapacitors.

As typical pseudocapacitor materials, transition metal chalcogenides (TMCs, C including O, S, Se, and Te) have been widely researched and applied in hybrid supercapacitors, exhibiting both high energy density and power density.<sup>34</sup> Thus, in this review, we focus on ZIF-67-derived TMCs as electrode

materials for application in supercapacitors. With the development of single-metal compounds to multi-metal compounds and composite materials, their preparation technology and electrochemical performances in supercapacitors are discussed to highlight the relevant challenges that need to be resolved in the future, enabling the research and development of high-performance materials. Furthermore, significantly, this review can guide the direction of future work based on the comparison of the electrochemical performance of various derivatives in supercapacitors.

## 2. ZIF-67-derived transition metal oxides

Metal oxide materials derived from ZIF-67 possess a high reversible capacity and superior rate and cycle performance, making them excellent electrode materials<sup>25</sup> (as shown in Table 1), which can be easily obtained by thermal treatment, while their charge storage mechanisms obey pseudocapacitance behavior.<sup>48</sup> Moreover, in the future, the class of transition metal oxides will play a crucial role in the development of cost-effective, high-powered, and environment-friendly energy storage.<sup>2</sup>

### 2.1 Single metal oxides

Salunkhe *et al.*<sup>49</sup> prepared both nanoporous carbon and nanoporous cobalt oxide materials from a single ZIF-67 precursor by optimizing the annealing conditions, as shown in Fig. 2a. The resulting ZIF-derived carbon possessed highly graphitic walls and a high specific surface area of  $350 \text{ m}^2 \text{ g}^{-1}$ , while the resulting ZIF-derived nanoporous  $\text{Co}_3\text{O}_4$  possessed a high specific area of  $148 \text{ m}^2 \text{ g}^{-1}$ . Also, when both materials were tested in a three-electrode system, they showed high capacitance values ( $272$  and  $504 \text{ F g}^{-1}$ , respectively, at a scan rate of  $5 \text{ mV s}^{-1}$ ). Also, Zhang *et al.*<sup>50</sup> successfully constructed a supercapacitor by adopting porous hollow  $\text{Co}_3\text{O}_4$  derived from the ZIF-67 rhombic dodecahedral structure as the electrode material, which showed a large specific capacitance of  $1100 \text{ F g}^{-1}$  and retained more than 95.1% of its specific capacitance after 6000 continuous charge–discharge cycles. Meanwhile, Guo *et al.*<sup>58</sup> reported an effective approach to synthesize cohesive porous  $\text{Co}_3\text{O}_4/\text{C}$  materials using a ZIF-67 single-source precursor *via* two-step calcination. As a supercapacitor electrode material, the  $\text{Co}_3\text{O}_4/\text{C}$  composite exhibited a higher specific capacitance ( $875.6 \text{ F g}^{-1}$  at  $1 \text{ A g}^{-1}$ ) and better cycling stability (capacitance retention of 87.8% after 1000 cycles at  $6 \text{ A g}^{-1}$ ) compared to pure  $\text{Co}_3\text{O}_4$  ( $245.3 \text{ F g}^{-1}$  and 78.4% under the same conditions). In addition, it showed good cycling stability with a capacitance retention of 82% after 1000 cycles at  $6 \text{ A g}^{-1}$  in a symmetric supercapacitor device. The better electrochemical performance of the composite can be attributed to the improvement in conductivity, larger surface area for more active sites, and the ameliorative volume expansion of  $\text{Co}_3\text{O}_4$  by the stable structure of  $\text{Co}_3\text{O}_4$  nanoparticles well embedded in the partially graphitized carbon matrix during the long

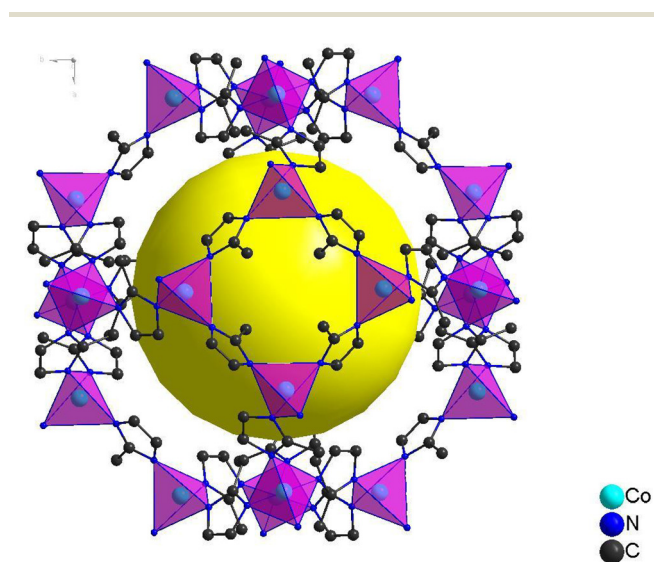
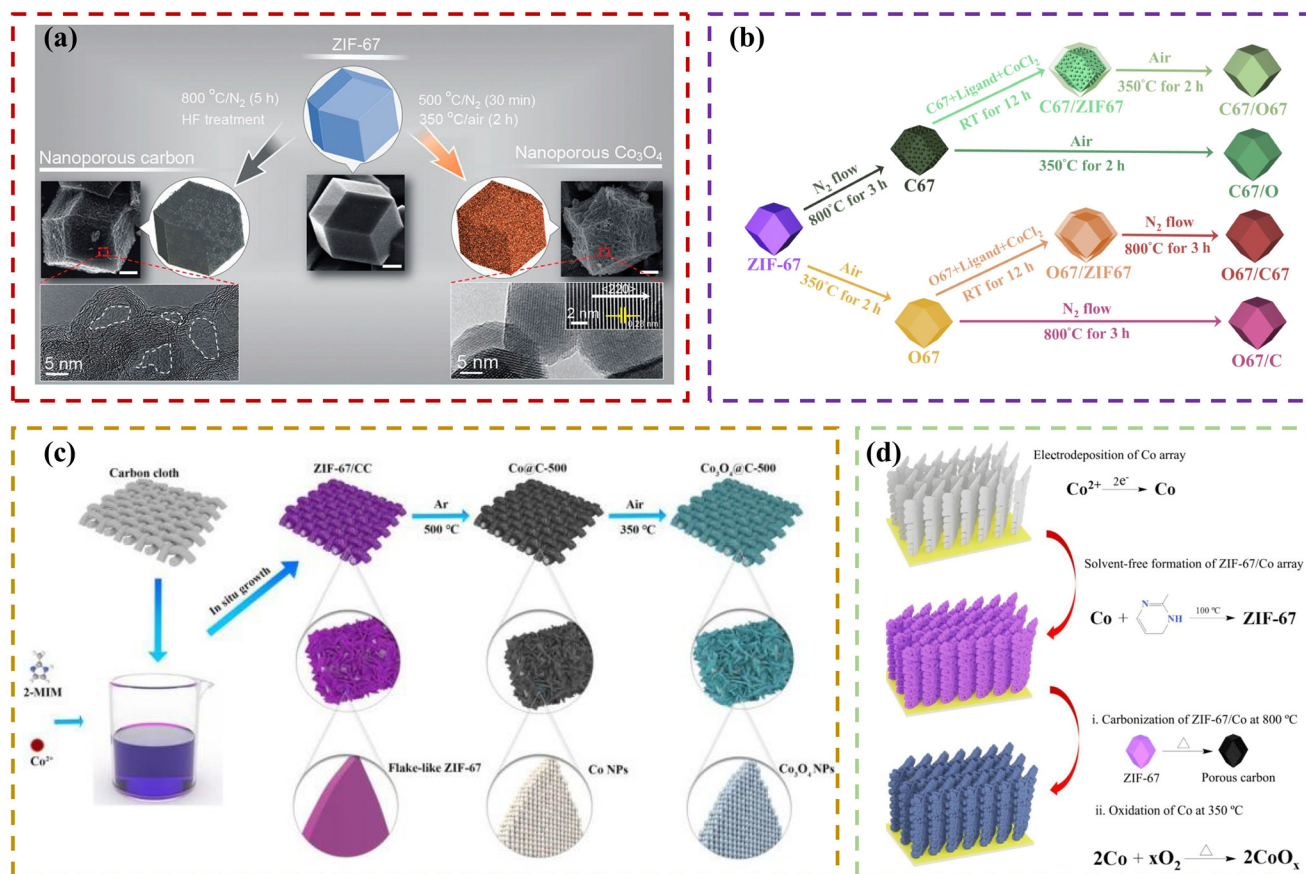


Fig. 1 Schematic of the structure of ZIF-67, showing the connection between its various atoms.

**Table 1** Summary of the electrochemical characteristics of ZIF-67-derived oxide materials determined using three-electrode measurements

Electrode materials	Specific capacity	Electrolyte	Potential window (CV)	Capacity retention	Cyclic stability	Ref.
Co <sub>3</sub> O <sub>4</sub>	504 F g <sup>-1</sup> at 5 mV s <sup>-1</sup>	6 M KOH	-0.1–0.4 V (Ag/AgCl)	52% (5 to 200 mV s <sup>-1</sup> )		49
Co <sub>3</sub> O <sub>4</sub>	1110 F g <sup>-1</sup> at 1.25 A g <sup>-1</sup>	3 M KOH	0–0.5 V (Hg/HgO)	39.4% (1.25 to 12.5 A g <sup>-1</sup> )	95.1% (6000)	50
Co <sub>3</sub> O <sub>4</sub> -NTA	2.26 C cm <sup>-2</sup> at 2 mA cm <sup>-2</sup>	2 M KOH	0–0.6 V	46.9% (2 to 40 mA cm <sup>-2</sup> )	96.9% (5000)	51
Co <sub>3</sub> O <sub>4</sub> /3DGN/NF	321 F g <sup>-1</sup> at 1 A g <sup>-1</sup>	6 M KOH	0–0.5 V (Hg/HgO)	76.6% (1 to 20 A g <sup>-1</sup> )	88% (2000)	52
Co <sub>3</sub> O <sub>4</sub> /C@MoS <sub>2</sub>	1076 F g <sup>-1</sup> at 1 A g <sup>-1</sup>	2 M KOH	0–0.7 V (Ag/AgCl)	76.9% (1 to 10 A g <sup>-1</sup> )	64.5% (5000)	53
Co <sub>3</sub> O <sub>4</sub> -CeO <sub>2</sub>	1288.3 F g <sup>-1</sup> at 2.5 A g <sup>-1</sup>	3 M KOH	0–0.55 V (Hg/HgO)	53.3% (2.5 to 12.5 A g <sup>-1</sup> )	>96.7% (6000)	54
M-Co <sub>3</sub> O <sub>4</sub>	1216.4 F g <sup>-1</sup> at 1 A g <sup>-1</sup>	2 M KOH	0–0.6 V (Hg/HgO)	76.1% (1 to 20 A g <sup>-1</sup> )		55
Ni <sub>x</sub> Co <sub>3-x</sub> O <sub>4</sub> /CNTs	668 F g <sup>-1</sup> at 1 A g <sup>-1</sup>	2 M KOH	0–0.6 V (Ag/AgCl)	91.6% (1 to 10 A g <sup>-1</sup> )	91.2% (2000)	56
MnCo <sub>2</sub> O <sub>4</sub> @Co <sub>3</sub> O <sub>4</sub>	1440 C cm <sup>-2</sup> at 1 mA cm <sup>-2</sup>	2 M KOH	0–0.6 V (SCE)	36% (1 to 10 mA cm <sup>-2</sup> )	82.76% (8000)	57
Co <sub>3</sub> O <sub>4</sub> /C	875.6 F g <sup>-1</sup> at 1 A g <sup>-1</sup>	6 M KOH	0–0.5 V (Ag/AgCl)		87.8% (1000)	58
Co <sub>3</sub> O <sub>4</sub> @N-pC	422.8 F g <sup>-1</sup> at 1 A g <sup>-1</sup>	1 M KOH	-0.2–0.8 V (SCE)	60.5% (1 to 5 A g <sup>-1</sup> )	87.9% (5000)	59
rGO/Co <sub>3</sub> O <sub>4</sub>	688 F g <sup>-1</sup> at 1 A g <sup>-1</sup>	6 M KOH	0–0.5 V (SCE)	64.3% (1 to 10 A g <sup>-1</sup> )	79.7% (1000)	60
Co <sub>3</sub> O <sub>4</sub> /Co(OH) <sub>2</sub>	184.9 mA h g <sup>-1</sup> at 1 A g <sup>-1</sup>	1 M KOH	-0.1–0.4 V (Ag/AgCl)	76% (1 to 16 A g <sup>-1</sup> )		61
Co <sub>3</sub> O <sub>4</sub> /MCS	1409.5 F g <sup>-1</sup> at 0.5 A g <sup>-1</sup>	1 M KOH	0–0.65 V (SCE)	93.5% (0.5 to 1 A g <sup>-1</sup> )	93.2% (1000)	62
Au@Co <sub>3</sub> O <sub>4</sub>	763 F g <sup>-1</sup> at 1 A g <sup>-1</sup>	2 M KOH	0.2–0.7 V	76% (1 to 10 A g <sup>-1</sup> )	83.7% (5000)	63
ZCCO	701 C g <sup>-1</sup> at 2 A g <sup>-1</sup>	3 M KOH	-0.1–0.55 V (Hg/HgO)	61% (2 to 60 A g <sup>-1</sup> )	93.6% (6000)	64
NiCo LDH/Co <sub>3</sub> O <sub>4</sub>	1393.9 F g <sup>-1</sup> at 1 A g <sup>-1</sup>	3 M KOH	0–0.5 V (Ag/AgCl)	71.3% (1 to 15 A g <sup>-1</sup> )	88.4% (5000)	65
NS-Co <sub>3</sub> O <sub>4</sub> @PC	940 F g <sup>-1</sup> at 1 A g <sup>-1</sup>	6 M KOH	0–0.6 V (Hg/HgO)	42.5% (1 to 20 A g <sup>-1</sup> )		66
Co <sub>3</sub> O <sub>4</sub> @MnO <sub>2</sub>	413 F g <sup>-1</sup> at 0.5 A g <sup>-1</sup>	1 M LiOH	0–0.6 V (Ag/AgCl)	41% (0.5 to 10 A g <sup>-1</sup> )	110% (2000)	67
NiMoO <sub>4</sub> @Co <sub>3</sub> O <sub>4</sub> /CA	436.9 C g <sup>-1</sup> at 0.5 A g <sup>-1</sup>	2 M KOH	0–0.6 V (SCE)	70.7% (0.5 to 10 A g <sup>-1</sup> )	82.7% (5000)	68
3D-H CoWO <sub>4</sub> /NF	1395 F g <sup>-1</sup> at 0.5 A g <sup>-1</sup>	6 M KOH	0–0.6 V (SCE)	32.3% (0.5 to 40 A g <sup>-1</sup> )	89% (3000)	69
Co <sub>3</sub> V <sub>2</sub> O <sub>7</sub> /G	276.5 C g <sup>-1</sup> at 1 A g <sup>-1</sup>	1 M KOH	0–0.6 V (Ag/AgCl)	62.5% (1 to 20 A g <sup>-1</sup> )	93% (10 000)	70
Z-CoO/RGO	275 F g <sup>-1</sup> at 1 A g <sup>-1</sup>	6 M KOH	-1–0 V (Ag/AgCl)	53% (1 to 10 A g <sup>-1</sup> )		71
Fe-doped Co <sub>3</sub> O <sub>4</sub>	1535.8 F g <sup>-1</sup> at 1 A g <sup>-1</sup>	6 M KOH	0–0.5 V (Hg/HgO)		88% (8000)	72
Co <sub>3</sub> O <sub>4</sub> /NiCo <sub>2</sub> O <sub>4</sub>	770 F g <sup>-1</sup> at 1 A g <sup>-1</sup>	6 M KOH	0–0.5 V (Ag/AgCl)	84% (1 to 20 A g <sup>-1</sup> )	70% (10 000)	73
Co <sub>3</sub> O <sub>4</sub> /NiNH	583 C g <sup>-1</sup> at 1 A g <sup>-1</sup>	6 M KOH	0–0.6 V (Hg/HgO)	82% (1 to 20 A g <sup>-1</sup> )		74
Co <sub>3</sub> O <sub>4</sub> /N-rGA	1485 F g <sup>-1</sup> at 1 A g <sup>-1</sup>	6 M KOH	0–0.4 V (SCE)	61% (1 to 20 A g <sup>-1</sup> )	93.4% (5000)	75
NPC-60	594.8 mF cm <sup>-2</sup> at 5 mV s <sup>-1</sup>	6 M KOH	0–0.45 V (SCE)		64% (2000)	76
Co <sub>3</sub> O <sub>4</sub> @C	703.3 F g <sup>-1</sup> at 1 A g <sup>-1</sup>	1 M KOH	0–0.8 V (SCE)	82.7% (1 to 10 A g <sup>-1</sup> )	100% (10 000)	77
ZnO/Co <sub>3</sub> O <sub>4</sub> /NiO	1119.11 C g <sup>-1</sup> at 1 A g <sup>-1</sup>	2 M KOH	-0.1–0.7 V (SCE)	72.92% (1 to 10 A g <sup>-1</sup> )	93.75% (5000)	78
Co <sub>3</sub> O <sub>4</sub> @Co/NC-HN	273.9 mA h g <sup>-1</sup> at 1 A g <sup>-1</sup>	3 M KOH	0–0.75 V (Hg/HgO)	47.6% (1 to 10 A g <sup>-1</sup> )	86.3% (3000)	79
Co <sub>3</sub> O <sub>4</sub> @NPC/Ni	525 F g <sup>-1</sup> at 1.5 A g <sup>-1</sup>	1 M KOH	0–0.6 V (Ag/AgCl)	42.9% (1.5 to 5 A g <sup>-1</sup> )	81% (8000)	80
Porous Co <sub>3</sub> O <sub>4</sub> -CNTs	875 F g <sup>-1</sup> at 5 mV s <sup>-1</sup>	6 M KOH	0–0.5 V (SCE)		98% (1000)	38
CoO <sub>x</sub> /carbon	1660.4 F g <sup>-1</sup> at 1 A g <sup>-1</sup>	1 M KOH	-0.1–0.4 V (Ag/AgCl)	22% (1 to 20 A g <sup>-1</sup> )	95.9% (10 000)	81
Co <sub>3</sub> O <sub>4</sub> @NiO	1017 F g <sup>-1</sup> at 1 A g <sup>-1</sup>		0–0.6 V (SCE)	55.9% (1 to 25 A g <sup>-1</sup> )	90.1% (10 000)	82
Co <sub>3</sub> O <sub>4</sub> HPCs	140 F g <sup>-1</sup> at 1 A g <sup>-1</sup>		0–0.5 V (Hg/HgO)	49.5% (1 to 15 A g <sup>-1</sup> )		83
Co <sub>3</sub> O <sub>4</sub> @N-doped C	709 F g <sup>-1</sup> at 1 A g <sup>-1</sup>	1 M KOH	0–0.4 V (Ag/AgCl)	43% (1 to 10 A g <sup>-1</sup> )	83% (5000)	84
α-Ni(Co)S@NiCoO <sub>2</sub>	502.4 mA h g <sup>-1</sup> at 1 A g <sup>-1</sup>	2 M KOH	-0.2–0.7 V (Ag/AgCl)	45.7% (1 to 20 A g <sup>-1</sup> )		85
Co-O-NSs@CFC	842 F g <sup>-1</sup> at 1 A g <sup>-1</sup>	6 M KOH	0–0.6 V (Ag/AgCl)	40% (1 to 20 A g <sup>-1</sup> )	96.4% (10 000)	86
CoVO-HNC	427.64 F g <sup>-1</sup> at 1 A g <sup>-1</sup>	3 M KOH	0–0.6 V (Hg/HgO)	88% (1 to 10 A g <sup>-1</sup> )	89.38% (10 000)	87
Co <sub>3</sub> O <sub>4</sub> @CoNi <sub>2</sub> S <sub>4</sub> -20/CC	1798 F g <sup>-1</sup> at 1 A g <sup>-1</sup>	1 M KOH	0–0.6 V (Ag/AgCl)	77.9% (1 to 10 A g <sup>-1</sup> )		88
Ni-Co LDH@Co <sub>3</sub> O <sub>4</sub> NC	1866 F g <sup>-1</sup> at 2 A g <sup>-1</sup>	1 M KOH	0–0.6 V (Ag/AgCl)	80% (2 to 40 A g <sup>-1</sup> )		89
Co <sub>3</sub> O <sub>4</sub> @C	251 F g <sup>-1</sup> at 1 A g <sup>-1</sup>	1 M KOH	0–0.6 V (Hg/HgO)	84% (1 to 5 A g <sup>-1</sup> )	90% (5000)	90
NiCo <sub>2</sub> O <sub>4</sub> /graphene	1365 F g <sup>-1</sup> at 1 A g <sup>-1</sup>	1 M KOH	0–0.65 V (Ag/AgCl)	51.5% (1 to 10 A g <sup>-1</sup> )	89.11% (2000)	91
Ni/Co-CN	1701 F g <sup>-1</sup> at 1 A g <sup>-1</sup>	3 M KOH	0–0.5 V (Ag/AgCl)	61.9% (1 to 10 A g <sup>-1</sup> )		92
Co <sub>3</sub> O <sub>4</sub> @MnO <sub>2</sub>	768 C g <sup>-1</sup> at 1 A g <sup>-1</sup>	1 M KOH	0–0.6 V (Hg/HgO)		86% (5000)	93
Co(OH)F@Co <sub>3</sub> O <sub>4</sub> /NF	543 F g <sup>-1</sup> at 1 A g <sup>-1</sup>	3 M KOH	0–0.7 V	57.8% (1 to 10 A g <sup>-1</sup> )	88.34% (5000)	94
Co <sub>3</sub> O <sub>4</sub> @NC	1144 F g <sup>-1</sup> at 1 A g <sup>-1</sup>	6 M KOH	0–0.6 V (Hg/HgO)	45.4% (1 to 20 A g <sup>-1</sup> )	91.6% (10 000)	95
CoMoO <sub>4</sub> @Co <sub>3</sub> O <sub>4</sub>	2003 F g <sup>-1</sup> at 1 A g <sup>-1</sup>	3 M KOH	-0.1–0.6 V (Ag/AgCl)		68% (5000)	96
Co <sub>3</sub> O <sub>4</sub> @SiO <sub>2</sub> /PPy	107.7 F g <sup>-1</sup> at 0.6 A g <sup>-1</sup>	1 M KOH	-0.55–0.45 V (Ag/AgCl)			97
MWCNT <sub>x</sub> @Co <sub>3</sub> O <sub>4</sub>	206.89 F g <sup>-1</sup> at 1 A g <sup>-1</sup>	3 M KOH	0–0.6 V (Ag/AgCl)	92.6% (1 to 5 A g <sup>-1</sup> )	78.9% (1000)	98
HCT-2@Co <sub>3</sub> O <sub>4</sub> @SnS <sub>2</sub>	439 F g <sup>-1</sup> at 1 A g <sup>-1</sup>	6 M KOH	0–0.5 V (Hg/HgO)	72.1% (1 to 20 A g <sup>-1</sup> )	63.5% (15 000)	99
Co <sub>3</sub> O <sub>4</sub> -VG-CC	1360 F g <sup>-1</sup> at 2.5 A g <sup>-1</sup>	2 M KOH	0–0.8 V (Hg/HgO)	90% (2.5 to 50 A g <sup>-1</sup> )		100
Co <sub>3</sub> O <sub>4</sub> /NiCo <sub>2</sub> O <sub>4</sub> DSNCs	236.18 C g <sup>-1</sup> at 1 mA cm <sup>-2</sup>	2 M KOH	0–0.6 V (SCE)	63.1% (1 to 20 mA cm <sup>-2</sup> )	103.43% (5000)	101
Carbon/TiO <sub>2</sub> /Co <sub>3</sub> O <sub>4</sub>	481.7 F g <sup>-1</sup> at 1 A g <sup>-1</sup>	3 M KOH	-0.05–0.55 V (Hg/HgO)	78.9% (1 to 10 A g <sup>-1</sup> )	91.6% (10 000)	102
Co <sub>3</sub> O <sub>4</sub> -NiCo <sub>2</sub> O <sub>4</sub> @CF	166.25 F g <sup>-1</sup> at 1 A g <sup>-1</sup>	1 M KOH	-0.5–0.5 V (Ag/AgCl)	91% (1 to 2.5 A g <sup>-1</sup> )		103
CoO <sub>x</sub> /CNF	750 mF cm <sup>-2</sup> at 10 mV s <sup>-1</sup>	6 M KOH	0–1 V	81% (10 to 100 mV s <sup>-1</sup> )	91% (10 000)	104
NM-CH/ZnO@Co <sub>3</sub> O <sub>4</sub> CNCs	1179 F g <sup>-1</sup> at 0.5 A g <sup>-1</sup>	1 M KOH	0–0.7 V (Ag/AgCl)	72.5% (0.5 to 20 A g <sup>-1</sup> )	98% (25 000)	105
CoFe <sub>2</sub> O <sub>4</sub> -Fe@NC-700	3960.9 F g <sup>-1</sup> at 1 A g <sup>-1</sup>	6 M KOH	-0.2–0.7 V (SCE)			106
Co <sub>3</sub> O <sub>4</sub> @N-pc/PEDOT	305.3 F g <sup>-1</sup> at 0.6 A g <sup>-1</sup>	1 M KOH	0–0.45 V (Ag/AgCl)		84% (3000)	107
CuCo <sub>2</sub> O <sub>4</sub> @40-rGO	762 F g <sup>-1</sup> at 0.5 A g <sup>-1</sup>	6 M KOH	0–0.6 V (Ag/AgCl)	71.6% (0.5 to 20 A g <sup>-1</sup> )	108% (5000)	108
Pt-NiCo <sub>2</sub> O <sub>4</sub> /C	1665.3 F g <sup>-1</sup> at 1 A g <sup>-1</sup>	6 M KOH	0–0.4 V (SCE)		94.49% (3500)	109
FeNiCo ZIF-67 (1 : 2 : 1)	532.7 F g <sup>-1</sup> at 1 A g <sup>-1</sup>	3 M KOH	-0.3–0.25 V (Ag/AgCl)	41.4% (1 to 10 A g <sup>-1</sup> )	91% (10 000)	110
Co <sub>3</sub> O <sub>4</sub> -carbon	574.44 F g <sup>-1</sup> at 1 A g <sup>-1</sup>	6 M KOH	0–0.5 V (Ag/AgCl)	52.6% (1 to 20 A g <sup>-1</sup> )	94.7% (1000)	111





**Fig. 2** (a) Schematic of the process for the preparation of nanoporous carbon and nanoporous  $\text{Co}_3\text{O}_4$  from a ZIF-67 polyhedron as the single precursor by optimized thermal treatment. The actual SEM images and high-resolution TEM images of the respective materials are shown below their illustrations. Reprinted with permission from ref. 49, Copyright 2015, the American Chemical Society. (b) Illustration of the process for the synthesis of C67, C67/O67, C67/O, O67, O67/C67 and O67/C. Reprinted with permission from ref. 112, Copyright 2021, Elsevier Ltd. (c) Schematic of the formation of  $\text{Co}_3\text{O}_4/\text{C}$  nanosheet array. Reprinted with permission from ref. 77, Copyright 2021, Elsevier B.V. (d) Schematic of the process for the preparation of  $\text{CoO}_x/\text{carbon}$  arrays. Reprinted with permission from ref. 81, Copyright 2021, the American Chemical Society.

cycling process. To compare the influence of the order of the two-step calcination in the oxide/carbon composite materials, Chen *et al.*<sup>112</sup> synthesized six active materials including carbonized ZIF67 (C67), oxidized C67 (C67/O), oxidized ZIF67-covered C67 (C67/O67), oxidized ZIF67 (O67), carbonized O67 (O67/C) and carbonized ZIF67-covered O67 (O67/C67) (shown in Fig. 2b). Among them, the C67/O electrode showed the highest capacitance value of  $332.3 \text{ mF cm}^{-2}$  at  $20 \text{ mV s}^{-1}$  due to the suitable N-doped graphite and  $\text{Co}_3\text{O}_4$  composition as well as the porous particle-assembled polyhedron structure. Similarly, as shown in Fig. 2c, Shu *et al.*<sup>77</sup> grew flake-like ZIF-67 on carbon cloth, and subsequently synthesized  $\text{Co}_3\text{O}_4/\text{C}$  by adopting a similar two-step thermal conversion. As a result, this strategy effectively prevents structural collapse and defect formation, which are usually caused by the direct oxidation of ZIF-67 nanosheets. In supercapacitor tests,  $\text{Co}_3\text{O}_4/\text{C}-500$  showed an appreciable specific capacitance ( $703.3 \text{ F g}^{-1}$  at  $1 \text{ A g}^{-1}$ ) and excellent cycling stability with the capacitance retention of 100% after 10 000 cycles at  $10 \text{ A g}^{-1}$ . Moreover, the  $\text{Co}_3\text{O}_4/\text{C}-500/\text{reduced graphene oxide (RGO)}$  asymmetric supercapacitor (ASC) exhibited an energy density

of  $43.99 \text{ W h kg}^{-1}$  at a power density of  $824.8 \text{ W kg}^{-1}$ , and excellent cycling performance with a capacity retention of 88% after 10 000 cycles. This excellent performance was attributed to the rational composition control and unique structure of  $\text{Co}_3\text{O}_4$  nanoparticles embedded in the carbon skeleton, which resulted in short electrolyte diffusion channels as well as electron transport distance and effectively reduced the negative effect of volume change in the electrode materials during the charge/discharge process. Alternatively, Li *et al.*<sup>81</sup> prepared tree-like  $\text{CoO}_x/\text{carbon}$  on Au surface *via* a chemical vapor deposition method and two-step treatment, as shown in Fig. 2d. The as-prepared  $\text{CoO}_x/\text{carbon}$  composite arrays provided a less tortuous pathway for ion diffusion, high pseudocapacitance from the transition metal oxide, and good electrical conductivity from carbon. Moreover, the absence of adhesives in array electrodes is beneficial for the promotion of the electrochemical performance. Subsequently, Wang *et al.*<sup>95</sup> changed the order of the two-step thermal treatment method to obtain  $\text{Co}_3\text{O}_4/\text{NC}$ .  $\text{Co}_3\text{O}_4/\text{NC}$  exhibited a specific capacitance of  $1144 \text{ F g}^{-1}$  at a current density of  $1 \text{ A g}^{-1}$  (much higher than the specific capacitance of pure  $\text{Co}_3\text{O}_4$ ), and its retention rate was 45.4% at a



current density of  $20 \text{ A g}^{-1}$ . In addition, the asymmetric supercapacitor (ASC) device consisting of  $\text{Co}_3\text{O}_4/\text{NC}$  composite electrodes and activated carbon produced the highest energy density of  $40 \text{ W h kg}^{-1}$  at a power density of  $1037 \text{ W kg}^{-1}$ . At a current density of  $5 \text{ A g}^{-1}$ , the capacitor retained 87.6% of its initial capacitance after 10 000 charge/discharge cycles.

## 2.2 Multi-metal oxides

The doping of other metal ions in the precursor ZIF-67 can be performed to derive more transition metal oxides. Also, multi-metal oxides can provide a higher theoretical capacitance because of the greater number of changes in their valence state. Chu *et al.*<sup>69</sup> designed a three-dimensional hollow  $\text{CoWO}_4$  composite grown on Ni-foam ( $3\text{D-H-CoWO}_4/\text{NF}$ ) based on a flower-like ZIF-67 utilizing a facile dipping and hydrothermal approach.  $3\text{D-H-CoWO}_4/\text{NF}$  not only possessed a large specific area and rich active sites, but also accommodated the volume expansion/contraction during the charge/discharge processes. Additionally, its unique structure facilitated fast electron/ion transport, resulting in a high specific capacitance of  $1395 \text{ F g}^{-1}$  and an excellent cycle stability with 89% retention after 3000 cycles and superior rate property. Furthermore,  $3\text{D-H-CoWO}_4/\text{NF}$  could be used as a cathode to assemble an asymmetric supercapacitor (ASC), and  $3\text{D-H-CoWO}_4/\text{NF}//\text{AC}$  showed a good energy density ( $29.0 \text{ W h kg}^{-1}$ ). Similarly, Le *et al.*<sup>70</sup> designed  $\text{Co}_2\text{V}_2\text{O}_7/\text{graphene}$  composites through an *in situ* ion exchange reaction, as shown in Fig. 3g. The morphological and compositional characterization confirmed that ZIF-67 was successfully transformed into the nanoparticle-assembled hollow  $\text{Co}_2\text{V}_2\text{O}_7$  nanocages, which were densely distributed on graphene (shown in Fig. 3a–f). Benefiting from the well-

designed structure and compositions, the electrochemical tests indicated that the as-prepared  $\text{Co}_2\text{V}_2\text{O}_7/\text{graphene}$  electrode exhibited a high specific capacity of  $276.5 \text{ C g}^{-1}$  at  $1 \text{ A g}^{-1}$ , good rate capability (Fig. 3h), and remarkably long cycling stability (93% capacity retention after 10 000 cycles). The asymmetric supercapacitor devices assembled with  $\text{Co}_2\text{V}_2\text{O}_7/\text{graphene}$  and reduced graphene oxides delivered a high energy density of  $25.7 \text{ W h kg}^{-1}$  at a power density of  $663.5 \text{ W kg}^{-1}$  and excellent long cycling stability.

Moreover, the doping of metal ions in the process of forming the precursor ZIF-67 or *in situ* ion exchange reaction of the precursor ZIF-67 is also an important approach to obtain multi-metal oxides. Cheng *et al.*<sup>72</sup> synthesized three-dimensional porous iron-doped  $\text{Co}_3\text{O}_4$  using a single bi-metallic metal–organic framework,  $\text{FeCo-ZIF-67}$  (Fig. 4a). The optimal 3D porous Fe-doped  $\text{Co}_3\text{O}_4$  possessed a high capacitance of  $767.9 \text{ C g}^{-1}$  at  $1 \text{ A g}^{-1}$ . Also, the Fe-doped  $\text{Co}_3\text{O}_4//\text{N-doped carbon HSC}$  device achieved a desirable specific energy ( $37 \text{ W h kg}^{-1}$ ) and power ( $750 \text{ W kg}^{-1}$ ), and satisfactory cycling stability (90% retention after 4000 cycles). Similarly, Venkatesh *et al.*<sup>91</sup> reported the synthesis of  $\text{NiCo}_2\text{O}_4$  nanosheets based on  $\text{NiCo-MOFs}$  and combined them with graphene oxide due to its outstanding mechanical support and electronic conductivity. The  $\text{NiCo}_2\text{O}_4$  nanosheets/graphene nanosheets achieved a high specific capacitance of  $1365 \text{ F g}^{-1}$  at  $1 \text{ A g}^{-1}$  and excellent capacity retention of 89.11% over 2000 cycles at  $10 \text{ A g}^{-1}$ . As shown in Fig. 4b, Zheng *et al.*<sup>106</sup> used pure ZIF-67 as the precursor to fabricate  $\text{CoFe}_2\text{O}_4\text{-Fe@NC}$  particles with a high surface area, which helped to accelerate ion and charge transfer. The specific capacitance of the  $\text{CoFe}_2\text{O}_4\text{-Fe@NC}$  composite carbonized at  $700^\circ\text{C}$  reached

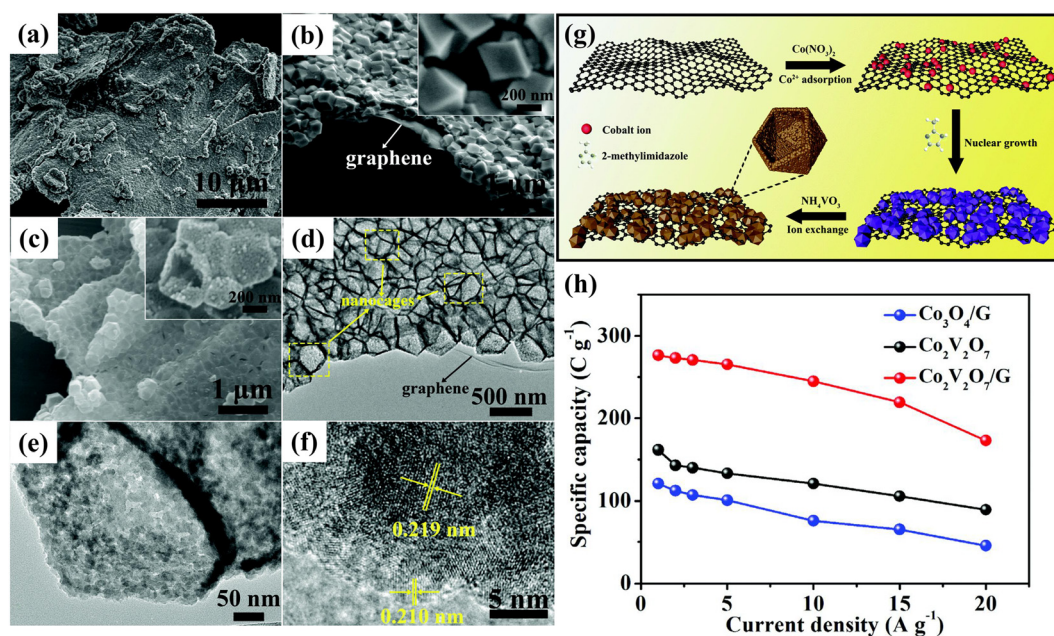


**Fig. 3** (a and b) SEM images of ZIF-67/G; (c) SEM image, (d and e) TEM images, and (f) HR-TEM image of  $\text{Co}_2\text{V}_2\text{O}_7/\text{G}$ . (g) Schematic of the fabrication process for  $\text{Co}_2\text{V}_2\text{O}_7/\text{G}$ . (h) Specific capacitance of  $\text{Co}_2\text{V}_2\text{O}_7$ ,  $\text{Co}_2\text{V}_2\text{O}_7/\text{G}$  and  $\text{Co}_3\text{O}_4/\text{G}$  electrodes at different current densities. Reprinted with permission from ref. 70, Copyright 2020, The Royal Society of Chemistry.

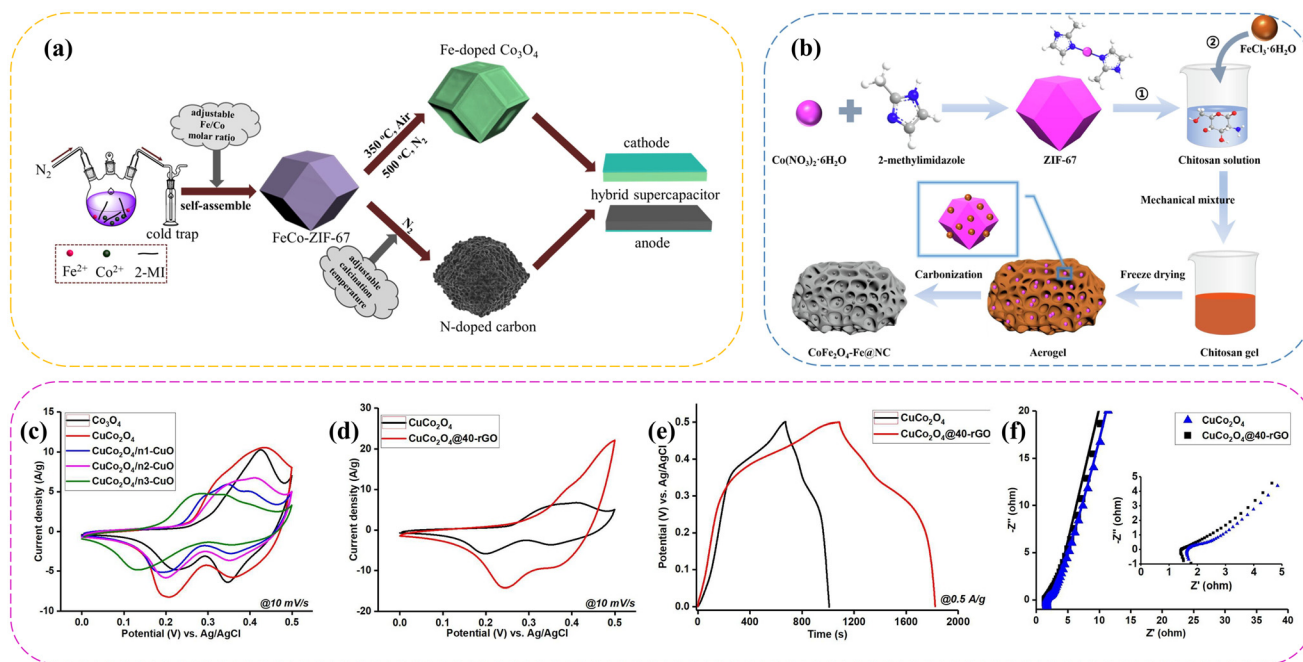


**Fig. 4** (a) Schematic of the design of Fe-doped Co<sub>3</sub>O<sub>4</sub> and N-doped carbon. Reprinted with permission from ref. 72, Copyright 2020, Elsevier Inc. (b) Procedure for the synthesis of the CoFe<sub>2</sub>O<sub>4</sub>-Fe@NC composite material. Reprinted with permission from ref. 106, Copyright 2024 Elsevier Inc. (c) CV curves of the metal oxide electrodes at a scan rate of 10 mV s<sup>-1</sup>; (d) CV curves of CuCo<sub>2</sub>O<sub>4</sub> and CuCo<sub>2</sub>O<sub>4</sub>@40-rGO at 10 mV s<sup>-1</sup>; (e) GCD curves of CuCo<sub>2</sub>O<sub>4</sub> and CuCo<sub>2</sub>O<sub>4</sub>@40-rGO at a current density of 0.5 A g<sup>-1</sup>; and (f) Nyquist plots of CuCo<sub>2</sub>O<sub>4</sub> and CuCo<sub>2</sub>O<sub>4</sub>@40-rGO. Reprinted with permission from ref. 108, Copyright 2024, Elsevier B.V.

3960.9 F g<sup>-1</sup> at 1 A g<sup>-1</sup>. When this composite was combined with activated carbon (AC) to construct an asymmetric supercapacitor (ASC), a density of energy of up to 84.9 W h kg<sup>-1</sup> was attained at a power capacity of 291.6 W kg<sup>-1</sup>. Moreover, this composite maintained a capacitance retention of up to 94.9% after 10 000 cycles. At the same time, Semerci *et al.*<sup>108</sup> prepared CuCo<sub>2</sub>O<sub>4</sub>@rGO nanomaterials using a step-wise method, which involved the annealing of the CoCu-LDH@rGO precursor derived from ZIF-67@rGO. At a graphene concentration of 4.1%, the composite named CuCo<sub>2</sub>O<sub>4</sub>@40-rGO exhibited the best performance among the CuCo<sub>2</sub>O<sub>4</sub>@rGO composites (Fig. 4c-f). A specific capacity of 762 F g<sup>-1</sup> (381 C g<sup>-1</sup>) was recorded at a current density of 0.5 A g<sup>-1</sup> and an excellent rate performance of 71.6%, revealing an excellent capacitive performance and reversibility. Moreover, the electrochemical performance of CuCo<sub>2</sub>O<sub>4</sub>@40-rGO was evaluated as a cathodic electrode and biomass-derived activated carbon (AC) as the negative electrode. The hybrid supercapacitor device showed an energy density of 20.7 W h kg<sup>-1</sup> at a power density of 0.43 kW kg<sup>-1</sup> with a working potential window of 0–1.7 V, as well as 98.8% capacity retention over 10 000 cycles. Also, Wei *et al.*<sup>54</sup> reported the synthesis of hybrid porous Co<sub>3</sub>O<sub>4</sub>-CeO<sub>2</sub> hollow polyhedrons *via* a simple cation-exchange route, followed by heat treatment. When utilized as the electrode material for supercapacitors, the hybrid porous Co<sub>3</sub>O<sub>4</sub>-CeO<sub>2</sub> hollow polyhedrons delivered a large specific capacitance of 1288.3 F g<sup>-1</sup> at 2.5 A g<sup>-1</sup> and a remarkably long cycling stability (<3.3% loss after 6000 cycles). Furthermore, an asymmetric

supercapacitor (ASC) device based on the hybrid porous Co<sub>3</sub>O<sub>4</sub>-CeO<sub>2</sub> hollow polyhedrons was assembled. The ASC device possessed an energy density of 54.9 W h kg<sup>-1</sup>, which retained 44.2 W h kg<sup>-1</sup> even at a power density of 5100 W kg<sup>-1</sup>, indicating its promising application in electrochemical energy storage.

### 2.3 Composite materials

It is estimated that particle-shaped metal oxides usually experience high internal resistance, and consequently reduced charge transfer due to the agglomeration of the particles. In this regard, ZIF-67-derived oxides are usually composited with other materials to improve their electrochemical properties, such as carbon materials and conductive polymers to improve their conductivity or other transition metal compounds to achieve a higher specific capacitance.

Deng *et al.*<sup>52</sup> successfully prepared honeycomb-like porous Co<sub>3</sub>O<sub>4</sub> grown on three-dimensional graphene network/nickel foam (Co<sub>3</sub>O<sub>4</sub>/3DGN/NF) *via* a facile solution growth process with subsequent annealing treatment, as shown in Fig. 5a. Fig. 5b shows Co<sub>3</sub>O<sub>4</sub>/3DGN grown on Ni foam, which possessed a large specific surface area, as shown in Fig. 5c. Also, the Co<sub>3</sub>O<sub>4</sub>/3DGN/NF electrode delivered a high specific capacitance (321 F g<sup>-1</sup> at 1 A g<sup>-1</sup>) and excellent long-cycling stability (88% of its maximum capacitance after 2000 charge-discharge cycles). Furthermore, the Co<sub>3</sub>O<sub>4</sub>/3DGN/NF electrode exhibited the maximum energy density of 7.5 W h kg<sup>-1</sup> with the power density of 794 W kg<sup>-1</sup> and retained 4.1 W h kg<sup>-1</sup> at the power



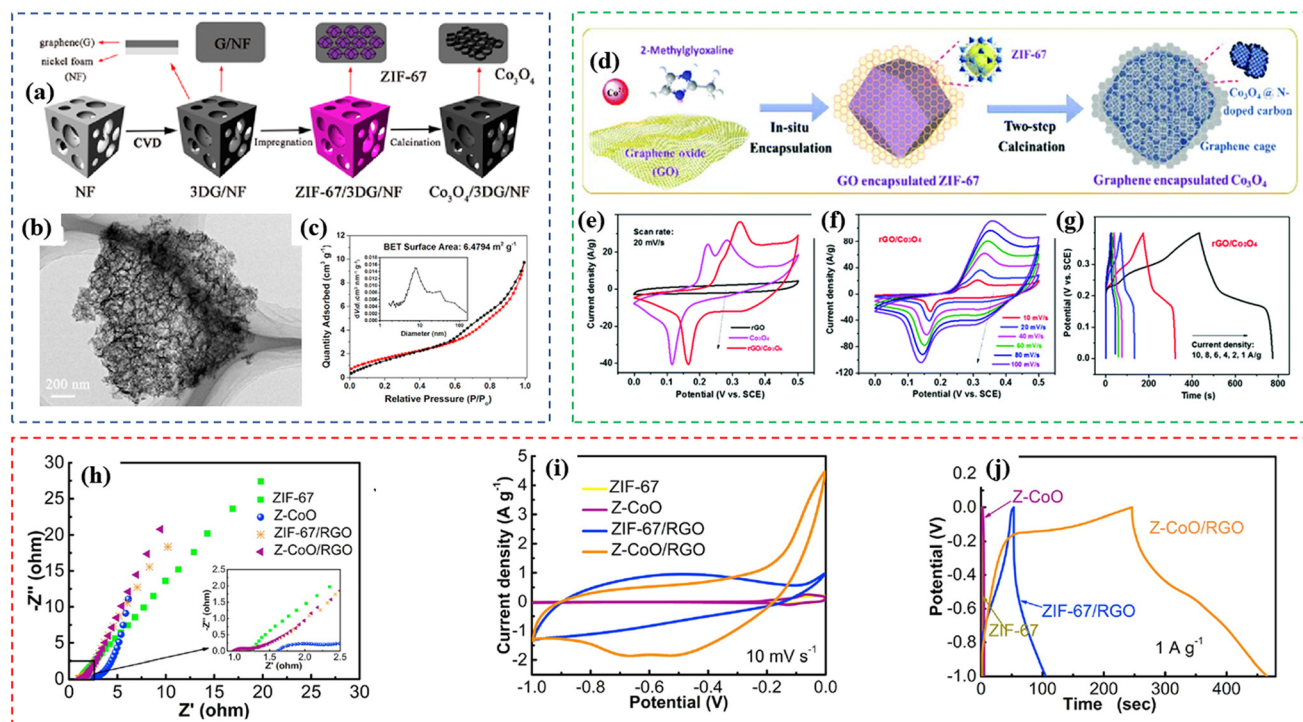


**Fig. 5** (a) Schematic of the fabrication process for Co<sub>3</sub>O<sub>4</sub>/3DGN/NF; (b) TEM image of Co<sub>3</sub>O<sub>4</sub>/3DGN/NF; and (c) pore size distribution of Co<sub>3</sub>O<sub>4</sub>/3DGN/NF. Reprinted with permission from ref. 52, Copyright 2016, Elsevier B.V. (d) Schematic of the synthesis route for rGO/Co<sub>3</sub>O<sub>4</sub> composite; (e) CV curves of rGO, Co<sub>3</sub>O<sub>4</sub>, and rGO/Co<sub>3</sub>O<sub>4</sub> at 20 mV s<sup>-1</sup>; (f) CV curves of rGO/Co<sub>3</sub>O<sub>4</sub> at different scan rates; and (g) GCD curves of rGO/Co<sub>3</sub>O<sub>4</sub> at different current densities. Reprinted with permission from ref. 60, Copyright 2019, The Royal Society of Chemistry. (h) Nyquist impedance plots, (i) CV curves and (j) GCD curves of ZIF-67, Z-CoO, ZIF-67/RGO and Z-CoO/RGO. Reprinted with permission from ref. 71, Copyright 2020, Elsevier Ltd.

density of 15 kW kg<sup>-1</sup> in a two-electrode system. Its enhanced electrochemical properties can be attributed to the unique nanostructure of Co<sub>3</sub>O<sub>4</sub> with admirable pseudocapacitance performance and the intimate integration of graphene with Co<sub>3</sub>O<sub>4</sub> and the Ni foam matrix, which not only enhanced the electron conductivity for fast electron and ion transport but also provided a high specific surface area and excellent structural stability. Similarly, Lin *et al.*<sup>60</sup> obtained rGO/Co<sub>3</sub>O<sub>4</sub> via the *in situ* growth of ZIF-67 polyhedra in the presence of graphene oxide, followed by thermal annealing (Fig. 5d). The resultant rGO/Co<sub>3</sub>O<sub>4</sub> composites consisted of a continuously-conductive double-network constructed from graphene sheets and derived N-doped carbons from ZIF-67, showing a large specific surface area of 523 m<sup>2</sup> g<sup>-1</sup>. The as-fabricated symmetrical supercapacitor based on rGO/Co<sub>3</sub>O<sub>4</sub> exhibited a high specific capacitance of 277.5 F g<sup>-1</sup> at 25 A g<sup>-1</sup> (as compared in Fig. 5e–g) and an energy density of 24.7 W h kg<sup>-1</sup> at a power density of up to 40 kW kg<sup>-1</sup>. The supercapacitor also retained 87.5% of its initial capacitance over 5000 cycles at 5 A g<sup>-1</sup>. The large capacitance, high energy density, and excellent cycling stability for rGO/Co<sub>3</sub>O<sub>4</sub> can be attributed to the 3D double conductive network from the 2D graphene sheets and porous channels of the pseudo-capacitive Co<sub>3</sub>O<sub>4</sub> polyhedra. Moreover, Zha *et al.*<sup>71</sup> initially synthesized ZIF-67-derived CoO, and then formed a composite with reduced graphene oxide through the hydrothermal method. As shown in Fig. 5h–j, Z-CoO/RGO

exhibited an outstanding mass specific capacitance (275 F g<sup>-1</sup> at 1 A g<sup>-1</sup>) and excellent resistance characteristic due to the synergistic effect between ZIF-67 and RGO. Besides graphene, Yang *et al.*<sup>98</sup> reported the preparation of ZIF-67-derived cobalt oxide/carbon nanotube (MWCNT<sub>x</sub>@Co<sub>3</sub>O<sub>4</sub>) composites by calcining the MWCNT<sub>x</sub>@ZIF-67 precursor in one step. Benefiting from the homogeneous conductive carbon nanotubes, the synthesized MWCNT<sub>x</sub>@Co<sub>3</sub>O<sub>4</sub> electrode displayed a maximum specific capacitance of 206.89 F g<sup>-1</sup> at 1 A g<sup>-1</sup>.

Also, Chen's group<sup>97</sup> reported the synthesis and characterization of nanocomposites via a two-step method using polypyrrole (PPy) and Co<sub>3</sub>O<sub>4</sub>@SiO<sub>2</sub> in the presence of an oxidizing agent. As shown in Fig. 6a, Co<sub>3</sub>O<sub>4</sub>@SiO<sub>2</sub>/PPy was obtained by coating PPy on Co<sub>3</sub>O<sub>4</sub>@SiO<sub>2</sub>, which was prepared by annealing SiO<sub>2</sub>-coated ZIF-67 at high temperature. Comparing Fig. 6b with Fig. 6c and d, it can be seen that PPy was well combined with Co<sub>3</sub>O<sub>4</sub>@SiO<sub>2</sub>. Also, the results showed that the specific capacitance of Co<sub>3</sub>O<sub>4</sub>@SiO<sub>2</sub> and Co<sub>3</sub>O<sub>4</sub>@SiO<sub>2</sub>/PPy (2 mL) was 33.36 F g<sup>-1</sup> and 107.7 F g<sup>-1</sup> at 0.6 A g<sup>-1</sup>, indicating that the addition of PPy greatly improved the electrochemical performance of Co<sub>3</sub>O<sub>4</sub>@SiO<sub>2</sub> (as shown in Fig. 6e and f). This may be due to synergy between Co<sub>3</sub>O<sub>4</sub>@SiO<sub>2</sub> and the PPy polymer, where the addition of PPy may help construct more ion channels in Co<sub>3</sub>O<sub>4</sub>@SiO<sub>2</sub> to enhance the ion transport. Subsequently, the next year, Chen's group<sup>107</sup> again reported the preparation of the Co<sub>3</sub>O<sub>4</sub>@N-pc/PEDOT composite as an



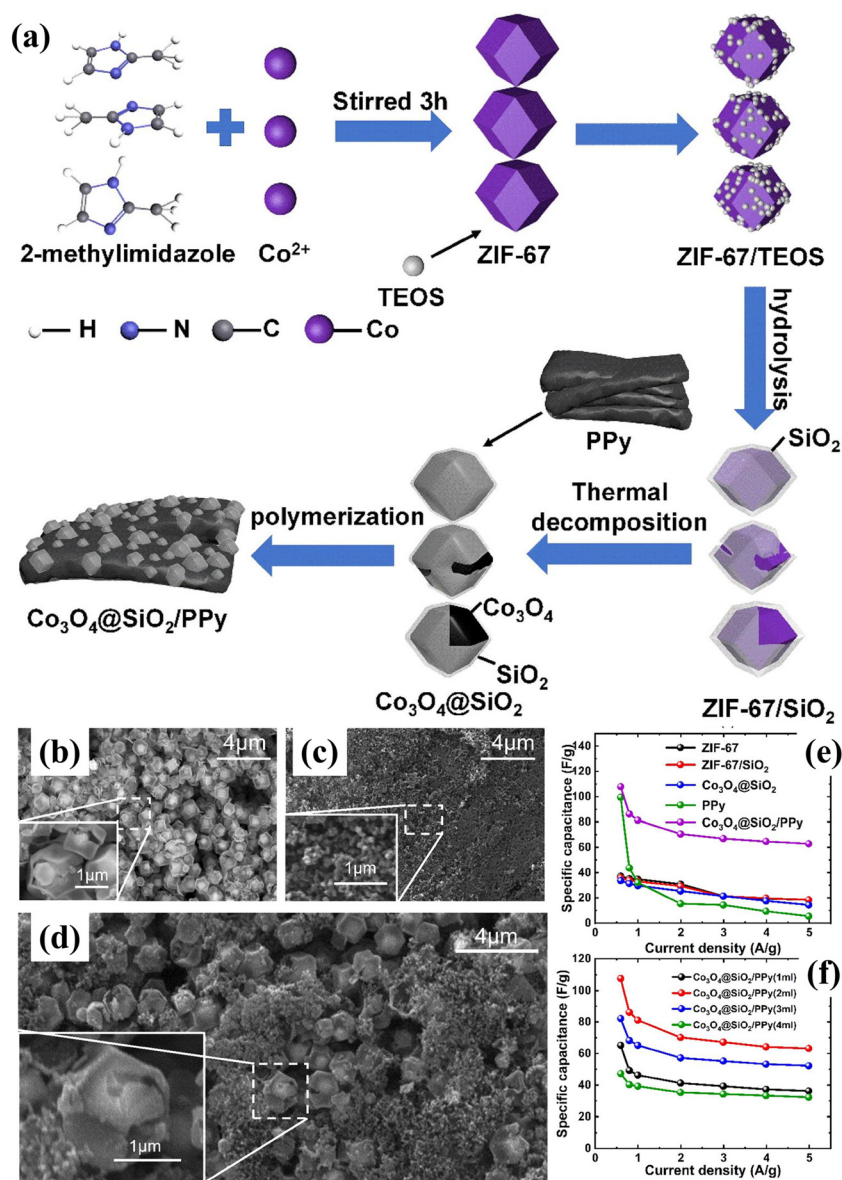


**Fig. 6** (a) Schematic illustration of synthetic procedure for ZIF-67, ZIF-67/SiO<sub>2</sub>, Co<sub>3</sub>O<sub>4</sub>@SiO<sub>2</sub> and Co<sub>3</sub>O<sub>4</sub>@SiO<sub>2</sub>/PPy; SEM images of (b) Co<sub>3</sub>O<sub>4</sub>@SiO<sub>2</sub>, (c) PPy and (d) Co<sub>3</sub>O<sub>4</sub>@SiO<sub>2</sub>/PPy (2 mL); (e) specific capacitance as a function of current density for ZIF-67, ZIF-67/SiO<sub>2</sub>, Co<sub>3</sub>O<sub>4</sub>@SiO<sub>2</sub>, PPy and Co<sub>3</sub>O<sub>4</sub>@SiO<sub>2</sub>/PPy; and (f) specific capacitance as a function of the current density for Co<sub>3</sub>O<sub>4</sub>@SiO<sub>2</sub> and PPy in different proportions. Reprinted with permission from ref. 97, Copyright 2023, Springer Nature.

electrode material for supercapacitors. Employing ZIF-67@ZIF-8 as the precursor, the obtained Co<sub>3</sub>O<sub>4</sub>@N-pc/PEDOT composite exhibited the highest specific capacitance of 305.3 F g<sup>-1</sup> at 0.6 A g<sup>-1</sup>, which is significantly superior to that of PEDOT (63.6 F g<sup>-1</sup>), ZIF-67@ZIF-8-400 (91.4 F g<sup>-1</sup>), ZIF-67 (43.8 F g<sup>-1</sup>) and Co<sub>3</sub>O<sub>4</sub>@N-pc-400 (154.8 F g<sup>-1</sup>). Further, Co<sub>3</sub>O<sub>4</sub>@N-pc/PEDOT (4 mL) was used to construct a symmetric supercapacitor, which delivered outstanding values of energy (20.03 W h kg<sup>-1</sup>) and power density (415.17 W kg<sup>-1</sup>).

Wang *et al.*<sup>53</sup> used ZIF-67 and (NH<sub>4</sub>)<sub>2</sub>MoS<sub>4</sub> as the precursors of Co<sub>3</sub>O<sub>4</sub>/C and MoS<sub>2</sub>, respectively, to obtain hierarchical mesoporous Co<sub>3</sub>O<sub>4</sub>/C@MoS<sub>2</sub> core-shell structure materials *via* calcination and solvothermal methods. Co<sub>3</sub>O<sub>4</sub>/C@MoS<sub>2</sub> exhibi-

ted a high specific capacitance (1076 F g<sup>-1</sup> at 1 A g<sup>-1</sup>), rate capability (76.9% capacitance retention at 10 A g<sup>-1</sup>) and cyclic stability (64.5% capacitance retention after 5000 cycles at 10 A g<sup>-1</sup>) due to the presence of MoS<sub>2</sub>, greatly influencing the electrochemical performances of the obtained core-shell materials, which were better than that of Co<sub>3</sub>O<sub>4</sub>/C. Xu *et al.*<sup>67</sup> reported the synthesis of a hollow Co<sub>3</sub>O<sub>4</sub>@MnO<sub>2</sub> cubic nano-material derived from the ZIF-67@Mn-ZIF sacrificial precursor. It demonstrated high performances, such as specific capacitance of 413 F g<sup>-1</sup> at the current density of 0.5 A g<sup>-1</sup>, and when the current density increased from 0.5 to 10 A g<sup>-1</sup> (20 times increase), it still exhibited ~41% retention of its initial capacitance. Similarly, Babu *et al.*<sup>93</sup> also synthesized a type of

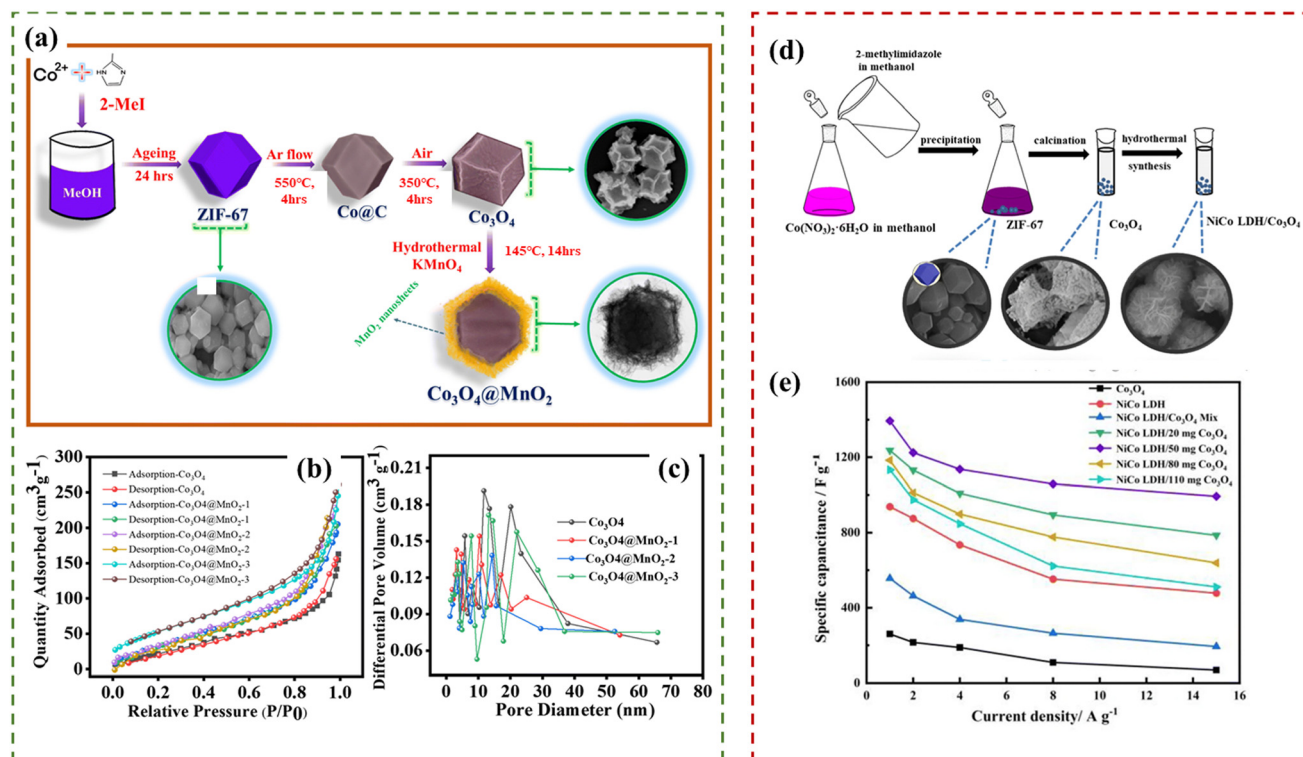


**Fig. 7** (a) Schematic diagram of the synthesis of  $\text{Co}_3\text{O}_4@/\text{MnO}_2$  core-shell structure; (b) BET analysis and (c) BJH pore size distribution curves of ZIF-67-derived  $\text{Co}_3\text{O}_4$ ,  $\text{Co}_3\text{O}_4@/\text{MnO}_2$ -1,  $\text{Co}_3\text{O}_4@/\text{MnO}_2$ -2 and  $\text{Co}_3\text{O}_4@/\text{MnO}_2$ -3. Reprinted with permission from ref. 93, Copyright 2022, The Royal Society of Chemistry. (d) Schematic of the processes for the preparation of  $\text{NiCo LDH}/\text{Co}_3\text{O}_4$ ; and (e) comparison of the specific capacitance of  $\text{Co}_3\text{O}_4$ ,  $\text{NiCo LDH}$ ,  $\text{NiCo LDH}/\text{Co}_3\text{O}_4$  Mix,  $\text{NiCo LDH}/20 \text{ mg Co}_3\text{O}_4$ ,  $\text{NiCo LDH}/50 \text{ mg Co}_3\text{O}_4$ ,  $\text{NiCo LDH}/80 \text{ mg Co}_3\text{O}_4$  and  $\text{NiCo LDH}/110 \text{ mg Co}_3\text{O}_4$  at different current densities. Reprinted with permission from ref. 65, Copyright 2019, Springer Nature.

$\text{Co}_3\text{O}_4@/\text{MnO}_2$  nanosheets using ZIF-67 and provided an effective pathway for rapidly transporting electrons and ions, as shown in Fig. 7a. As a result, the ZIF-67-derived  $\text{Co}_3\text{O}_4@/\text{MnO}_2$ -3 electrode material showed a high specific capacitance of  $768 \text{ C g}^{-1}$  at  $1 \text{ A g}^{-1}$  with outstanding cycling stability (86% retention after 5000 cycles) and the porous structure of the material had a good BET surface area of  $160.8 \text{ m}^2 \text{ g}^{-1}$  according to Fig. 7b and c. As a hybrid supercapacitor,  $\text{Co}_3\text{O}_4@/\text{MnO}_2$ -3/activated carbon exhibited a high specific capacitance ( $82.9 \text{ C g}^{-1}$ ) and long cycle life (85.5% retention after 5000 cycles). Moreover, a high energy density of  $60.17 \text{ W h kg}^{-1}$  and power density of  $2674.37 \text{ W kg}^{-1}$  were achieved. Additionally, as shown in Fig. 7d, Dai *et al.*<sup>65</sup> modified ZIF-67-derived  $\text{Co}_3\text{O}_4$  with  $\text{NiCo}$ -layered double hydroxide nanosheets to obtain an outstanding electrode composite material. The specific capacitance of  $\text{NiCo LDH}/50 \text{ mg Co}_3\text{O}_4$  was  $1393.9 \text{ F g}^{-1}$  at  $1 \text{ A g}^{-1}$  with outstanding cycle stability (88.4% up to 5000 cycles) compared with other electrodes, as shown in Fig. 7e. An aqueous asymmetric supercapacitor (ASC) was assembled by employing  $\text{NiCo LDH}/50 \text{ mg Co}_3\text{O}_4$  as the positive electrode and activated carbon (AC) as the negative electrode, which delivered a voltage window of  $1.5 \text{ V}$  and a high energy density of  $46.4 \text{ W h kg}^{-1}$  at a power density of  $750.4 \text{ W kg}^{-1}$ .

Considering two-electrode systems, El-Deen's group<sup>89</sup> further applied  $\text{Ni-Co LDH}/\text{Co}_3\text{O}_4$  nanocubes (prepared as shown in

Fig. 8a) in an asymmetric solid-state supercapacitor device (ASC) and constructed the device based on a full cell with the  $\text{Ni-Co LDH}/\text{Co}_3\text{O}_4$  nanocubes and three-dimensional spongy graphene. When tested in a two-electrode system, as shown in Fig. 8b–e, the ASC delivered the highest energy density of  $66.7 \text{ W h kg}^{-1}$  with a power density of  $800 \text{ W kg}^{-1}$  and superior recyclability over 10 500 cycles with a holding capacitance retention ratio of 90.5% and coulombic efficiency of 99.8%. Recently, Wang *et al.*<sup>99</sup> reported the preparation of hollow carbon tube@ $\text{Co}_3\text{O}_4@/\text{SnS}_2$  composites by growing ZIF-67 and  $\text{SnS}_2$  nanosheets on a PMMA/PAN/ $\text{Zn}^{2+}$  electrospun film as the precursors (Fig. 8f). The unique inner core-shell and the outer-shell  $\text{SnS}_2$  contributed to the excellent characteristics, including abundant pores and channels for rapid ion transport and storage, high specific surface area, improved electrical conductivity, and additional electroactive sites for the faradaic reaction. Owing to the synergy between the unique 1D porous hollow structure and the different components, the as-fabricated HCT-2@ $\text{Co}_3\text{O}_4@/\text{SnS}_2$  electrode exhibited a high specific capacitance of  $439 \text{ F g}^{-1}$  at  $1 \text{ A g}^{-1}$ . Moreover, as shown in Fig. 8g, the assembled flexible supercapacitor also demonstrated a remarkable energy density of  $40.22 \text{ W h kg}^{-1}$ , the corresponding power density of  $750.22 \text{ W kg}^{-1}$ , and long cycle life (Fig. 8j). In addition, no structural deformation and capacitance loss were observed in the bent devices, as shown in Fig. 8h and i.

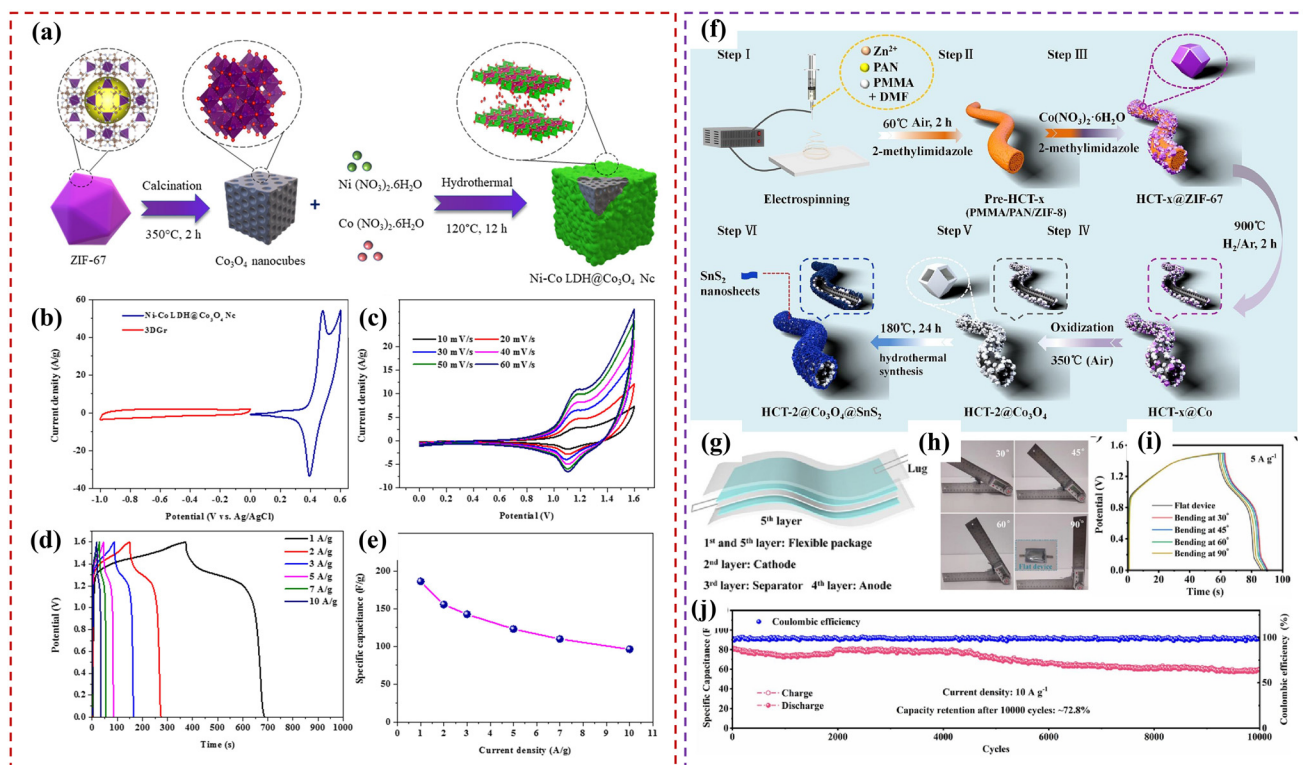


**Fig. 8** (a) Schematic process for the fabrication of Ni-Co LDH@Co<sub>3</sub>O<sub>4</sub> nanocube; (b) CV profiles of 3DSGr and Ni-Co LDH@Co<sub>3</sub>O<sub>4</sub> nanocube electrodes at a scan rate of 10 mV s<sup>-1</sup>; (c) CV plots of the ASC at various scan rates; (d) GCD curves of Ni-Co LDH@Co<sub>3</sub>O<sub>4</sub> nanocube//3DSGr device at various current densities; and (e) capacitance measured for the prepared ASC device. Reprinted with permission from ref. 89, Copyright 2022, Elsevier B.V. (f) Schematic illustration of the preparation of HCT-2@Co<sub>3</sub>O<sub>4</sub>@SnS<sub>2</sub>; (g) schematic illustration of HCT-2@Co<sub>3</sub>O<sub>4</sub>@SnS<sub>2</sub>//AC device; (h) flexible device bending at various angles; (i) GCD plots of the ASC device at various bending conditions; and (j) cycling stability of the device at 10 A g<sup>-1</sup>. Reprinted with permission from ref. 99, Copyright 2023, Elsevier B.V.

### 3. ZIF-67-derived transition metal sulfides

As a type of pseudocapacitor material, sulfides possess larger specific capacitance values, narrower band gaps, lower melting points, higher conductivity and richer redox sites compared to metal oxides. However, they still have some challenges, which limit their further research such as side reactions during the electrochemical measurement process, susceptibility to oxidation and structural destruction.<sup>34</sup> Thus, to solve the above-mentioned problems, the design of the material structure needs to be studied, while ZIF-67 is regarded as a good precursor to obtain transition metal sulfides with unique structures<sup>113</sup> (Table 2).

#### 3.1 Single metal sulfides

Hu *et al.*<sup>114</sup> demonstrated the template-induced formation of double-shelled hollow structures with CoS-nanoparticle-assembled nanoboxes surrounded by outer CoS-nanosheet-constructed shells (CoS-NP/CoS-NS DSNBs). Delicate manipulation of the template-induced reaction between ZIF-67 and water led to the formation of ZIF-67/Co(OH)<sub>2</sub>-nanosheet yolk-shelled structures, which were then transformed into CoS-NP/

CoS-NS DSNBs through the reaction with Na<sub>2</sub>S, as shown in Fig. 9a. As a result of the unique assembly of subunits with different dimensionalities, the CoS-NP/CoS-NS DSNBs possessed a high specific surface area, suitable mesopores, and good structural robustness (Fig. 9b and c), which contributed to their exceptional performance as a battery-type electrode (a specific capacitance of 980 F g<sup>-1</sup> at 1 A g<sup>-1</sup> and 89% retention after 10 000 cycles in Fig. 9d). Additionally, as shown in Fig. 9e, Jia *et al.*<sup>121</sup> reported the designed synthesis of porous quadruple-shelled CoS<sub>2</sub> hollow dodecahedrons with concave surfaces through a template-induced formation process. As the result of the combined advantages of the materials and structures (Fig. 9f), when evaluating as electrodes for supercapacitors, the porous quadruple-shelled CoS<sub>2</sub> showed a high specific capacity of 375.2 C g<sup>-1</sup> with a good rate performance and excellent stability with 92.1% retention after 10 000 cycles. Moreover, the assembled quadruple-shelled CoS<sub>2</sub>//active carbon asymmetric supercapacitor achieved a high energy density of 52.1 W h kg<sup>-1</sup>, excellent specific capacitance (146 F g<sup>-1</sup> at 0.5 A g<sup>-1</sup>), and electrochemical cycling stability (89% retention after 5000 cycles). Moreover, Peng *et al.*<sup>136</sup> successfully synthesized hierarchical porous Co<sub>9</sub>S<sub>8</sub> nanowire arrays grown on Ni foam *via* a multi-step method for use in supercapacitors (Fig. 9g). Introducing ZIF-67 is favorable for the for-



**Table 2** Summary of the electrochemical characteristics of ZIF-67-derived sulfide materials in three-electrode measurements

Electrode materials	Specific capacity	Electrolyte	Potential window (CV)	Capacity retention	Cyclic stability	Ref.
CoS-NP/CoS-NS	980 F g <sup>-1</sup> at 1 A g <sup>-1</sup>	2 M KOH	0–0.6 V (SCE)	60% (1–20 A g <sup>-1</sup> )	89% (10 000)	114
CoNi <sub>2</sub> S <sub>4</sub>	1890 F g <sup>-1</sup> at 4 A g <sup>-1</sup>	2 M KOH	0–0.5 V (Ag/AgCl)	81.2% (4–20 A g <sup>-1</sup> )	71.6% (5000)	32
Co <sub>9</sub> S <sub>8</sub> @N–C@MoS <sub>2</sub>	410 F g <sup>-1</sup> at 10 A g <sup>-1</sup>	3 M KOH	0–0.6 V (Hg/HgO)	79.8% (0.5–20 A g <sup>-1</sup> )	101.7% (20 000)	115
NiCo <sub>2</sub> S <sub>4</sub>	939 C g <sup>-1</sup> at 1 A g <sup>-1</sup>	6 M KOH	–0.1–0.6 V (SCE)	75.8% (1–10 A g <sup>-1</sup> )		116
CNT/CoS	2173.1 F g <sup>-1</sup> at 5 A g <sup>-1</sup>	6 M KOH	–0.07–0.63 (Hg/HgO)	65% (5–20 A g <sup>-1</sup> )		117
GH@NC@Co <sub>9</sub> S <sub>8</sub>	842.4 F cm <sup>-2</sup> at 1 A g <sup>-1</sup>	6 M KOH	0–0.5 V (Ag/AgCl)	65.5% (1–10 A g <sup>-1</sup> )		118
MnO <sub>2</sub> @NiCo-LDH/CoS <sub>2</sub>	1547 F g <sup>-1</sup> at 1 A g <sup>-1</sup>	2 M KOH	0–0.55 V (SCE)	76.9% (1–10 A g <sup>-1</sup> )	82.3% (2000)	119
NiCo <sub>2</sub> S <sub>4</sub>	1232 F g <sup>-1</sup> at 2.1 A g <sup>-1</sup>	3 M KOH	0–0.65 V (Hg/HgO)	55% (2.1–41.5 A g <sup>-1</sup> )	80% (8000)	120
CoS <sub>2</sub>	375.2 C g <sup>-1</sup> at 1 A g <sup>-1</sup>	2 M KOH	–0.2–0.6 V (Hg/HgO)	70% (1–20 A g <sup>-1</sup> )	92.1% (10 000)	121
Mo-doped CoS HNC	781 F g <sup>-1</sup> at 0.5 A g <sup>-1</sup>	2 M KOH	0–0.6 V (SCE)	52% (0.5–10 A g <sup>-1</sup> )	46.8% (5000)	122
CoS <sub>x</sub> /Ni–Co LDH	1562 F g <sup>-1</sup> at 1 A g <sup>-1</sup>	2 M KOH	–0.1–0.55 V (SCE)	65.4% (1–20 A g <sup>-1</sup> )	76.64% (5000)	123
CoS <sub>x</sub> @NiCo-LDH	680.8 C g <sup>-1</sup> at 1 A g <sup>-1</sup>	3 M KOH	0–0.6 V (Ag/AgCl)	76% (1–10 A g <sup>-1</sup> )	80% (3000)	124
NiCo <sub>2</sub> S <sub>4</sub>	1382 F g <sup>-1</sup> at 1 A g <sup>-1</sup>	2 M KOH	0–0.5 V (Ag/AgCl)	83.6% (1–10 A g <sup>-1</sup> )	70% (10 000)	125
CuCo <sub>2</sub> S <sub>4</sub>	1344 F g <sup>-1</sup> at 1 A g <sup>-1</sup>	3 M KOH	0–0.6 V (Hg/HgO)	71.3% (1–30 A g <sup>-1</sup> )	93.1% (5000)	126
Co <sub>3</sub> S <sub>4</sub> -HNCs@PPy	1706 F g <sup>-1</sup> at 1 A g <sup>-1</sup>	2 M KOH	–0.1–0.8 V (SCE)	73.2% (1–10 A g <sup>-1</sup> )	68.1% (5000)	37
Co <sub>3</sub> S <sub>4</sub> @NiO	187.93 F g <sup>-1</sup> at 1 A g <sup>-1</sup>	6 M KOH	0–0.5 V (SCE)	74.1% (1–20 A g <sup>-1</sup> )	92.6% (10 000)	127
MnCo <sub>2</sub> S <sub>4</sub> /Co <sub>9</sub> S <sub>8</sub>	1058 F g <sup>-1</sup> at 1 A g <sup>-1</sup>	6 M KOH	0–0.5 V (Hg/HgO)	47.6% (1–10 A g <sup>-1</sup> )		128
Co <sub>3</sub> S <sub>4</sub> /WS <sub>2</sub>	412.7 F g <sup>-1</sup> at 1 A g <sup>-1</sup>	1 M H <sub>2</sub> SO <sub>4</sub>	0–1 V (Ag/AgCl)		94.3% (2000)	129
NiCo <sub>2</sub> S <sub>4</sub>	1350 F g <sup>-1</sup> at 1 A g <sup>-1</sup>	2 M KOH	0–0.6 V (Hg/HgO)	70% (1–20 A g <sup>-1</sup> )		130
Co–W–S@N, S-PC	1001 F g <sup>-1</sup> at 2 A g <sup>-1</sup>	2 M KOH	0–0.5 V (SCE)	45% (2–20 A g <sup>-1</sup> )		131
Co <sub>3</sub> S <sub>4</sub> /PANI	1106 F g <sup>-1</sup> at 1 A g <sup>-1</sup>	6 M KOH	0–0.5 V (SCE)	66.55% (1–10 A g <sup>-1</sup> )	86% (20 000)	132
rGO/CoS <sub>x</sub> -rGO/rGO	460 F g <sup>-1</sup> at 1 A g <sup>-1</sup>	1 M KOH	0–0.5 V (SCE)	30% (1–16 A g <sup>-1</sup> )	85% (5000)	133
NiCoS@PPy	2316.6 F g <sup>-1</sup> at 1 A g <sup>-1</sup>	2 M KOH	0–0.6 V (SCE)	60.8% (1–10 A g <sup>-1</sup> )		134
α-MnS@Co <sub>3</sub> S <sub>4</sub>	283.3 mA h g <sup>-1</sup> at 1 A g <sup>-1</sup>	6 M KOH	0–0.5 V (Ag/AgCl)	81.5% (1–25 A g <sup>-1</sup> )	92.7% (10 000)	135
Co <sub>9</sub> S <sub>8</sub> /NF	369.1 mA h g <sup>-1</sup> at 1 A g <sup>-1</sup>	6 M KOH	0–0.5 V (Hg/HgO)	75.5% (1–20 A g <sup>-1</sup> )	75% (5000)	136
CoNi <sub>2</sub> S <sub>4</sub> /MXene/NF	933 C g <sup>-1</sup> at 1 A g <sup>-1</sup>	3 M KOH	0–0.7 V (Hg/HgO)	70.2% (1–10 A g <sup>-1</sup> )		137
NiCo-LDH/Co <sub>9</sub> S <sub>8</sub>	1654 F g <sup>-1</sup> at 2 A g <sup>-1</sup>	3 M KOH	0–0.5 V (SCE)	83.3% (2–20 A g <sup>-1</sup> )	82.5% (5000)	138
CoNi <sub>2</sub> S <sub>4</sub>	2448 F g <sup>-1</sup> at 1 A g <sup>-1</sup>	3 M KOH	0–0.43 C	63.3% (1–10 A g <sup>-1</sup> )		139
hollow tube@sheets NiCo <sub>2</sub> S <sub>4</sub>	3227.94 F g <sup>-1</sup> at 2 A g <sup>-1</sup>	2 M KOH	0–0.7 V (SCE)	59% (2–10 A g <sup>-1</sup> )	83.92% (5000)	140
Al-doped Co <sub>9</sub> S <sub>8</sub> @NG	736 C g <sup>-1</sup> at 1 A g <sup>-1</sup>	2 M KOH	–0.2–0.6 V (Ag/AgCl)	71% (1–40 A g <sup>-1</sup> )	92% (10 000)	141
MSZ@NF	4840 mF cm <sup>-2</sup> at 1 mA cm <sup>-2</sup>	2 M KOH	0–0.6 V		81.3% (5000)	142
Co <sub>1-x</sub> S/HNPSCS	1058.9 C g <sup>-1</sup> at 1 A g <sup>-1</sup>	6 M KOH	0–0.6 V (SCE)	74.3% (1–20 A g <sup>-1</sup> )		143
Co <sub>3</sub> S <sub>4</sub> /Ti <sub>3</sub> C <sub>2</sub> T <sub>x</sub>	602 F g <sup>-1</sup> at 1 A g <sup>-1</sup>	3 M KOH	0–0.6 V (Hg/HgO)	81.6% (1–10 A g <sup>-1</sup> )		144
CC/Co <sub>9</sub> S <sub>8</sub> /PPy	429 F g <sup>-1</sup> at 1 mA cm <sup>-2</sup>	2 M KOH	–0.2–0.6 V (SCE)	66.6% (1–16 mA cm <sup>-2</sup> )	83.5% (2500)	145
rGO@CuCo <sub>2</sub> S <sub>4</sub> @CoS <sub>2</sub> /NF	2447.1 F g <sup>-1</sup> at 1 A g <sup>-1</sup>	6 M KOH	0–0.5 V (Hg/HgO)	55.2% (1–10 A g <sup>-1</sup> )	79.2% (10 000)	146
CoS/NC	789 F g <sup>-1</sup> at 1 A g <sup>-1</sup>	6 M KOH	0–0.5 V (Hg/HgO)	80.2% (1–20 A g <sup>-1</sup> )	92.8% (10 000)	147
MoS <sub>2</sub> @CoS <sub>2</sub>	950 F g <sup>-1</sup> at 1 A g <sup>-1</sup>	2 M KOH	–0.2–0.8 V (SCE)	75.6% (1–10 A g <sup>-1</sup> )	94.6% (10 000)	148
N-Co <sub>3</sub> S <sub>4</sub> -GN/CNT	1158 F g <sup>-1</sup> at 1 A g <sup>-1</sup>	6 M KOH	0–0.6 V (Hg/HgO)	86% (1–10 A g <sup>-1</sup> )	97.2% (4000)	149
Co-NTC@Co <sub>3</sub> S <sub>4</sub>	3117.3 F g <sup>-1</sup> at 1 A g <sup>-1</sup>	1 M KOH	0–0.45 V (SCE)	80% (1–10 A g <sup>-1</sup> )	87% (1000)	150
NiS <sub>2</sub> /CoS <sub>2</sub> @C	1373 C g <sup>-1</sup> at 1 A g <sup>-1</sup>	6 M KOH	0–0.7 V (SCE)	68.6% (1–20 A g <sup>-1</sup> )	100.2% (10 000)	151
V <sub>2</sub> O <sub>5</sub> @Co <sub>3</sub> S <sub>4</sub>	1493.6 F g <sup>-1</sup> at 1 A g <sup>-1</sup>	2 M KOH	0–0.5 V (SCE)	57.9% (1–20 A g <sup>-1</sup> )	75.1% (7000)	152
CoNi <sub>2</sub> S <sub>4</sub> /MXene	751 C g <sup>-1</sup> at 1 A g <sup>-1</sup>	3 M KOH	0–0.7 V	73.2% (1–10 A g <sup>-1</sup> )	72.1% (5000)	153
Co <sub>3</sub> S <sub>4</sub> @CoCH/NF	2697.1 F g <sup>-1</sup> at 2 A g <sup>-1</sup>	3 M KOH	–0.05–0.55 V (SCE)	84.4% (2–20 A g <sup>-1</sup> )	79.8% (8000)	154
NiCo <sub>2</sub> S <sub>4</sub> /Co <sub>3</sub> S <sub>4</sub>	8.43 F cm <sup>-2</sup> at 2 mA cm <sup>-2</sup>	3 M KOH	0–0.7 V (SCE)	24.9% (2–50 mA cm <sup>-2</sup> )	60% (5000)	155
Co <sub>4</sub> S <sub>3</sub> /Ni <sub>3</sub> S <sub>2</sub> @MoS <sub>2</sub>	1238 F g <sup>-1</sup> at 1 A g <sup>-1</sup>	1 M KOH	–0.1–0.8 V (Ag/AgCl)	56.9% (1–8 A g <sup>-1</sup> )	85% (2000)	156
NF/FeNi <sub>2</sub> S <sub>4</sub> @Co <sub>9</sub> S <sub>8</sub> -rGO	1308 C g <sup>-1</sup> at 1 A g <sup>-1</sup>	6 M KOH	0–0.7 V (Ag/AgCl)	83.6% (1–36 A g <sup>-1</sup> )	93.75 (8500)	157
CoS <sub>2</sub> @C	1151 F g <sup>-1</sup> at 1 A g <sup>-1</sup>	2 M KOH	0–0.6 V (SCE)	73.4% (1–10 A g <sup>-1</sup> )	85.58% (10 000)	158
Ni(OH) <sub>2</sub> /CoS/CC	561.6 mA h g <sup>-1</sup> at 1 A g <sup>-1</sup>	2 M KOH	0–0.8 V (Hg/HgO)	70.8% (1–32 A g <sup>-1</sup> )		159
NiCo <sub>2</sub> S <sub>4</sub>	408 mA h g <sup>-1</sup> at 1 A g <sup>-1</sup>	6 M KOH	0–0.6 V (Hg/HgO)	51.1% (1–20 A g <sup>-1</sup> )	84.3% (10 000)	160
rGO/NiCo <sub>2</sub> S <sub>4</sub>	171 mA h g <sup>-1</sup> at 1 A g <sup>-1</sup>	2 M KOH	0–0.7 V (Hg/HgO)	71.3% (1–10 A g <sup>-1</sup> )	85% (2000)	161
CoS <sub>2</sub> @gC/rGO	1188 F g <sup>-1</sup> at 1 A g <sup>-1</sup>	1 M KOH	0–0.4 V (Ag/AgCl)	57% (1–20 A g <sup>-1</sup> )	76% (10 000)	162
CoS <sub>x</sub> @CoNi <sub>2</sub> S <sub>4</sub> /CC	1970 F g <sup>-1</sup> at 1 A g <sup>-1</sup>	1 M KOH	0–0.6 V (Hg/HgO)	92% (1–10 A g <sup>-1</sup> )		163
Co <sub>9</sub> S <sub>8</sub> @ZnGa <sub>2</sub> S <sub>4</sub>	1018 C g <sup>-1</sup> at 5 mA cm <sup>-2</sup>	3 M KOH	–0.05–0.55 V (Hg/HgO)	65% (5–187.5 mA cm <sup>-2</sup> )	93.5% (10 000)	164
Ni–Co–Mo–S/CNT	1728.6 F g <sup>-1</sup> at 1 A g <sup>-1</sup>	2 M KOH	–0.1–0.8 V (Hg/HgO)	55.8% (1–10 A g <sup>-1</sup> )		165
HN <sub>2</sub> CMS	928.1 C g <sup>-1</sup> at 1 A g <sup>-1</sup>	3 M KOH	0–0.7 V (Hg/HgO)	52.3% (1–10 A g <sup>-1</sup> )	85% (5000)	166
HCCoS@CNT	1250 F g <sup>-1</sup> at 0.5 A g <sup>-1</sup>	3 M KOH	0–0.5 V (SCE)	69.6% (1–10 A g <sup>-1</sup> )	90.4% (10 000)	167
Co <sub>3</sub> S <sub>4</sub> /NiS <sub>2</sub> /Cu <sub>2</sub> S	464.16 C g <sup>-1</sup> at 1 A g <sup>-1</sup>	6 M KOH	0–0.5 V (Ag/AgCl)			168
CoNi <sub>2</sub> S <sub>4</sub> /carbon/MXene	1221.6 F g <sup>-1</sup> at 1 A g <sup>-1</sup>	6 M KOH	0–0.6 V (Hg/HgO)	79.1% (1–20 A g <sup>-1</sup> )	63.96% (10 000)	40
Ni <sub>3</sub> S <sub>4</sub> @Co <sub>3</sub> S <sub>4</sub>	747.3 C g <sup>-1</sup> at 1 A g <sup>-1</sup>	6 M KOH	0–0.6 V (Hg/HgO)	77% (1–10 A g <sup>-1</sup> )		169
NiCo <sub>2</sub> S <sub>4</sub> /MXene/NC	1786 F g <sup>-1</sup> at 1 A g <sup>-1</sup>	3 M KOH	–0.2–0.7 V (Hg/HgO)	52% (1–40 A g <sup>-1</sup> )	110.5% (10 000)	170
MoS <sub>2</sub> /Co <sub>3</sub> S <sub>4</sub> /NPC	612 F g <sup>-1</sup> at 1 mV s <sup>-1</sup>	1 M KOH	0–0.45 V (Ag/AgCl)		88.59% (9000)	171
Co <sub>3</sub> S <sub>4</sub>	668 F g <sup>-1</sup> at 1 A g <sup>-1</sup>	1 M KOH	0–0.7 V (SCE)	52.8% (1–10 A g <sup>-1</sup> )	86.4% (5000)	172
CoNiS	598.8 C g <sup>-1</sup> at 1 A g <sup>-1</sup>	6 M KOH	0–0.5 V (Hg/HgO)	59.9% (1–30 A g <sup>-1</sup> )	70.1% (10 000)	173
Co <sub>3</sub> S <sub>4</sub> –Mo <sub>15</sub> S <sub>19</sub>	3283 F g <sup>-1</sup> at 1 A g <sup>-1</sup>	2 M KOH	0–0.5 V (Ag/AgCl)	77.7% (1–10 A g <sup>-1</sup> )	77% (2500)	174
Au/ZnS@Co <sub>3</sub> S <sub>4</sub> @Ni <sub>3</sub> S <sub>2</sub>	302.6 mA h g <sup>-1</sup> at 1 A g <sup>-1</sup>	3 M KOH	0–0.6 V (SCE)	70.3% (1–10 A g <sup>-1</sup> )		175
ZnCo <sub>2</sub> S <sub>4</sub> @ZIF-67	447.25 F g <sup>-1</sup> at 1 A g <sup>-1</sup>	1 M KOH	–0.1–0.6 V (Hg/HgO)	40.3% (1–7 A g <sup>-1</sup> )		176
CoNi <sub>2</sub> S <sub>4</sub> /C-CNTs	1314.6 C g <sup>-1</sup> at 1 A g <sup>-1</sup>	2 M KOH	0–0.6 V (Hg/HgO)	72.1% (1–20 A g <sup>-1</sup> )	78% (10 000)	177
P–Co <sub>3</sub> S <sub>4</sub> HNCs	499.1 C g <sup>-1</sup> at 1 A g <sup>-1</sup>	6 M KOH	0–0.55 V (Hg/HgO)		88.6% (5000)	178
MoS <sub>2</sub> /CoMoS <sub>4</sub> /C	426.5 F g <sup>-1</sup> at 1 A g <sup>-1</sup>	2 M KOH	0–0.6 V (Hg/HgO)	73.3% (1–20 A g <sup>-1</sup> )	93% (10 000)	179
MoNiCo–S	3125.1 F g <sup>-1</sup> at 1 A g <sup>-1</sup>	2 M KOH	0–0.7 V (Hg/HgO)	47.6% (1–30 A g <sup>-1</sup> )	72.9% (5000)	180
S-hollow ZIF-67 and NiCo-LDH	3744.4 F g <sup>-1</sup> at 1 A g <sup>-1</sup>	6 M KOH	–0.2–0.6 V (Hg/HgO)	68.6% (1–10 A g <sup>-1</sup> )	82% (3000)	181
Mo–CoS <sub>2</sub>	1382.6 F g <sup>-1</sup> at 0.5 A g <sup>-1</sup>	6 M KOH	0–0.7 V (Hg/HgO)	49.0% (0.5–10 A g <sup>-1</sup> )	75.75% (1000)	182

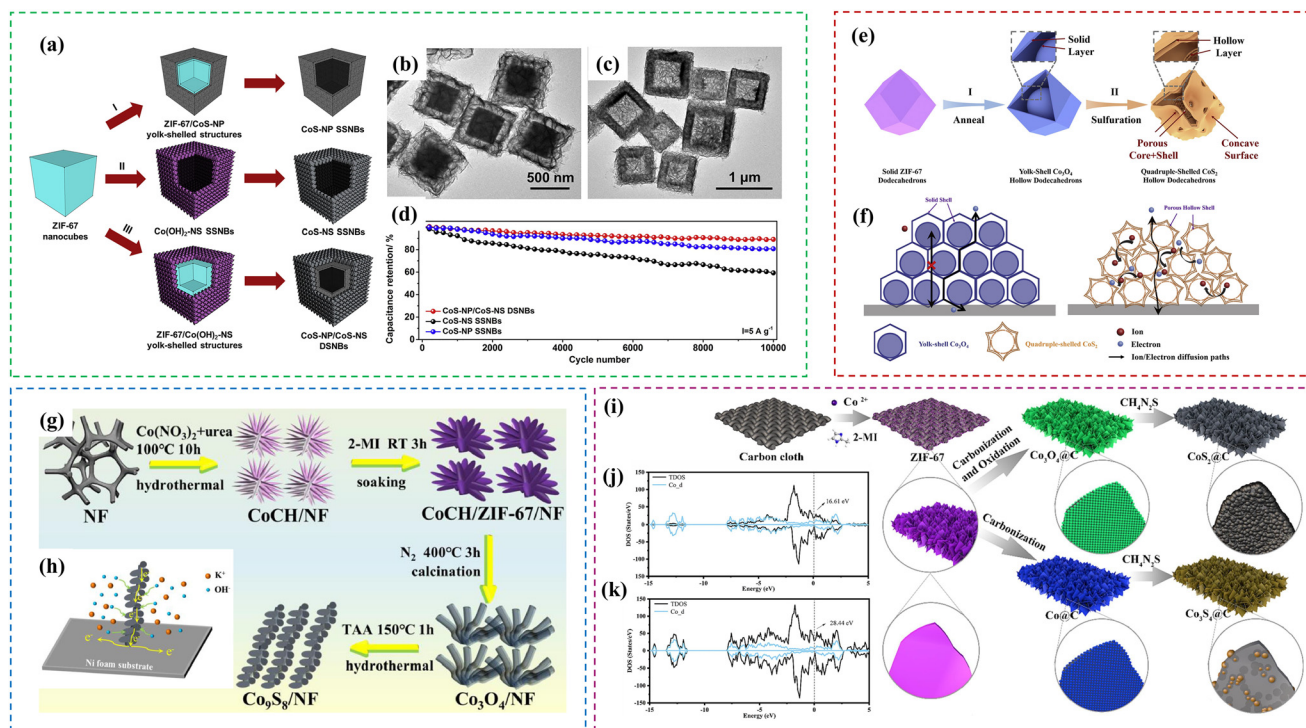
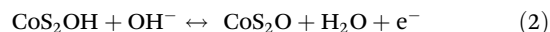
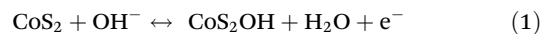


**Fig. 9** (a) Procedure for the synthesis of CoS-NP SSNBs, CoS-NS SSNBs and CoS-NP/CoS-NS DSNBs; (b) TEM image of ZIF-67/Co(OH)<sub>2</sub>-NS yolk-shell structures; (c) TEM image of CoS-NP/CoS-NS DSNBs; and (d) comparison of the cycling performance of the three CoS hollow nanostructures at 5 A g<sup>-1</sup>. Reprinted with permission from ref. 114, Copyright 2016, Elsevier Inc. (e) Schematic of the fabrication of quadruple-shelled CoS<sub>2</sub> hollow dodecahedron electrode; (f) schematic of the reasons for the enhanced performance of quadruple-shelled CoS<sub>2</sub> hollow dodecahedrons compared with yolk-shell Co<sub>3</sub>O<sub>4</sub> hollow dodecahedrons. Reprinted with permission from ref. 121, Copyright 2019, Elsevier Ltd. (g) Schematic of the synthetic process of Co<sub>9</sub>S<sub>8</sub>/NF and (h) schematic structure and mechanism of Co<sub>9</sub>S<sub>8</sub>/NF. Reprinted with permission from ref. 136, Copyright 2021, Elsevier Ltd. (i) Process for the construction of CoS<sub>2</sub> and Co<sub>3</sub>S<sub>4</sub> and total density of states (TDOS) of (j) Co<sub>3</sub>S<sub>4</sub> and (k) CoS<sub>2</sub>. Reprinted with permission from ref. 158, Copyright 2022, Elsevier Ltd.

mation of hierarchical pores and small active powder. Also, it is beneficial to provide a large surface area and short diffusion channels, as shown in Fig. 9h, which can reduce the volume expansion and ensure the stability of the architecture. ZIF-derived Co<sub>9</sub>S<sub>8</sub> displayed a large specific capacitance because of its abundant redox sites and high electrical conductivity. The Co<sub>9</sub>S<sub>8</sub>/NF electrode possessed outstanding electrochemical properties with the specific capacitance of 369.1 mA h g<sup>-1</sup> at 1 A g<sup>-1</sup> and 75.5% retention at 20 A g<sup>-1</sup>. After 5000 cycles, it showed 75% capacitance retention at 20 A g<sup>-1</sup>. Furthermore, a button-type asymmetric supercapacitor (ASC) was assembled with Co<sub>9</sub>S<sub>8</sub>/NF as the positive electrode, which displayed the maximum specific energy of 48.2 W h kg<sup>-1</sup> at the specific power of 799.8 W kg<sup>-1</sup> and excellent cycling life with 77% retention of its initial capacitance after 5000 cycles. Wang *et al.*<sup>147</sup> applied chemical vapor deposition (CVD) treatment to obtain a CoS/nitrogen-doped carbon (CoS/NC) composite with a hollow cage-like polyhedron structure formed by the combination of CoS nanosheets and nitrogen-doped carbon skeleton. It exhibited a specific capacitance of 789 F g<sup>-1</sup> at a current density of 1 A g<sup>-1</sup> and a rate capacity of 80.2% at a current density of 20 A g<sup>-1</sup>. The CoS/NC-700//AC capacitor showed the highest energy density of 32.8 W h kg<sup>-1</sup> when the power density was 620.0 W kg<sup>-1</sup> and it retained 89.2% of its

initial capacitance after 10 000 charge-discharge cycles at a current density of 5 A g<sup>-1</sup>. Meanwhile, Wei *et al.*<sup>158</sup> constructed CoS<sub>2</sub> and Co<sub>3</sub>S<sub>4</sub> nanoparticles anchored on a carbon skeleton (CoS<sub>2</sub>@C and Co<sub>3</sub>S<sub>4</sub>@C) depending on if an oxidation process occurred, respectively (Fig. 9i). The reactions are represented by the following equations:



Compared with the inhomogeneous distribution of Co<sub>3</sub>S<sub>4</sub>@C nanoparticles, a larger specific surface area is provided by numerous CoS<sub>2</sub>@C nanoparticles embedded in the 2D carbon skeleton and connected into sheets through effectively morphological construction, which provides more redox channels and active sites for electrochemical reactions. Thus, the CoS<sub>2</sub>@C electrode presented a superior electrochemical performance with a high specific capacitance of 1151 F g<sup>-1</sup> at 1 A g<sup>-1</sup>, which is 1.69-times larger than that of Co<sub>3</sub>S<sub>4</sub>@C. Comparing Fig. 9j and k, density functional theory (DFT) calculations illustrated that CoS<sub>2</sub> can transfer much more charge and has higher electronic activity in the process of OH<sup>-</sup> adsorption compared with Co<sub>3</sub>S<sub>4</sub>, proving that CoS<sub>2</sub> has better conductivity. Moreover, an asymmetric supercapacitor was con-

structed using  $\text{CoS}_2$ @C//reduced graphene oxide (RGO), which displayed a high energy density of  $46.52 \text{ W h kg}^{-1}$  at a power density of  $800 \text{ W kg}^{-1}$ .

### 3.2 Multi-metal sulfides

Alternatively, multi-metal sulfides have richer redox-active sites, higher electronic conductivity and synergistic effects between different metal ions. Therefore, numerous studies have been devoted to designing multi-metal sulfides using ZIF-67 as a template. For instance, the Ni ion, similar to the Co ion, is usually used as a dopant ion to obtain multi-metal chalcogenides derived from ZIF-67. Guo *et al.*<sup>116</sup> reported the growth of well-aligned  $\text{NiCo}_2\text{S}_4$  (shown in Fig. 10a–c) and  $\text{CoS}_2$  nanoarrays with a hollow/porous configuration on a conductive matrix, which significantly increase the number of electroactive sites, shortened the charge/ion diffusion length, and enhanced the mass/electron transfer. Consequently, the obtained  $\text{NiCo}_2\text{S}_4$  possessed an excellent specific capacitance of  $939 \text{ C g}^{-1}$ , a fast charge/discharge rate, and a favorable life span. Similarly, Liu *et al.*<sup>120</sup> synthesized  $\text{NiCo}_2\text{S}_4$  hollow nanocages assembled by ultrathin nanosheets through a facile solid-state chemical sulfurization method, as shown in Fig. 10d. Also, as shown in Fig. 10e and f, the obtained hollow  $\text{NiCo}_2\text{S}_4$  possessed inner cavities and large ultrathin nanosheets for both short ion diffusion distance and rich interfacial active sites, which can dynamically speed up faradaic reactions. A specific capacitance of  $1232 \text{ F g}^{-1}$  was obtained at a current

density of  $2 \text{ A g}^{-1}$  for the  $\text{NiCo}_2\text{S}_4$  electrode. Notably, compared with Co–Ni LDH, as shown in Fig. 10g and h, the  $\text{NiCo}_2\text{S}_4$  electrode yielded an impressive rate capability and excellent cycling stability (80% capacitance retention after 8000 charge–discharge cycles), mainly due to its robust porous architecture and good electronic conductivity. The aqueous asymmetric supercapacitor assembled with  $\text{NiCo}_2\text{S}_4$  as the positive electrode also delivered a high energy density of  $41.4 \text{ W h kg}^{-1}$  at a power density of  $689.5 \text{ W kg}^{-1}$ . Moreover, Cai *et al.*<sup>125</sup> changed the order of the sulfidation and cation exchange to obtain  $\text{CoS}_x$  hollow cages first, and subsequently obtained  $\text{NiCo}_2\text{S}_4$  by adding  $\text{Ni}^{2+}$ , as shown in Fig. 10i and j. Compared with  $\text{CoS}_x$ , as shown in Fig. 10k and l, the  $\text{NiCo}_2\text{S}_4$  hollow cages exhibited an appealing capacitance of  $1382 \text{ F g}^{-1}$  at  $1 \text{ A g}^{-1}$ . Furthermore, asymmetric supercapacitors (ASCs) were fabricated with the synthesized  $\text{NiCo}_2\text{S}_4$  and active carbon (AC) as the electrodes. The ASCs showed an energy density of  $35.3 \text{ W h kg}^{-1}$  at a power density of  $750 \text{ W kg}^{-1}$  and outstanding cycling stability of 79% retention after 10 000 cycles.

In the case of other metal ions, Yang *et al.*<sup>122</sup> doped Mo in ZIF-67 in the presence of  $\text{Na}_2\text{MoO}_4$ , and subsequently obtained an Mo-doped CoS hollow nanocage structure (Mo-doped CoS HNC) *via* a sulfurization process. As shown in Fig. 11a–d, the obtained Mo-doped CoS HNC exhibited an enhanced specific capacitance ( $781.0 \text{ F g}^{-1}$  at  $0.5 \text{ A g}^{-1}$ ) compared with the control CoS HNC ( $387.1 \text{ F g}^{-1}$ ) and  $\text{CoMoO}_4\text{--Co(OH)}_2$  HNC ( $285.1 \text{ F g}^{-1}$ ). Furthermore, it also showed a

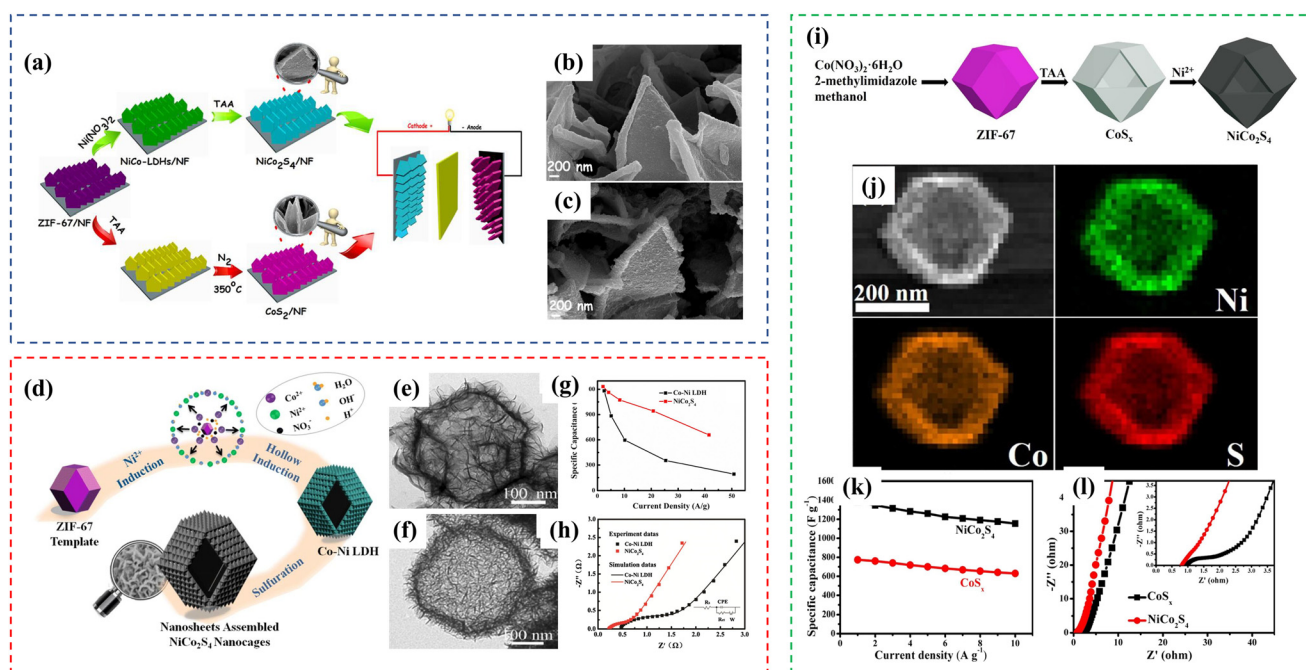


**Fig. 10** (a) Schematic of the process for the synthesis of the composite and fabrication of the asymmetric supercapacitor and SEM images of (b)  $\text{NiCo-LDHs}$  and (c)  $\text{NiCo}_2\text{S}_4$ . Reprinted with permission from ref. 116, Copyright 2018, the American Chemical Society. (d) Schematic of the fabrication of  $\text{NiCo}_2\text{S}_4$ ; TEM images of (e) Co–Ni LDH and (f)  $\text{NiCo}_2\text{S}_4$ ; (g) specific capacitance versus current density and (h) Nyquist plots of Co–Ni LDH and  $\text{NiCo}_2\text{S}_4$ . Reprinted with permission from ref. 120, Copyright 2019, Springer Nature. (i) Schematic showing the fabrication of  $\text{NiCo}_2\text{S}_4$  hollow cages; (j) EDS mapping of  $\text{NiCo}_2\text{S}_4$ ; (k) specific capacitance at different current densities and (l) Nyquist plots of  $\text{NiCo}_2\text{S}_4$  and  $\text{CoS}_x$ . Reprinted with permission from ref. 125, Copyright 2019, Elsevier B.V.



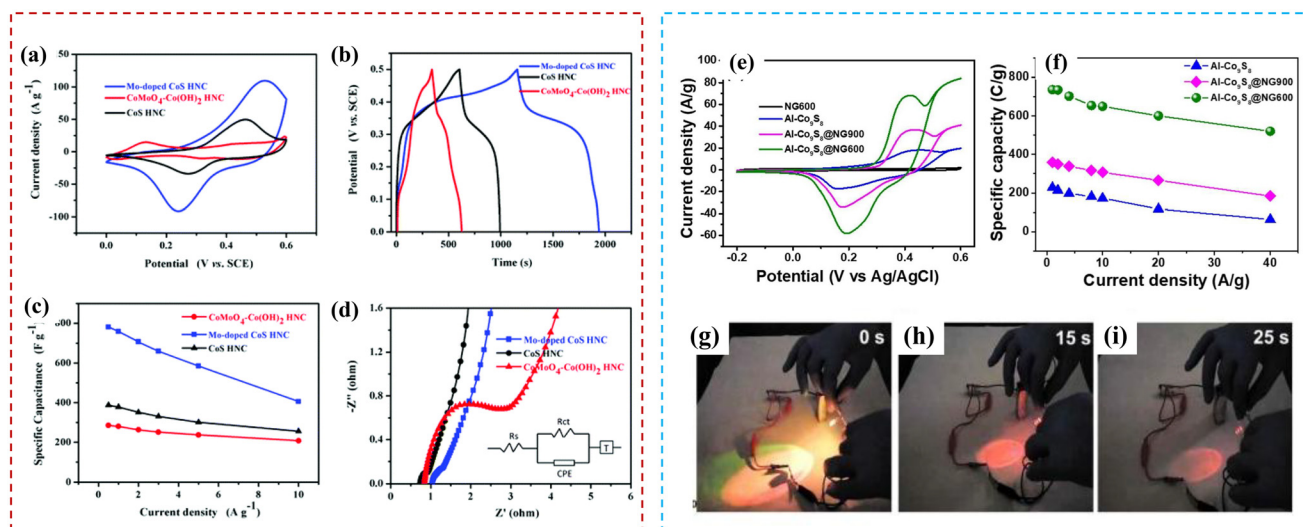


**Fig. 11** (a) CV curves, (b) GCD curves, (c) specific capacitance and (d) Nyquist plots of CoS HNC, CoMoO<sub>4</sub>-Co(OH)<sub>2</sub> HNC and Mo-doped CoS HNC. Reprinted with permission from ref. 122, Copyright 2019, The Royal Society of Chemistry. (e) CV curves and of NG600, Al-Co<sub>9</sub>S<sub>8</sub>, Al-Co<sub>9</sub>S<sub>8</sub>@NG600 and Al-Co<sub>9</sub>S<sub>8</sub>@NG900; (f) specific capacitance of Al-Co<sub>9</sub>S<sub>8</sub>, Al-Co<sub>9</sub>S<sub>8</sub>@NG600 and Al-Co<sub>9</sub>S<sub>8</sub>@NG900; (j–i) photographs of AsSC devices linked in series to light a red LED. Reprinted with permission from ref. 141, Copyright 2021, Elsevier B.V.

superior rate capacity of 52% at a 20-fold increase in current density (10 A g<sup>-1</sup>). The asymmetric supercapacitor (ASC) device assembled using the Mo-doped CoS HNC as the positive electrode and activated carbon (AC) as the negative electrode displayed a high energy density of 27.7 W h kg<sup>-1</sup> at a power density of 799.9 W kg<sup>-1</sup> with excellent cycling stability, maintaining 88% of its initial capacitance after 10 000 cycles. The excellent electrochemical performance is attributed to the unique ternary metal sulfide hollow nanocage structure having a large surface area, facile diffusion of ions, good conductivity, and rich redox reactions as well as the synergistic effect between Mo and Co ions. Also, Zhao *et al.*<sup>126</sup> presented the synthesis and characterization of ZIF-67-derived mesoporous copper cobalt sulfide (CuCo<sub>2</sub>S<sub>4</sub>) prepared *via* simple reflux and solvothermal reactions. The obtained CuCo<sub>2</sub>S<sub>4</sub> electrode showed a high specific capacity of up to 672 C g<sup>-1</sup> (1344 F g<sup>-1</sup>) at 1 A g<sup>-1</sup>. Additionally, Goda *et al.*<sup>141</sup> reported Al doping to improve the conductivity of cobalt sulfide. A novel type of core/shell architecture was successfully designed from aluminum-doped cobalt sulfide encapsulated by nitrogen-doped graphene (Al-doped Co<sub>9</sub>S<sub>8</sub>@NG) through the solvothermal/sulfuration of the ZIF-67 structure, subsequent wrapping with a PPy layer and calcination in argon gas at various temperatures. Interestingly, integrating the morphology and composition merits endowed the Al-doped Co<sub>9</sub>S<sub>8</sub>@NG600 electrode with highly enhanced supercapacitive features, as shown in Fig. 11e and f. The electrode attained a superior specific capacity of about 736 C g<sup>-1</sup> at an applied current density of 1 A g<sup>-1</sup>, ultra-long cycle stability of 92% after 10 000 cycles, and a remarkable retention rate (71%). Subsequently, a solid-state AsSC device with Al-doped Co<sub>9</sub>S<sub>8</sub>@NG core/shell as the positive electrode and activated PANI-derived carbon nanorods (ACNRs) as the negative electrode was assembled. The device exhibited

outstanding specific capacitance, energy density, and power density values of 134 F g<sup>-1</sup>, 53.3 W h kg<sup>-1</sup>, and 0.954 kW kg<sup>-1</sup>, respectively, with a considerable cycle life stability of 93% after consuming 10 000 cycles. Further, when two AsSC devices were linked in series, a multicolor LED could be lit for 25 s, demonstrating their availability for making modern portable electronics, as shown in Fig. 11g–i.

### 3.3 Composite materials

As mentioned, ZIF-67-derived sulfides usually exhibit the drawbacks of limited rate capability and poor cyclic stability. Accordingly, composite materials are being developed as promising electrode materials because rationally designed structures can improve the cycling stability and rate capability and facilitate electronic transport in electrodes.<sup>42</sup> Jian *et al.*<sup>117</sup> designed a hybrid structure of a cobalt sulfide nanocage derived from ZIF-67 and interconnected by carbon nanotubes (CNT/CoS). The carbon nanotube/ZIF-67 (CNT/ZIF-67) nanocomposites with controlled ZIF-67 particle sizes were systematically studied by varying the mass ratio of CNTs to ZIF-67 during crystallization, followed by subsequent sulfurization with thioacetamide (Fig. 12a). Benefiting from the porous nanocage architecture and conductive CNTs, the optimized CNT/CoS nanocage exhibited an excellent electrochemical performance with an outstanding specific capacitance (2173.1 F g<sup>-1</sup> at 5 A g<sup>-1</sup>) and high rate capability (65% retention at 20 A g<sup>-1</sup>), as shown in Fig. 12b and c. More importantly, the fabricated symmetric supercapacitor exhibited an energy density of 23.3 W h kg<sup>-1</sup> at a power density of 3382.2 W kg<sup>-1</sup> and impressive long-term stability (96.6% retention after 5000 cycles). Additionally, Zhou *et al.*<sup>140</sup> constructed hollow tube@sheet NiCo<sub>2</sub>S<sub>4</sub> core-shell nanoarrays by *in situ* growing ZIF-67 on Co-precursor nanorod arrays and sequentially performing

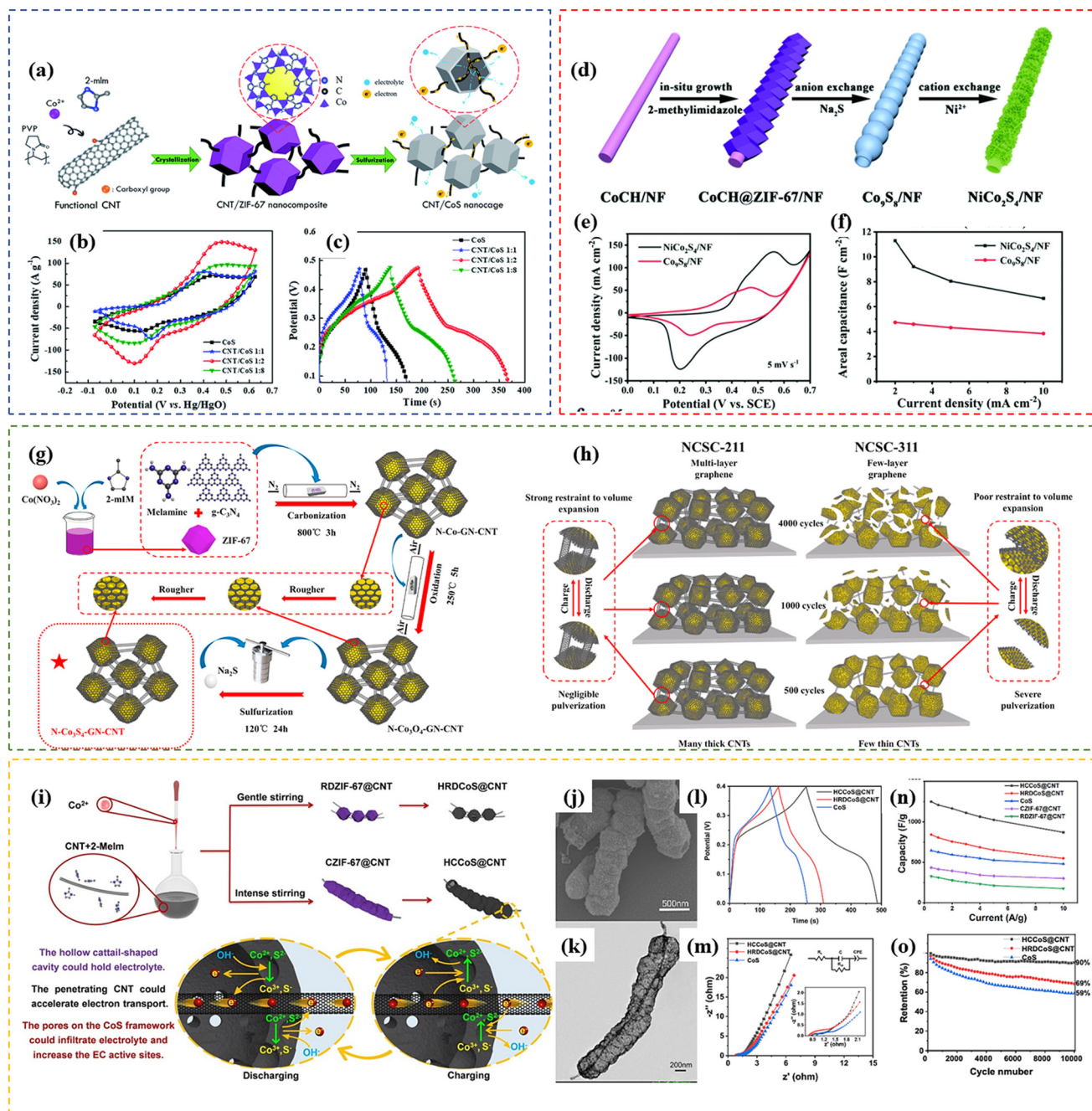


**Fig. 12** (a) Schematic of the synthesis of hybrid CNT/CoS nanocages; (b) CV curves at  $100 \text{ mV s}^{-1}$  and (c) GCD curves at  $5 \text{ A g}^{-1}$  for CoS, CNT/CoS (1:1), CNT/CoS (1:2) and CNT/CoS (1:8). Reprinted with permission from ref. 117, Copyright 2019, The Royal Society of Chemistry. (d) Synthetic procedure for  $\text{NiCo}_2\text{S}_4/\text{NF}$ ; (e) CV curves at  $5 \text{ mV s}^{-1}$  and (f) specific capacitance of  $\text{Co}_9\text{S}_8/\text{NF}$  and  $\text{NiCo}_2\text{S}_4/\text{NF}$ . Reprinted with permission from ref. 140, Copyright 2021, The Royal Society of Chemistry. (g) Schematic diagram of the construction of  $\text{N-Co}_9\text{S}_4\text{-GN/CNT}$  nanostructure and (h) schematic of the nanostructure changes in NCSC-211 and NCSC-311 after 500, 1000 and 4000 cycles. Reprinted with permission from ref. 149, Copyright 2022, Elsevier Ltd. (i) Schematic representation showing the various synthesis procedures for generating  $\text{CoS@CNT}$  structures and the electrochemical process occurring on hierarchical pore-structured  $\text{HCCoS@CNT}$ . Gentle stirring resulted in the formation of  $\text{HRDCoS@CNT}$  with a rhombic dodecahedron-shaped morphology by controlling the stirring speed to 200 rpm, while intense stirring resulted in the fabrication of  $\text{HCCoS@CNT}$  with a cattail-shaped morphology by controlling the stirring speed at 1000 rpm. (j) SEM image and (k) TEM image of  $\text{HCCoS@CNT}$  and (l) GCD curves at  $2 \text{ A g}^{-1}$ , (m) Nyquist plots, (n) specific capacitance and (o) cycling stability at  $10 \text{ A g}^{-1}$  of CoS,  $\text{HCCoS@CNT}$  and  $\text{HRDCoS@CNT}$ . Reprinted with permission from ref. 167, Copyright 2023, Elsevier B.V.

anion-exchange ( $\text{S}^{2-}$ ) and cation-exchange ( $\text{Ni}^{2+}$ ) (Fig. 12d). The well-defined nanostructures could shorten the ion transport path in the charging–discharging process and increase the specific surface area and electrochemical active sites, improving the electrochemical performance. Therefore, the unique tube@sheet  $\text{NiCo}_2\text{S}_4$  core–shell nanoarrays exhibited an intriguing electrochemical performance and showed an excellent areal capacitance of  $11.3 \text{ F cm}^{-2}$  ( $3227.94 \text{ F g}^{-1}$ ) at a current density of  $2 \text{ mA cm}^{-2}$  ( $2 \text{ A g}^{-1}$ ) (Fig. 12e and f). The assembled asymmetric supercapacitor device delivered a high energy density of  $0.42 \text{ mW h cm}^{-2}$  at a power density of  $2.1 \text{ mW cm}^{-2}$  and displayed outstanding cyclic stability (90.2% retention after 5000 cycles). Similarly, Zhang *et al.*<sup>149</sup> proposed a ZIF-67 derived, nitrogen-doped, graphene-coated and carbon nanotube-interlinked 3D  $\text{Co}_3\text{S}_4/\text{C}$  conductive network (N- $\text{Co}_3\text{S}_4$ -GN/CNT), as shown in Fig. 12g, for high-performance supercapacitors. By controlling the mass ratio of ZIF-67, melamine and g- $\text{C}_3\text{N}_4$ , various microstructures with determined electrochemical performances could be achieved. The nanocomposites synthesized with the component mass ratio of 2 : 1 : 1 (NCSC-211) were proven to have the most excellent comprehensive electrochemical properties, as shown in Fig. 12h. In the NCSC-211 nanostructure, multi-layer graphene functions as conductive shells for improving the cycling performance by alleviating the pulverization caused by volume change, the thick CNTs act as conductive bridges and agglomeration spacers, which increase the electron conductivity and provide more active sites for redox reaction, and doped-nitrogen offers enhanced electrolyte wettability and faster electron transfer. Consequently, the NCSC-211 electrode displayed a specific capacitance of  $1158 \text{ F g}^{-1}$  at  $1 \text{ A g}^{-1}$ , rate capability of 86% at  $10 \text{ A g}^{-1}$  and extraordinary cycling stability with 97.2% capacitive retention after 4000 cycles. Moreover, Li *et al.*<sup>165</sup> demonstrated the synthesis of Mo-ZIF-67/CNT composites through mechanical stirring and co-precipitation. After that, Ni, Co and Mo trimetallic sulfide/CNT composites (Ni–Co–Mo–S/CNT) were produced through further ion exchange/etching and vulcanization processes. The material had multiple valence states of three different metal ions, providing a large number of oxidation–reduction sites. The doping of CNTs endowed it with a unique coral-like structure, which helped to form its huge specific surface area and large mesopores. The electrode exhibited an impressive performance with a specific capacitance of  $1728.6 \text{ F g}^{-1}$  at a current density of  $1 \text{ A g}^{-1}$ . It also had a good rate capability, maintaining 55.8% of its specific capacitance when the current density increased tenfold. Moreover, Yan *et al.*<sup>167</sup> developed an *in situ* self-assembly strategy to prepare hollow composites using ZIF-67 and carbon nanotubes, and subsequently converted ZIF-67 to cobalt sulfide *via* a sulfurization strategy (Fig. 12i). The unique hollow composites with different dimensions, as shown in Fig. 12j and k, exhibited a synergistic effect between subunits, resulting in excellent electrochemical properties. The impact of particle cavity channel size on electrochemical properties was evaluated systematically. As a result, the obtained  $\text{CoS@CNT}$  with hollow cattail-shape structures ( $\text{HCCoS@CNT}$ ) exhibited a

high specific capacitance ( $1250 \text{ F g}^{-1}$ ) and cyclic stability (90.4% for over 10 000 cycles at  $10 \text{ A g}^{-1}$ ) (as shown in Fig. 12l–o).

Besides carbon nanotubes, graphene is also a good conductive carbon material for improving the electrochemical properties of ZIF-67-derived transition metal sulfides. Wu *et al.*<sup>133</sup> reported the preparation of a sandwich-like  $\text{GO/CoS}_x\text{-rGO/GO}$  hybrid film *via* a three-step process and the resulting  $\text{rGO/CoS}_x\text{-rGO/rGO}$  hybrid film was shown to have a good electrochemical performance because it combined the good pseudocapacitor property of cobalt sulfide and good conductivity and electric double layer capacitor property of rGO. Similarly, Reddy *et al.*<sup>162</sup> added a calcination process and obtained  $\text{CoS}_2\text{@gC/rGO}$  by CVD treatment, as shown in Fig. 13a. The  $\text{CoS}_2\text{@gC/rGO}$  composite exhibited a specific capacitance of  $1188 \text{ F g}^{-1}$ , cyclic stability of 76% and 99% coulombic efficiency (Fig. 13b–d). An all-solid-state asymmetric supercapacitor device was fabricated with  $\text{CoS}_2\text{@gC/rGO}$  and hydrothermally reduced graphene oxide (hrGO) as the positive and negative electrodes, respectively. The device exhibited a high specific capacitance of  $233 \text{ F g}^{-1}$  at a current density of  $1.5 \text{ A g}^{-1}$  and delivered a high energy density of  $82.88 \text{ W h kg}^{-1}$  at a power density of  $1199.56 \text{ W kg}^{-1}$ . Particularly, the device conserved an energy density of  $42.44 \text{ W h kg}^{-1}$  even at a high-power density of  $7999.9 \text{ W kg}^{-1}$ . Additionally, it showed good cyclic stability after 10 000 cycles of repeated charging/discharging, suggesting its potential for practical supercapacitor applications. Moreover, Wu *et al.*<sup>161</sup> designed the  $\text{rGO/NiCo}_2\text{S}_4$  material by using GO and ZIF-67 as the template and precursor, which increased the specific surface area and provided active sites for redox reactions and shortened ion transport pathways. The synthesized  $\text{rGO-10/NiCo}_2\text{S}_4$  exhibited excellent electrochemical properties as an electrode material, which had a high specific capacity of  $171 \text{ mA h g}^{-1}$  and  $121.9 \text{ mA h g}^{-1}$  ( $1 \text{ A g}^{-1}$  and  $10 \text{ A g}^{-1}$ ). The as-obtained  $\text{rGO-10/NiCo}_2\text{S}_4\text{//AC}$  asymmetric supercapacitor (ASC) delivered a power density of  $870 \text{ W kg}^{-1}$  at the specific energy of  $41 \text{ W h kg}^{-1}$ , with 88.2% capacitance retention after 5000 cycles at  $5 \text{ A g}^{-1}$ .

As a representative member of the emerging 2D MXenes,  $\text{Ti}_3\text{C}_2\text{T}_x$ -based supercapacitor materials have been comprehensively reviewed and demonstrated to be beneficial for the conductivity and the structural stability of ZIF-67-derived transition metal sulfides.<sup>183</sup> For example, Ruan *et al.*<sup>137</sup> synthesized  $\text{Ti}_3\text{C}_2$  MXene-wrapped  $\text{CoNi}_2\text{S}_4$  nanosheets grown on nickel foam, as shown in Fig. 14a and b, which delivered a very high specific capacity of  $933 \text{ C g}^{-1}$  at  $1 \text{ A g}^{-1}$  and good rate performance (Fig. 14c) due to the fact that the unique dendrite morphology can provide many exposed electro-active sites and the wrapped conductive MXene can facilitate charge transfer. An asymmetric supercapacitor was assembled using  $\text{CoNi}_2\text{S}_4/\text{MXene/NF}$  and RGO as positive and negative electrodes, respectively, which delivered a high energy density of  $30.5 \text{ W h kg}^{-1}$  without deteriorating its high power density ( $1587 \text{ W kg}^{-1}$ ). Also, Luo *et al.*<sup>144</sup> obtained  $\text{Co}_3\text{S}_4/\text{Ti}_3\text{C}_2\text{T}_x$  powder by hydrothermal reaction and the electrode containing  $\text{Co}_3\text{S}_4/\text{Ti}_3\text{C}_2\text{T}_x$  as the active material exhibited a very high specific



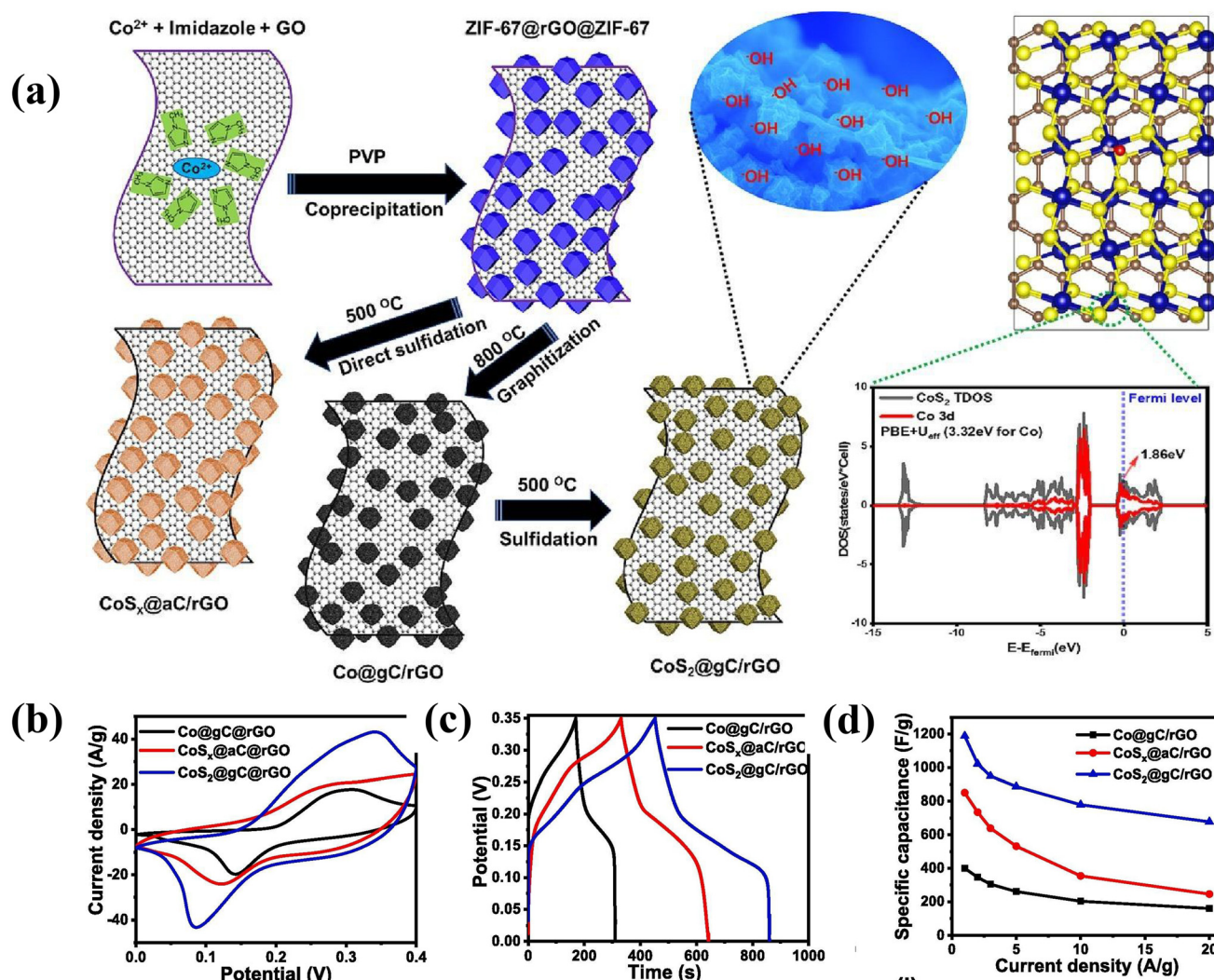
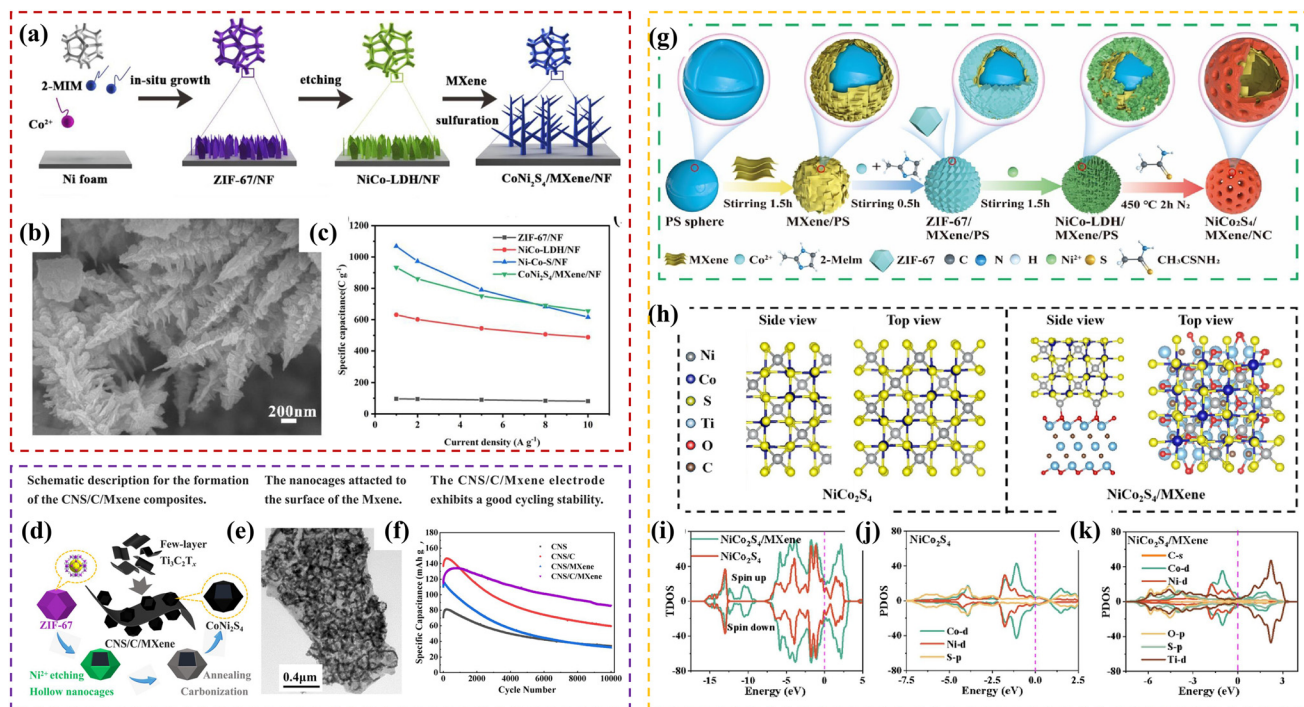


Fig. 13 (a) Schematic of the synthesis of  $\text{CoS}_2\text{@gC/rGO}$ , the insert is optimized configuration of  $\text{CoS}_2(200)$  and total density of states (TDOS) with Co 3d contributions of  $\text{CoS}_2$  (blue and yellow colors represent Co and S atoms, respectively); and (b) CV curves at  $25 \text{ mV s}^{-1}$ , (c) GCD curves at  $1 \text{ A g}^{-1}$  and (d) specific capacitance of  $\text{Co@gC/rGO}$ ,  $\text{CoS}_x\text{@aC/rGO}$  and  $\text{CoS}_2\text{@gC/rGO}$ . Reprinted with permission from ref. 162, Copyright 2023 Elsevier B.V.

capacitance of  $602 \text{ F g}^{-1}$  at  $1 \text{ A g}^{-1}$ , which was 2.6-times higher than of the ZIF-67/ $\text{Ti}_3\text{C}_2\text{T}_x$ -containing electrode. The supercapacitor based on  $\text{Co}_3\text{S}_4/\text{Ti}_3\text{C}_2\text{T}_x$  maintained 81.6% of its original capacitance even at a current density of  $10 \text{ A g}^{-1}$ . Thus, the introduction of  $\text{Ti}_3\text{C}_2\text{T}_x$  in ZIF-67 not only improved the electrical conductivity of the hybrid material but also its structural stability, which acted as a support. The asymmetric  $\text{Co}_3\text{S}_4/\text{Ti}_3\text{C}_2\text{T}_x\text{//AC}$  supercapacitor (ASC) containing activated carbon (AC) as the anode showed a high energy density of  $44.9 \text{ W h kg}^{-1}$  at a power density of  $800.3 \text{ W kg}^{-1}$ . This ASC also demonstrated a high rate performance (79.2%) and excellent cycling stability (with 88.3% capacitance retention and 99.23% coulombic efficiency after 5000 cycles). Similarly, Qi *et al.*<sup>153</sup> reported that  $\text{CoNi}_2\text{S}_4/\text{MXene}$  derived from ZIF-67/MXene and  $\text{NiCo-LDH/MXene}$  exhibited an outperforming specific capacitance ( $751 \text{ C g}^{-1}$  at  $1 \text{ A g}^{-1}$ ), which was much higher than that of pure  $\text{CoNi}_2\text{S}_4$  ( $600 \text{ C g}^{-1}$  at  $1 \text{ A g}^{-1}$ ). An asymmetric super-

capacitor ( $\text{CoNi}_2\text{S}_4/\text{MXene}\text{//reduced graphene oxide (RGO)}$ ) was assembled, which delivered a high energy density of  $33.8 \text{ W h kg}^{-1}$  and excellent cycling performance. As shown in Fig. 14d, Jiao *et al.*<sup>40</sup> added a carbonization process to improve the conductivity and structural stability of the obtained  $\text{CoNi}_2\text{S}_4/\text{carbon/MXene}$  (Fig. 14e).  $\text{CoNi}_2\text{S}_4/\text{carbon/MXene}$  exhibited the specific capacitance of  $1221.6 \text{ F g}^{-1}$  ( $169.7 \text{ mA h g}^{-1}$ ) at  $1 \text{ A g}^{-1}$  and still maintained a high capacitance of  $966.4 \text{ F g}^{-1}$  ( $134.2 \text{ mA h g}^{-1}$ ) at  $20 \text{ A g}^{-1}$  (79.1% of the former), with a better cycling stability compared with other electrodes, as shown in Fig. 14f. After assembling it with activated carbon into an asymmetric supercapacitor, the device delivered a high energy density of  $19.82 \text{ W h kg}^{-1}$  at a power density of  $469.31 \text{ W kg}^{-1}$  and maintained about 71.17% of its initial capacitance after 30 000 cycles at a current density of  $20 \text{ A g}^{-1}$ , representing excellent cycle stability and rate capability. Moreover, Li *et al.*<sup>170</sup> fabricated hierarchical hollow core-shell microspheres



**Fig. 14** (a) Schematic of synthetic process for dendrite CoNi<sub>2</sub>S<sub>4</sub>/MXene/NF; (b) SEM image of CoNi<sub>2</sub>S<sub>4</sub>/MXene/NF; and (c) specific capacitance of ZIF-67/NF, NiCo-LDH/NF, Ni-Co-S/NF and CoNi<sub>2</sub>S<sub>4</sub>/MXene/NF. Reprinted with permission from ref. 137, Copyright 2021, Elsevier B.V. (d) Schematic description of the formation of the CNS/C/MXene composites; (e) TEM images of CNS/C/MXene; and (f) cycling stability of CNS, CNS/C, CNS/MXene and CNS/C/MXene. Reprinted with permission from ref. 40, Copyright 2024, Elsevier Ltd. (g) Schematic diagram of the preparation of NiCo<sub>2</sub>S<sub>4</sub>/MXene/NC; (h) constructed models of NiCo<sub>2</sub>S<sub>4</sub> and NiCo<sub>2</sub>S<sub>4</sub>/MXene for calculation; (i) TDOS of NiCo<sub>2</sub>S<sub>4</sub> and NiCo<sub>2</sub>S<sub>4</sub>/MXene; and PDOS of (j) NiCo<sub>2</sub>S<sub>4</sub> and (k) NiCo<sub>2</sub>S<sub>4</sub>/MXene. Reprinted with permission from ref. 170, Copyright 2024, Elsevier B.V.

of NiCo<sub>2</sub>S<sub>4</sub>/MXene/N-doped carbon (NiCo<sub>2</sub>S<sub>4</sub>/MXene/NC) using dual templates of polyethylene microspheres and ZIF-67 (Fig. 14g). The integration of MXene and N-doped carbon significantly enhanced the electronic conductivity of the electrode, while the construction of hollow spherical structures effectively alleviated the instability of NiCo<sub>2</sub>S<sub>4</sub>/NC during the charge-discharge cycles, leading to an excellent charge storage performance with a high specific capacitance (1786 F g<sup>-1</sup> at 1 A g<sup>-1</sup>) and impressive cycling stability (over 100% capacitance retention after 10 000 cycles). The corresponding hybrid supercapacitor displayed a high specific capacitance (190 F g<sup>-1</sup> at 1 A g<sup>-1</sup>) with a maximum energy density of 67 W h kg<sup>-1</sup> at 796 W kg<sup>-1</sup> and great cycling stability (over 80% capacitance retention after 10 000 cycles). As shown in Fig. 14h–k, density functional theory (DFT) calculations revealed that addition of MXene enhanced the conductivity of NiCo<sub>2</sub>S<sub>4</sub>.

Cheng *et al.*<sup>37</sup> inlaid Co<sub>3</sub>S<sub>4</sub> hollow nanocages (HNCs) derived from ZIF-67 on polypyrrole (PPy) tubes, forming a Co<sub>3</sub>S<sub>4</sub>-HNCs@PPy hybrid with intertwined “Co<sub>3</sub>S<sub>4</sub>-to-PPy-to-Co<sub>3</sub>S<sub>4</sub>” conductive networks *via* a facile solution method. The as-synthesized Co<sub>3</sub>S<sub>4</sub>-HNCs@PPy showed outstanding electrochemical activity (1706 F g<sup>-1</sup> at 1 A g<sup>-1</sup>) together with a high rate capability (73.2% retention at 10 A g<sup>-1</sup>), which was significantly superior to individual Co<sub>3</sub>S<sub>4</sub>-HNCs, PPy or a physical mixture of Co<sub>3</sub>S<sub>4</sub> and PPy. Remarkably, the asymmetric super-

capacitor based on Co<sub>3</sub>S<sub>4</sub>-HNCs@PPy delivered a high energy density of 50.5 W h kg<sup>-1</sup> (at 849.1 W kg<sup>-1</sup>) with high durability (82.8% retention after 10 000 cycles). The outstanding supercapacitor property can be attributed to the synergistic advantages of the intertwined “Co<sub>3</sub>S<sub>4</sub>-to-PPy-to-Co<sub>3</sub>S<sub>4</sub>” networks including rich reactive sites, shortened charge diffusion pathway and enhanced charge transfer and mechanical stability. Similarly, Zhao *et al.*<sup>134</sup> grew the ZIF-67-derived porous CoNi<sub>2</sub>S<sub>4</sub> on intercrosslinked PPy tubes to obtain the NiCoS@PPy hybrid *via* a solution sulfidation (as shown in Fig. 15a). The NiCoS@PPy electrode achieved an ultrahigh specific capacitance of 2316.6 and 1409.5 F g<sup>-1</sup> at 1 and 10 A g<sup>-1</sup>, largely outperforming the control NiCoS or NiCo-LDH@PPy (Fig. 15b–d). Furthermore, the fabricated ASC utilizing NiCoS@PPy as the cathode displayed an outstanding energy storage capability (34.4 W h kg<sup>-1</sup> at 799 W kg<sup>-1</sup>) and splendid cyclic life (retaining 84% initial capacitance after 8500 cycles). Additionally, Wu *et al.*<sup>145</sup> initially assembled ZIF-67 on carbon cloth, which was further hydrothermally converted to Co<sub>9</sub>S<sub>8</sub>, and subsequently PPy was coated on the surface of CC/Co<sub>9</sub>S<sub>8</sub> *via* an electrodeposition process. The obtained CC/Co<sub>9</sub>S<sub>8</sub>/PPy electrode showed 83.5% capacity retention after 2500 charge-discharge cycles due to the buffered volume change of Co<sub>9</sub>S<sub>8</sub> during the redox process by the introduction of the PPy shell. Moreover, Xu *et al.*<sup>132</sup> used polyaniline (PANI) as a growth substrate for ZIF-67 as a transfer



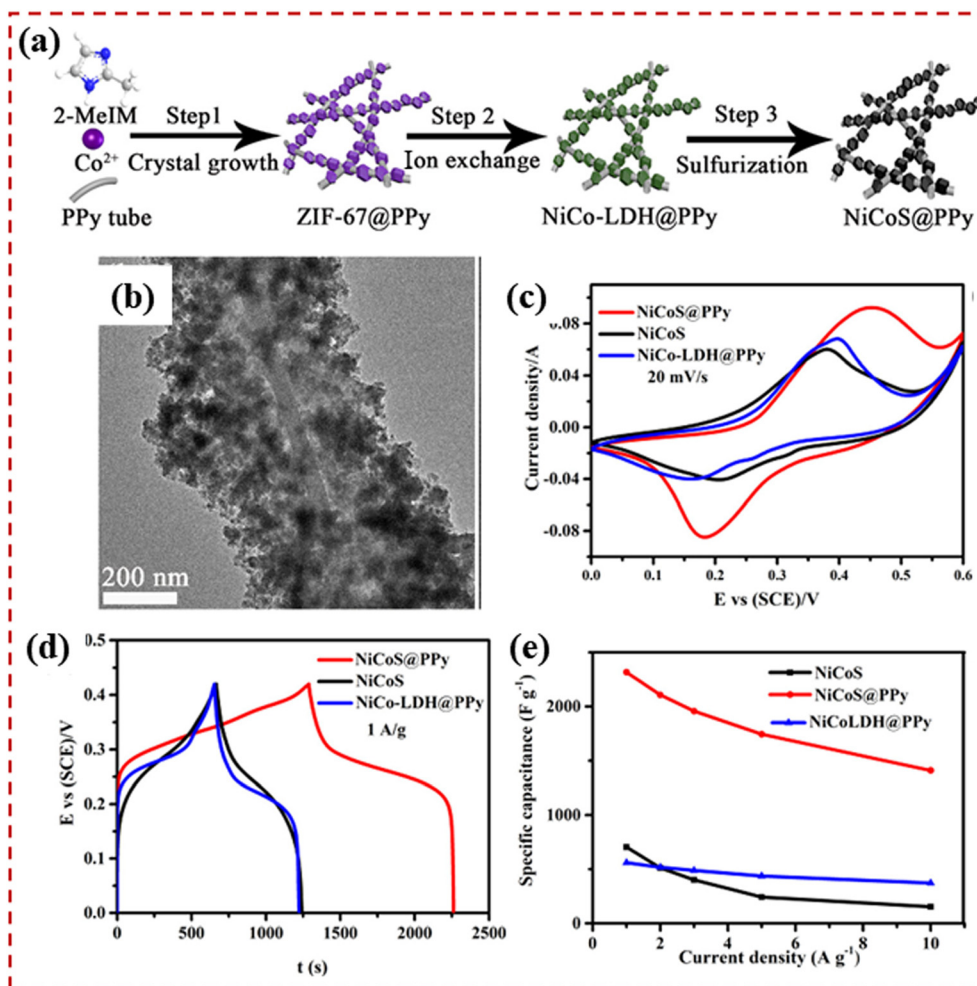


**Fig. 15** (a) Procedure for the preparation of porous NiCoS@PPy; (b) TEM image of NiCoS@PPy; (c) CV curves at 20 mV s<sup>-1</sup>, (d) GCD curves at 1 A g<sup>-1</sup> and (e) specific capacitance of NiCoS, NiCo-LDH@PPy and NiCoS@PPy. Reprinted with permission from ref. 134, Copyright 2021, the American Chemical Society.

scaffold of electrons and worked as a wire to connect nanoparticles, improving the conductivity of ZIF-67. The sulfides (Co<sub>3</sub>S<sub>4</sub>/PANI) obtained by sulfurization exhibited a high specific capacitance of up to 11 times that of ZIF-67 at 1 A g<sup>-1</sup>. Also, the assembled asymmetric supercapacitors (ASC) device exhibited a high specific energy of 40.75 W h kg<sup>-1</sup> at a specific power of 800 W kg<sup>-1</sup> and displayed super cycling stability. After 20 000 cycles of charge and discharge tests, it still maintained 88% of its initial capacitance at a higher current density of 5 A g<sup>-1</sup>.

Combining ZIF-67-derived transition metal sulfides with other compounds is an effective strategy to improve their electrochemical performance by taking advantage of their synergistic effect. Hou *et al.*<sup>115</sup> successfully fabricated a core-shell-structured Co<sub>9</sub>S<sub>8</sub>@N-C@MoS<sub>2</sub> nanocube through a sulfurization process based on ZIF. Due to their improved electrical conductivity and large surface area, the Co<sub>9</sub>S<sub>8</sub>@N-C@MoS<sub>2</sub> nanocubes with a core-shell heterostructure exhibited a better electrochemical performance in supercapacitors

compared with Co<sub>9</sub>S<sub>8</sub> and delivered a high specific capacitance of 410 F g<sup>-1</sup> at the current density of 10 A g<sup>-1</sup> after 20 000 cycles with excellent cycling stability (101.7% of the initial value). Similarly, Saha *et al.*<sup>174</sup> used ZIF-67 and Mo-precursor to obtain Co<sub>3</sub>S<sub>4</sub>-Mo<sub>15</sub>S<sub>19</sub> (CMS/NF) *via* one-pot hydrothermal sulfurization (Fig. 16a). The unique stellate-shaped architecture of the CMS/NF microflowers enhanced the exposure of the redox active sites, improving the charge storage and exhibiting superior performance. On account of the synergy of the metal ions and stellate-shaped hierarchical architecture, the CMS/NF hybrid sulfide showed an excellent specific capacitance value of 3283 F g<sup>-1</sup> at a current density of 1 A g<sup>-1</sup> with a capacitance retention of 77.7% at 10 A g<sup>-1</sup>. The asymmetric supercapacitor device based on CMS/NF hybrid sulfide with aqueous KOH electrolyte exhibited a high specific energy of 40.8 W h kg<sup>-1</sup> at 400 W kg<sup>-1</sup> with excellent cycling life of 81% after 5000 cycles with ~100% coulombic efficiency. Also, according to the total density of states, as shown in Fig. 16b and c, it was concluded that compared to



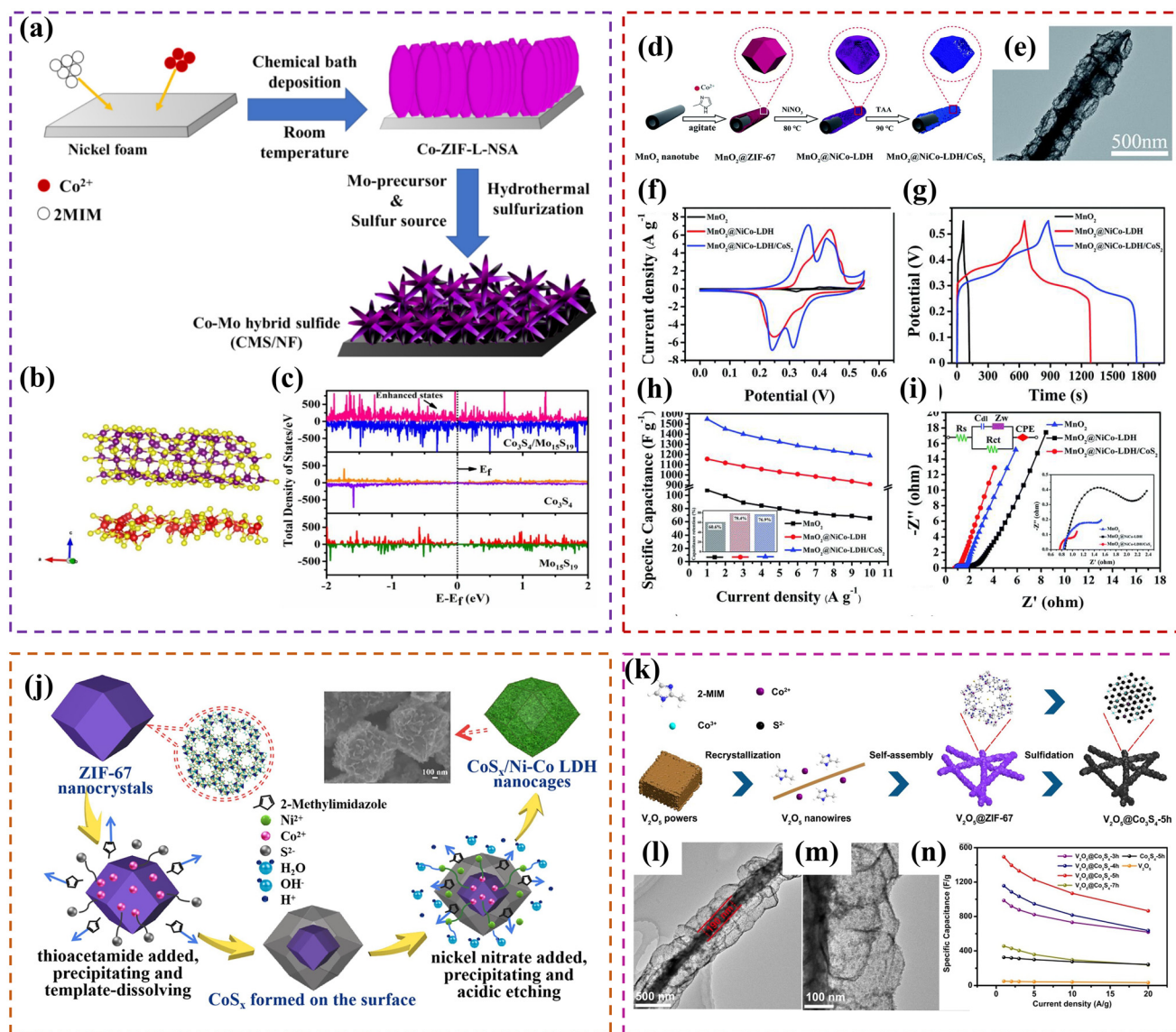


**Fig. 16** (a) Schematic of the synthesis process for CMS/NF; (b) DFT optimized structure of  $\text{Co}_3\text{S}_4\text{-Mo}_{15}\text{S}_{19}$ , where red, violet, and yellow colour represent Mo, Co, and S atoms, respectively; and (c) total density of states for (i) pristine  $\text{Mo}_{15}\text{S}_{19}$ , (ii) pristine  $\text{Co}_3\text{S}_4$ , and (iii)  $\text{Co}_3\text{S}_4\text{-Mo}_{15}\text{S}_{19}$  hybrid structure. Reprinted with permission from ref. 174, Copyright 2024, Elsevier Ltd. (d) Schematic diagram of the synthesis of  $\text{MnO}_2\text{@NiCo-LDH/CoS}_2$ ; (e) TEM image of  $\text{MnO}_2\text{@NiCo-LDH/CoS}_2$ ; (f) CV curves at  $1 \text{ mV s}^{-1}$ , (g) GCD curves at  $1 \text{ A g}^{-1}$ , (h) specific capacitance and (i) Nyquist plots of  $\text{MnO}_2$ ,  $\text{MnO}_2\text{@NiCo-LDH}$  and  $\text{MnO}_2\text{@NiCo-LDH/CoS}_2$ . Reprinted with permission from ref. 119, Copyright 2019, The Royal Society of Chemistry. (j) Schematic illustration of the fabrication process of  $\text{CoS}_x\text{/Ni-Co LDH}$  nanocages. Reprinted with permission from ref. 123, Copyright 2019 Elsevier B. V.; (k) schematic diagram showing the construction of  $\text{V}_2\text{O}_5\text{@Co}_3\text{S}_4$ ; (l and m) TEM images of  $\text{V}_2\text{O}_5\text{@Co}_3\text{S}_4$ ; and (n) specific capacitance of the  $\text{V}_2\text{O}_5$ ,  $\text{Co}_3\text{S}_4$ -5 h,  $\text{V}_2\text{O}_5\text{@Co}_3\text{S}_4$ -3 h,  $\text{V}_2\text{O}_5\text{@Co}_3\text{S}_4$ -4 h,  $\text{V}_2\text{O}_5\text{@Co}_3\text{S}_4$ -5 h and  $\text{V}_2\text{O}_5\text{@Co}_3\text{S}_4$ -7 h at  $1\text{--}20 \text{ A g}^{-1}$ . Reprinted with permission from ref. 152, Copyright 2022, Elsevier B.V.

the pristine structures, the hybrid system had enhanced states close to the Fermi level, confirming the improvement in conductivity.

Wang *et al.*<sup>119</sup> designed new one-dimensional hierarchical hollow nickel-cobalt layered double hydroxide nanocages assembled on  $\text{MnO}_2$  nanotubes with uniformly dispersed  $\text{CoS}_2$  nanoparticles,  $\text{MnO}_2\text{@NiCo-LDH/CoS}_2$ , using ZIF-67 as the template *via* multiple hydrothermal and sulfuration process, as shown in Fig. 16d. Fig. 16e shows the TEM image of

$\text{MnO}_2\text{@NiCo-LDH/CoS}_2$ . Compared with other electrode in Fig. 16f–i, the  $\text{MnO}_2\text{@NiCo-LDH/CoS}_2$  electrode materials have a high specific capacitance of  $1547 \text{ F g}^{-1}$  at a current density of  $1 \text{ A g}^{-1}$  and  $1189 \text{ F g}^{-1}$  at  $10 \text{ A g}^{-1}$ , exhibiting high rate performance (76.9%) and high stability (82.3%). Also, Zardkhoshoui *et al.*<sup>135</sup> synthesized nanosheet-assembled hollow  $\alpha\text{-MnS@Co}_3\text{S}_4$  spheres (NSH-MCS) with special morphology using ZIF-67 grown on manganese-glycerate (Mn-G) solid spheres as the precursor. The special structure can

provide rich mass/electron transfer channels, and meanwhile prevent the accumulation of nanosheets. Taking advantage of these great merits, the NSH-MCS-based electrode exhibited appealing electrochemical features including an impressive capacity value of 283.3 mA h g<sup>-1</sup> (1019.9 C g<sup>-1</sup>) at 1 A g<sup>-1</sup> with the desirable rate performance of 81.5% at 25 A g<sup>-1</sup> and significant longevity of 92.7% over 10 000 cycles at 15 A g<sup>-1</sup>. Also, the hybrid supercapacitor assembled with NSH-MCS as the positive electrode and AC (activated carbon) as the negative electrode exhibited a desirable performance, such as a good energy density (54.9 W h kg<sup>-1</sup> at 753 W kg<sup>-1</sup>) and excellent longevity of 90.5% after 10 000 cycles at 15 A g<sup>-1</sup>. Additionally, as shown in Fig. 16j, Guan *et al.*<sup>123</sup> prepared CoS<sub>x</sub>/Ni-Co LDH *via* the partial sulfuration of ZIF-67 and etching and precipitation of the added nickel ions. The prepared CoS<sub>x</sub>/Ni-Co LDH nanocages consisted of a hollow rhombic dodecahedral morphology with many nanosheet arrays on their shell. When used as the electrode material for electrochemical capacitors, the CoS<sub>x</sub>/Ni-Co LDH nanocages delivered a specific capacitance of 1562 F g<sup>-1</sup> at a current density of 1 A g<sup>-1</sup>. In addition, the asymmetric supercapacitor assembled with CoS<sub>x</sub>/Ni-Co LDH as the cathode and activated carbon (AC) as the anode showed a high energy density of 35.8 W h kg<sup>-1</sup> at a power density of 800 W kg<sup>-1</sup> and an excellent cycling performance with the retention rate of 94.56% after 10 000 cycles, suggesting its potential application in high-performance electrochemical capacitors. These exceptional electrochemical properties can be attributed to the unique structure and synergistic effects between the metal sulfide and the bimetallic hydroxide. Similarly, Wang *et al.*<sup>159</sup> directly grew ZIF-67-derived CoS with Ni(OH)<sub>2</sub> nanosheets on carbon cloth (Ni(OH)<sub>2</sub>/CoS/CC) and the composites possessed a superior performance (561.6 mA h g<sup>-1</sup> at 1 A g<sup>-1</sup>) to the Ni(OH)<sub>2</sub>/CC electrode (199.4 mA h g<sup>-1</sup>). The hybrid supercapacitor (HSC) with Ni(OH)<sub>2</sub>/CoS/CC as the cathode and activated carbon (AC) as

the anode (Ni(OH)<sub>2</sub>/CoS/CC//AC) provided a remarkable energy density of 90.8 W h kg<sup>-1</sup> at 800 W kg<sup>-1</sup> and maintained 59.7 W h kg<sup>-1</sup> even at 25 600 W kg<sup>-1</sup>, which is higher than that of most of the reported Ni(OH)<sub>2</sub>-related devices, and possessed a marvelous capacity retention of 92.2% over 10 000 charge-discharge cycles. The outstanding electrochemical performance of Ni(OH)<sub>2</sub>/CoS/CC was chiefly due to the mediation of the Co<sup>2+</sup>/Co<sup>3+</sup> redox cycle for the rapid conversion of Ni<sup>2+</sup> into Ni<sup>3+</sup>, which greatly boosted the charge-transfer efficiency in the supercapacitor and methanol electro-oxidation. Moreover, Xue *et al.*<sup>152</sup> used one-dimensional (1D) V<sub>2</sub>O<sub>5</sub> nanowires as a flexible backbone to string ZIF-67-derived hollow Co<sub>3</sub>S<sub>4</sub> three-dimensional (3D) nanopholyhedra to build robust core-shell 1D@3D V<sub>2</sub>O<sub>5</sub>@Co<sub>3</sub>S<sub>4</sub> nanocomposites (Fig. 16k). As shown in Fig. 16l and m, the 1D V<sub>2</sub>O<sub>5</sub> nanowires facilitated efficient electron transportation between the Co<sub>3</sub>S<sub>4</sub> nanopolyhedra. The hollow/porous structure of Co<sub>3</sub>S<sub>4</sub> not only afforded substantial electroactive sites, but also shortened the charge transport pathway. With these advantages, the optimal V<sub>2</sub>O<sub>5</sub>@Co<sub>3</sub>S<sub>4</sub>-5 h displayed enhanced electrochemical properties compared with the control V<sub>2</sub>O<sub>5</sub> or Co<sub>3</sub>S<sub>4</sub>-5 h in a three-electrode system, as shown in Fig. 16n. Furthermore, the asymmetric supercapacitor made from V<sub>2</sub>O<sub>5</sub>@Co<sub>3</sub>S<sub>4</sub>-5 h exhibited a high energy density (40.7 W h kg<sup>-1</sup> at 800 W kg<sup>-1</sup>) with outstanding cycle durability, maintaining 85.9% of its initial capacitance after 10 000 cycles.

## 4. ZIF-67-derived transition metal selenides

Similar to sulfides, ZIF-67-derived transition metal selenides also have the advantages of improved redox-active sites, high specific capacity, better electronic conductivity and thermal and mechanical stability (as shown in Table 3). Additionally,

**Table 3** Summary of the electrochemical characteristics of ZIF-67-derived selenide materials in three-electrode measurements

Electrode materials	Specific capacity	Electrolyte	Potential window (CV)	Capacity retention	Cyclic stability	Ref.
Co-Zn-Se@CNTs-CNFs	1891 F g <sup>-1</sup> at 1 A g <sup>-1</sup>	6 M KOH	0–0.7 V (Hg/HgO)	52.4% (1 to 30 A g <sup>-1</sup> )	97.2% (5000)	184
H-Ni-Co-Se	1175 F g <sup>-1</sup> at 1 A g <sup>-1</sup>	6 M KOH	–0.2–0.6 V (SCE)	72.8% (1 to 10 A g <sup>-1</sup> )	89.3% (2000)	185
NiSe <sub>2</sub> /CoSe <sub>2</sub>	1668 F g <sup>-1</sup> at 1 A g <sup>-1</sup>	3 M KOH	0–0.7 V (Hg/HgO)	82.8% (1 to 20 A g <sup>-1</sup> )	87.2% (5000)	186
P-(Ni, Co)Se <sub>2</sub>	755 C g <sup>-1</sup> at 2 mA cm <sup>-2</sup>	3 M KOH	0–0.6 V (Hg/HgO)	86.4% (2 to 30 mA cm <sup>-2</sup> )	80.1% (3000)	187
Ni <sub>1-x</sub> Co <sub>1-x</sub> Se <sub>2</sub> /CNFs/CoO@CC	207.8 mA h g <sup>-1</sup> at 1 A g <sup>-1</sup>	6 M KOH	0–0.5 V (Hg/HgO)		104.1% (5000)	188
CoSe <sub>2</sub> /GO	108.31 mA h g <sup>-1</sup> at 1 A g <sup>-1</sup>	2 M KOH	–0.2–0.6 V (SCE)	61.6% (1 to 10 A g <sup>-1</sup> )	91.2% (5000)	189
CoSe <sub>2</sub> /C	462 F g <sup>-1</sup> at 5 A g <sup>-1</sup>	2 M KOH	0–0.8 V (SCE)	63.3% (1 to 10 A g <sup>-1</sup> )	100% (10 000)	190
NiCoSe <sub>2</sub> /C	232.6 mA h g <sup>-1</sup> at 1 A g <sup>-1</sup>	2 M KOH	0–0.5 V (SCE)	72.6% (1 to 10 A g <sup>-1</sup> )	88.3% (5000)	191
CMS-DSHNCs	1029.8 C g <sup>-1</sup> at 2 A g <sup>-1</sup>	3 M KOH	–0.3–0.7 V (Ag/AgCl)	76.14% (2 to 50 A g <sup>-1</sup> )	95.2% (8000)	192
CoNiSe <sub>2</sub> /Fe-CoNiSe <sub>2</sub>	1091.2 C g <sup>-1</sup> at 1 A g <sup>-1</sup>	3 M KOH	0–0.5 V (Ag/AgCl)	55% (1 to 20 A g <sup>-1</sup> )	85% (5000)	193
MXene@CoSe <sub>2</sub> /Ni <sub>3</sub> Se <sub>4</sub>	283 mA h g <sup>-1</sup> at 1 A g <sup>-1</sup>	3 M KOH	0–0.5 V (Hg/HgO)	62% (1 to 10 A g <sup>-1</sup> )	80% (5000)	194
H-NiCoSe <sub>2</sub> /NC	1131 C g <sup>-1</sup> at 1 A g <sup>-1</sup>	3 M KOH	–0.1–0.8 V (Ag/AgCl)	59.2% (1 to 10 A g <sup>-1</sup> )	90.2% (6000)	195
CoSe <sub>2</sub>	269.4 mA h g <sup>-1</sup> at 1 A g <sup>-1</sup>	6 M KOH	0–0.5 V (Hg/HgO)	83.7% (1 to 20 A g <sup>-1</sup> )	83.4% (5000)	196
CoSe <sub>2</sub> /NC	554.4 F g <sup>-1</sup> at 1 A g <sup>-1</sup>	2 M KOH	0–0.8 V (Hg/HgO)	78% (1 to 10 A g <sup>-1</sup> )	92% (21 000)	197
CoSe/NC	746 F g <sup>-1</sup> at 2 mV s <sup>-1</sup>	3 M KOH	0–0.5 V (Ag/AgCl)	9.5% (2 to 50 mV s <sup>-1</sup> )	82.3% (4000)	198
M-(Ni, Co)-Se@CNFs/CC	378.9 mA h g <sup>-1</sup> at 1 A g <sup>-1</sup>	6 M KOH	0–0.5 V (Hg/HgO)	72.8% (1 to 10 A g <sup>-1</sup> )		199
CoSe <sub>2</sub> @NiMn-LDH@Cu <sub>1.6</sub> Se	7064 mF cm <sup>-2</sup> at 2 mA cm <sup>-2</sup>	6 M KOH	0–0.5 V (Hg/HgO)		80.11% (10 000)	200
CFP/PNCNF(Se <sub>10</sub> )/PEDOT@300	378.1 F g <sup>-1</sup> at 1 A g <sup>-1</sup>	1 M H <sub>2</sub> SO <sub>4</sub>	0–0.7 V (Ag/AgCl)	19% (1 to 32 A g <sup>-1</sup> )		33
60-MoSe <sub>2</sub> /(Ni,Co)Se <sub>2</sub>	359.9 mA h g <sup>-1</sup> at 1 A g <sup>-1</sup>	6 M KOH	0–0.6 V (Hg/HgO)	82.3% (1 to 10 A g <sup>-1</sup> )	83.7% (10 000)	201
NiSe/Ni <sub>3</sub> Se <sub>2</sub> /CoSe/MoSe <sub>2</sub>	15.49 F cm <sup>-2</sup> at 5 mA cm <sup>-2</sup>	6 M KOH	–0.2–0.8 V	55.1% (5 to 50 mA cm <sup>-2</sup> )	96.5% (10 000)	202

as a type of nucleophile, Se not only has a faster reaction speed with active oxygen but also is easier to be restored than the S–O bond due to the existence of a  $\pi$  bond in the Se–O bond, which effectively avoids the occurrence of permanent oxidation and improves the cycling stability of selenides.<sup>34</sup> Therefore, ZIF-67-derived transition metal selenides have attracted increasing attention in supercapacitor application.

#### 4.1 Single metal selenides

Shaikat *et al.*<sup>198</sup> synthesized CoSe/NC based on ZIF-67 as the precursor and varying amounts of selenium powder by high-temperature treatment. Compared with the other electrodes with different amounts of Se, CoSe-1 (ZIF-67:Se 1:1) showed an excellent electrochemical performance with the highest specific capacitance ( $746 \text{ F g}^{-1}$  at  $2 \text{ mV s}^{-1}$ ), showing a cyclic capability of 82.3% after 4000 cycles because of the optimized ratio of cobalt and selenium in it. At the same time, Wang *et al.*<sup>197</sup> obtained CoSe<sub>2</sub>/NC *via* a similar strategy at various temperatures. In a three-electrode system with 2 M KOH as the electrolyte, CoSe<sub>2</sub>/NC-1 h possessed a high capacity of  $554.4 \text{ F g}^{-1}$  at  $1 \text{ A g}^{-1}$  and excellent cycling stability (92% capacity retention after 21 000 cycles). In addition, a flexible solid-state supercapacitor was assembled with CoSe<sub>2</sub>/NC-1 h as the positive electrode and AC as the negative electrode. The power density was  $800 \text{ W kg}^{-1}$  at  $1 \text{ A g}^{-1}$ , and the cycling stability was tested at 91.53% after 6000 cycles at  $2 \text{ A g}^{-1}$ . Additionally,

Wei's group<sup>190</sup> grew CoSe<sub>2</sub> on carbon cloth using leaf-like ZIF-67 as the precursor by a two-step calcination method (Fig. 17a–c). The novel CoSe<sub>2</sub>/carbon (CoSe<sub>2</sub>/C) electrode showed an excellent electrochemical performance (Fig. 17d and e), with a specific capacitance of  $462 \text{ F g}^{-1}$  at a current density of  $5 \text{ A g}^{-1}$ , and 100% capacitance retention at  $10 \text{ A g}^{-1}$  after 10 000 cycles. Meanwhile, an asymmetric supercapacitor was assembled, which exhibited an energy density of  $20.6 \text{ W h kg}^{-1}$  with a power density of  $698.8 \text{ W kg}^{-1}$  and outstanding cycling stability. Moreover, Fan *et al.*<sup>196</sup> prepared porous CoSe<sub>2</sub> nanosheets on nickel foam *via* the hydrothermal method (Fig. 17f and g). The unique nanosheet array structure could provide a highly active surface, large superficial area and fast ion transport channels. This was mainly attributed to the fact that the reaction at different hydrothermal temperatures can provide different nanosheet structures. In addition, the incorporated ZIF-67 backbone provided a pathway for rapid electron transfer and accommodated the volume expansion of the selenide during charge–discharge processes. As shown in Fig. 17h–k, due to its distinct porous structure, the CoSe<sub>2</sub>-180 electrode showed a high specific capacity of  $269.4 \text{ mA h g}^{-1}$  at  $1 \text{ A g}^{-1}$  and a distinguished retention rate of 83.7% at  $20 \text{ A g}^{-1}$ . After 5000 cycles, the specific capacity was maintained at 83.4% of the initial value. Moreover, the asymmetric supercapacitor (ASC) device was assembled with CoSe<sub>2</sub>-180 as the positive electrode. It displayed a favorable electrochemical per-

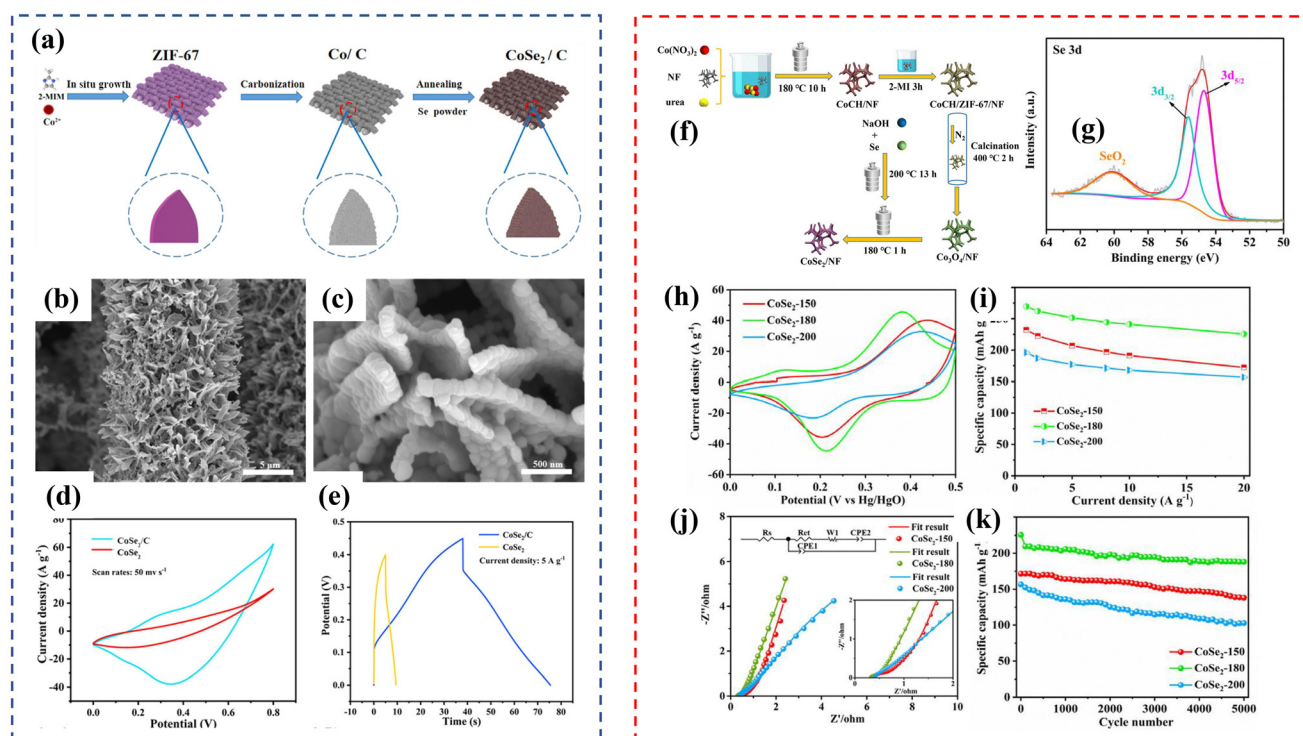


**Fig. 17** (a) Schematic of the CoSe<sub>2</sub>/C lamellar array; (b and c) SEM images of CoSe<sub>2</sub>/C; (d) CV curves at  $50 \text{ mV s}^{-1}$  and (e) GCD curves at  $5 \text{ A g}^{-1}$  of CoSe<sub>2</sub> and CoSe<sub>2</sub>/C. Reprinted with permission from ref. 190, Copyright 2021, Elsevier B.V. (f) Schematic of the CoSe<sub>2</sub> electrode preparation process; (g) high-resolution XPS patterns of Se 3d; (h) CV curves at  $10 \text{ mV s}^{-1}$ , (i) specific capacitance, (j) Nyquist plots and (k) cycling performance of CoSe<sub>2</sub>-T electrode. Reprinted with permission from ref. 196, Copyright 2023, The Royal Society of Chemistry.



formance with the maximum specific energy of 45.6 W h kg<sup>-1</sup> at a specific power of 800.8 W kg<sup>-1</sup> and original capacitance retention rate of 81.5% after 5000 cycles.

## 4.2 Multi-metal selenides

Also, Tan *et al.*<sup>185</sup> successfully assembled nickel cobalt selenide (H-Ni-Co-Se) nanoarrays with a hollow structure from pentagon-like Ni/Co-ZIF on Ni foam by employing a sequential chemical etching and selenylation strategy. The hollow configuration grown on Ni-foam could offer a rich electroactive region, shorten the charge/ion diffusion length and enhance the mass/electrons transfer. Consequently, the as-prepared H-Ni-Co-Se delivered a favorable specific capacitance of 1175 F g<sup>-1</sup> at 1 A g<sup>-1</sup>, fast charge/discharge rate and excellent long-term stability. Similarly, Wang *et al.*<sup>191</sup> reported the preparation of a hollow NiCoSe<sub>2</sub>/C through a step-by-step derivatization method as a high-performance supercapacitor electrode. Hollow nickel-cobalt bimetallic layered hydroxide (NiCo-LDH) derived from ZIF-67 was selenized to NiCoSe<sub>2</sub> *via in situ* selenylation, which was then coated with a layer of carbon *via* the hydrothermal method using glucose as the carbon source. The electrochemical performances of the as-synthesized NiCoSe<sub>2</sub>/C were investigated, and the results indicated that the hollow NiCoSe<sub>2</sub>/C exhibited a considerable specific capacity of 232.6 mA h g<sup>-1</sup> at 1 A g<sup>-1</sup>, good rate capability of 72.6% and high capacity retention of 88.3% after 5000 cycles. Compared with ZIF-67, NiCo-LDH and NiCoSe<sub>2</sub>, the greatly enhanced electrochemical performances of NiCoSe<sub>2</sub>/C can be attributed to the hollow nanostructure of NiCoSe<sub>2</sub>, enhanced electrical conductivity by the introduction of Se and C, and inhibited volume changes during the redox cycling from the protection of the carbon layer. Salehan *et al.*<sup>195</sup> also synthesized a cobalt-nickel selenide nitrogen-doped carbon (H-CoNiSe<sub>2</sub>/NC) hollow polyhedral composite structure and the presence of the NC structure in the proposed composite could simultaneously lead to improved conductivity and reduce the volume effect created during the cycling procedure. The H-CoNiSe<sub>2</sub>/NC electrode provided a high specific capacity (1131 C g<sup>-1</sup> at 1.0 A g<sup>-1</sup>) and outstanding cyclic stability (90.2% retention after 6000 cycles). In addition, the H-CoNiSe<sub>2</sub>/NC//AC hybrid supercapacitor delivered an ultrahigh energy density and power density (81.9 W h kg<sup>-1</sup> at 900 W kg<sup>-1</sup>, respectively) and excellent cyclic stability (92.1% of the initial capacitance after 6000 cycles). Additionally, Zong *et al.*<sup>187</sup> successfully designed and fabricated P-(Ni, Co)Se<sub>2</sub> nanoarrays on activated carbon cloth with PBA nanocubes anchored on nanoflakes-nanowires *via* a facile hydrothermal method, followed precipitate reaction and phosphorization/selenylation treatment (Fig. 18a). The continuous hollow PBA nanocubes and appropriate incorporation of P in (Ni, Co)Se<sub>2</sub> could greatly increase the active surface area and enhance the ion diffusion and charge transfer. The reaction is shown as the following equations:



The resultant P-(Ni, Co)Se<sub>2</sub> NA electrode delivered a high areal capacity of 3.02 C cm<sup>-2</sup> (a specific capacity of 755 C g<sup>-1</sup>) at 2 mA cm<sup>-2</sup> and a good rate capability (2.61 C cm<sup>-2</sup> at 30 mA cm<sup>-2</sup>), as shown in Fig. 18b–e. Furthermore, an all-solid-state hybrid supercapacitor device was also constructed using P-(Ni, Co)Se<sub>2</sub> NAs and ZIF-8-derived carbon as the positive electrode and negative electrode, respectively, which showed a high energy density of 45.0 W h kg<sup>-1</sup> at the power density of 446.3 W kg<sup>-1</sup>. Moreover, Andikaey *et al.*<sup>193</sup> developed trimetallic CoNiSe<sub>2</sub>/Fe-CoNiSe<sub>2</sub> yolk-shell nanoboxes (YSBs) using ZIF-67/NiCoFe Prussian blue analogue (PBA) precursors. Structural engineering of the PBA framework with Co-Fe oxide increased the topological complexity of the nanostructure. The energy storage activity was effectively improved because of the open structure and larger surface area. The presence of trimetallic selenides in CoNiSe<sub>2</sub>/Fe-CoNiSe<sub>2</sub> YSBs improved the electronic structures, and thus the electrochemical performances, and enhanced conductivity of the nanostructure compared with its oxide counterparts. As a result, it exhibited an attractive electrochemical performance when used as an electrode for battery-type supercapacitors. CoNiSe<sub>2</sub>/Fe-CoNiSe<sub>2</sub> yolk-shell nanoboxes showed a high specific capacity of 1091.2 C g<sup>-1</sup> at 1 A g<sup>-1</sup>, good acceleration performance (55% at 20 A g<sup>-1</sup>), and excellent cycle stability (85% recovery after 5000 charge-discharge cycles). Furthermore, the CoNiSe<sub>2</sub>/Fe-CoNiSe<sub>2</sub> YSB//AC hybrid SC demonstrated an energy density above 76.5 W h kg<sup>-1</sup> at a power density of 2378.7 W kg<sup>-1</sup>.

## 4.3 Composite materials

Furthermore, Lv *et al.*<sup>184</sup> reported the preparation of hierarchical “tube-on-fiber” nanostructures composed of carbon nanotubes (CNTs) on carbon nanofibers (CNFs) and impregnated with mixed-metal selenide nanoparticles (Co-Zn-Se@CNTs-CNf) as high-performance supercapacitors. Co-Zn hybrid zeolitic imidazolate framework-67 (Co-Zn ZIF-67) was electrospun with polyacrylonitrile (PAN) to form nanofibers, which were sequentially thermally treated and subjected to selenylation. The “tube-on-fiber” structure was designed to confine the Co-Zn mixed-metal selenide nanoparticles and prevented their agglomeration. Extruded CNTs rooted in carbon nanofibers further improved the electronic conductivity. The mixed-metal selenide allowed more accommodation space and faradaic reactions compared to the single metal selenide. Based on these merits, the hierarchical Co-Zn-Se@CNTs-CNf exhibited a high specific capacity of 1040.1 C g<sup>-1</sup> (1891 F g<sup>-1</sup>) at 1 A g<sup>-1</sup> with an impressive rate performance in supercapacitors. Furthermore, a hybrid supercapacitor was fabricated with Co-Zn-Se@CNTs-CNf as the cathode and porous carbon nanofibers as the anode (denoted as Co-Zn-Se@CNTs-CNf//PCNFs). It delivered a superior energy and power density of 61.4 W h kg<sup>-1</sup> and 754.4 W kg<sup>-1</sup>, respectively, and meanwhile retained an energy density of 31.7 W h kg<sup>-1</sup> with the working power of 15 421.6 W kg<sup>-1</sup>. In addition, the assembled supercapacitor device displayed an excellent capacity retention of 88.6% after 8000 cycles at 5 A g<sup>-1</sup>. Also, Wang *et al.*<sup>189</sup> reported the facile syn-

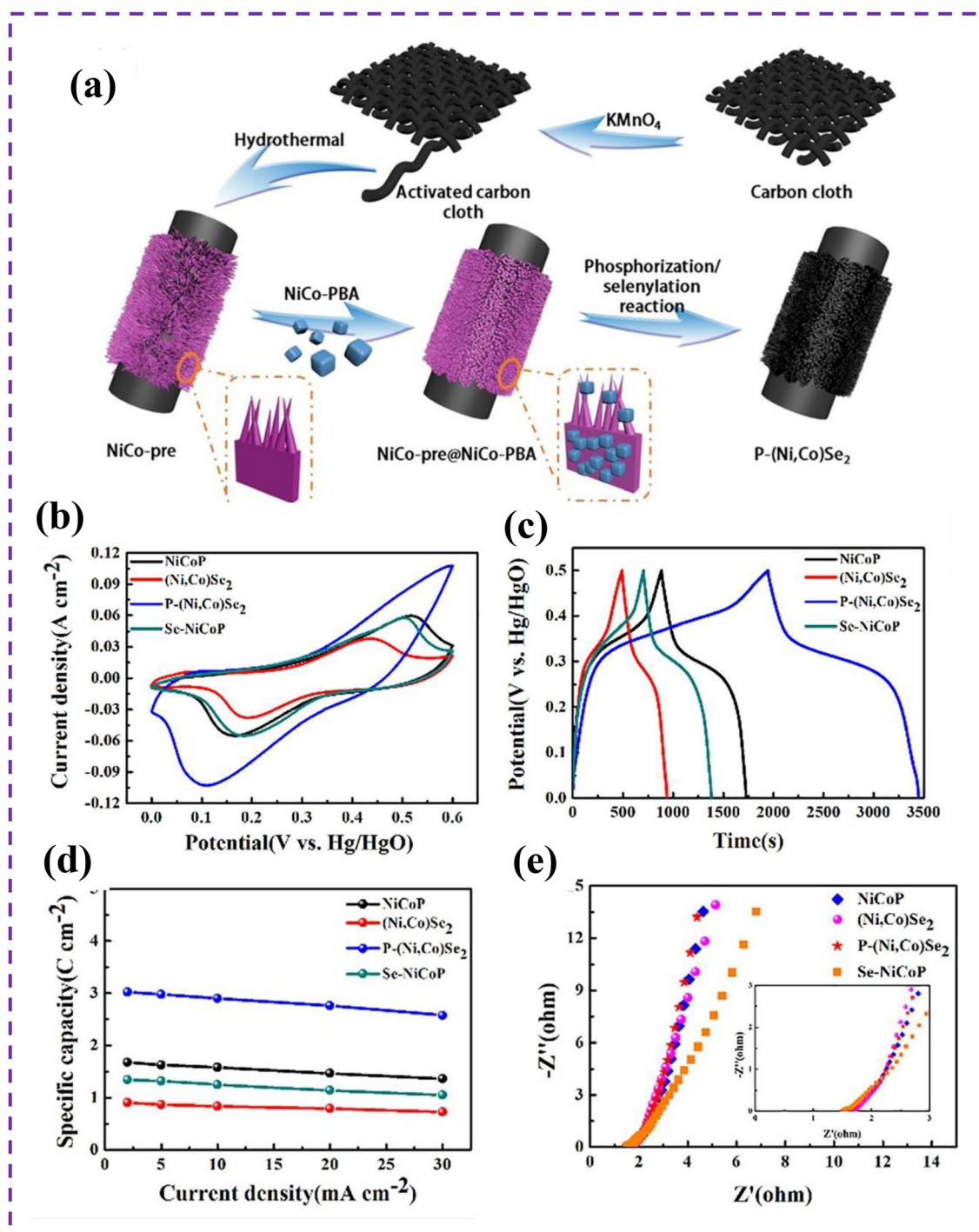


**Fig. 18** (a) Schematic of the procedure for the fabrication of P-(Ni, Co)Se<sub>2</sub> NAs on activated carbon cloth; (b) CV curves at 10 mV s<sup>-1</sup>, (c) GCD curves at 2 mA cm<sup>-2</sup>, (d) specific capacitance and (e) Nyquist plots of NiCoP, (Ni, Co)Se<sub>2</sub>, P-(Ni, Co)Se<sub>2</sub> and Se-NiCoP. Reprinted with permission from ref. 187, Copyright 2019, Elsevier B.V.

thesis of graphene oxide (GO)-supported CoSe<sub>2</sub> (CoSe<sub>2</sub>/GO) derived from ZIF-67 *via* the hydrothermal method. CoSe<sub>2</sub>/GO exhibited a considerable specific capacity (108.31 mA h g<sup>-1</sup> at 1 A g<sup>-1</sup>) and high cyclic stability (capacity retention of 91.2% after 5000 cycles). Compared with GO and CoSe<sub>2</sub> alone, the greatly enhanced electrochemical performances of CoSe<sub>2</sub>/GO

can be attributed to the synergistic effect of GO and CoSe<sub>2</sub>. Additionally, Yang *et al.*<sup>194</sup> synthesized ZIF-67-derived CoSe<sub>2</sub>/Ni<sub>3</sub>Se<sub>4</sub> nanosheets anchored vertically on an MXene substrate, which enhanced the overall conductivity. Furthermore, the close combination between the CoSe<sub>2</sub>/Ni<sub>3</sub>Se<sub>4</sub> nanosheets and MXene nanosheets promoted a faster charge transfer rate

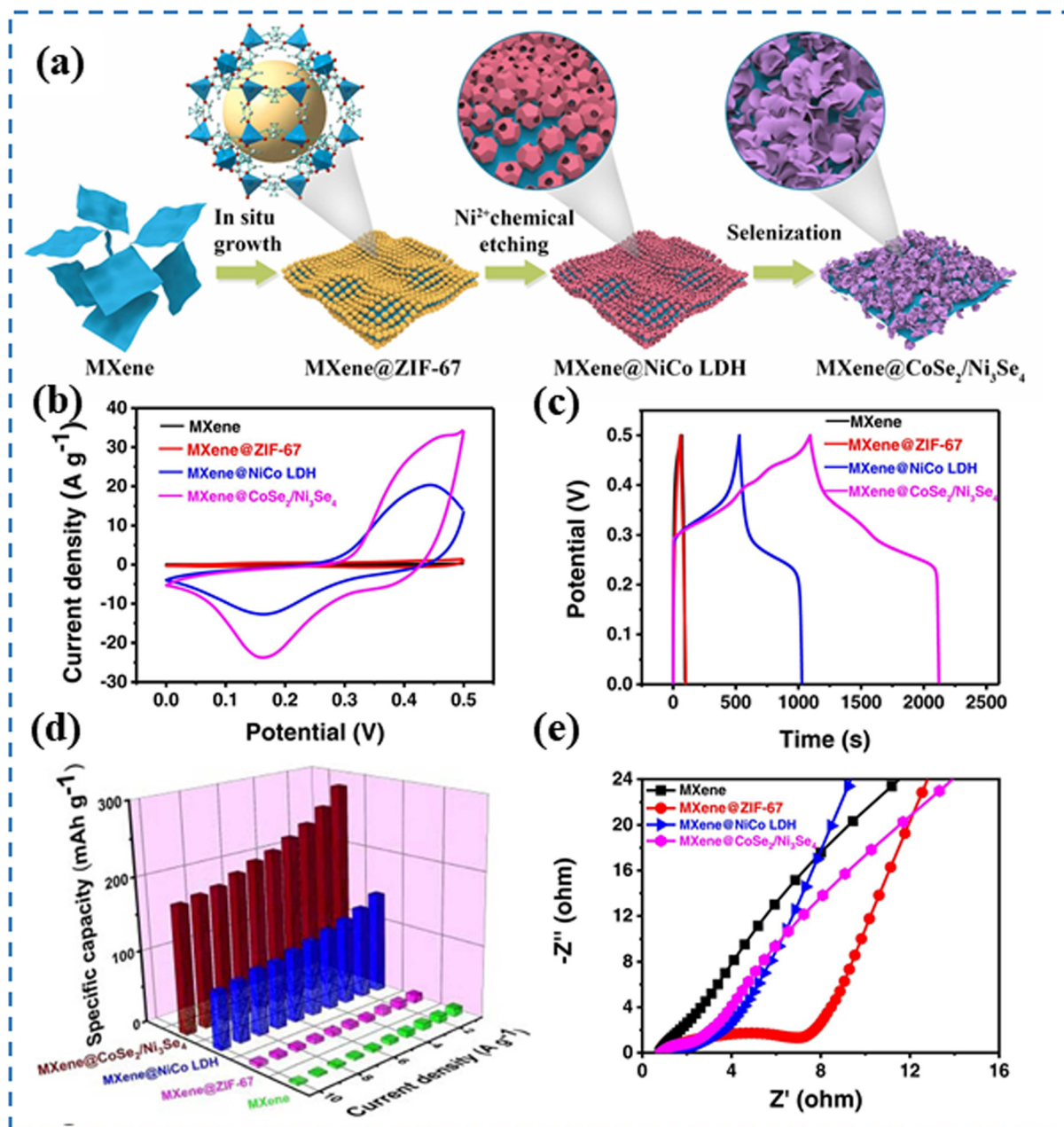


**Fig. 19** (a) Schematic of the synthesis of the hierarchical 2D MXene@CoSe<sub>2</sub>/Ni<sub>3</sub>Se<sub>4</sub> nanosheets and (b) CV curves at 5 mV s<sup>-1</sup>, (c) GCD curves at 1 A g<sup>-1</sup>, (d) specific capacitance and (e) Nyquist plots of MXene, MXene@ZIF-67, MXene@NiCo-LDH and MXene@CoSe<sub>2</sub>/Ni<sub>3</sub>Se<sub>4</sub>. Reprinted with permission from ref. 194, Copyright 2022, Elsevier B.V.

and improved the durability of the structure (Fig. 19a). Consequently, as an electrode material for supercapacitors, the honeycomb-like MXene@CoSe<sub>2</sub>/Ni<sub>3</sub>Se<sub>4</sub> achieved a high specific capacitance (283 mA h g<sup>-1</sup> at 1 A g<sup>-1</sup>, as shown in Fig. 19b–e) and an outstanding capacitance retention rate with 80% after 5000 cycles. Moreover, Shi's group reported the synthesis of M–(Ni, Co)–Se@CNFs/CC<sup>199</sup> and Ni<sub>x</sub>Co<sub>1–x</sub>Se<sub>2</sub>/CNFs/CoO@CC<sup>188</sup> derived from ZIF-L for hybrid supercapacitors, respectively. M–(Ni, Co)–Se@CNFs/CC exhibited a specific capacitance of 378.9 mA h g<sup>-1</sup> at 1 A g<sup>-1</sup>, while that

of Ni<sub>x</sub>Co<sub>1–x</sub>Se<sub>2</sub>/CNFs/CoO@CC was 207.8 mA h g<sup>-1</sup>, and both displayed a superior performance and stability.

Meanwhile, Zhang *et al.*<sup>200</sup> synthesized a wire-sheet-particle hierarchical hetero-structured CoSe<sub>2</sub>@NiMn-layered double hydroxide (NiMn-LDH)@Cu<sub>1.8</sub>Se/Copper foam (CF) electrode *via* a phase pseudomorphic transformation process achieved by the selective selenization of Cu and Co elements (Fig. 20a). Benefiting from the stable support structure of CuBr<sub>2</sub>, the large specific surface area of NiMn-LDH, and the excellent conductivity of CoSe<sub>2</sub>, the prepared binder-free electrode showed



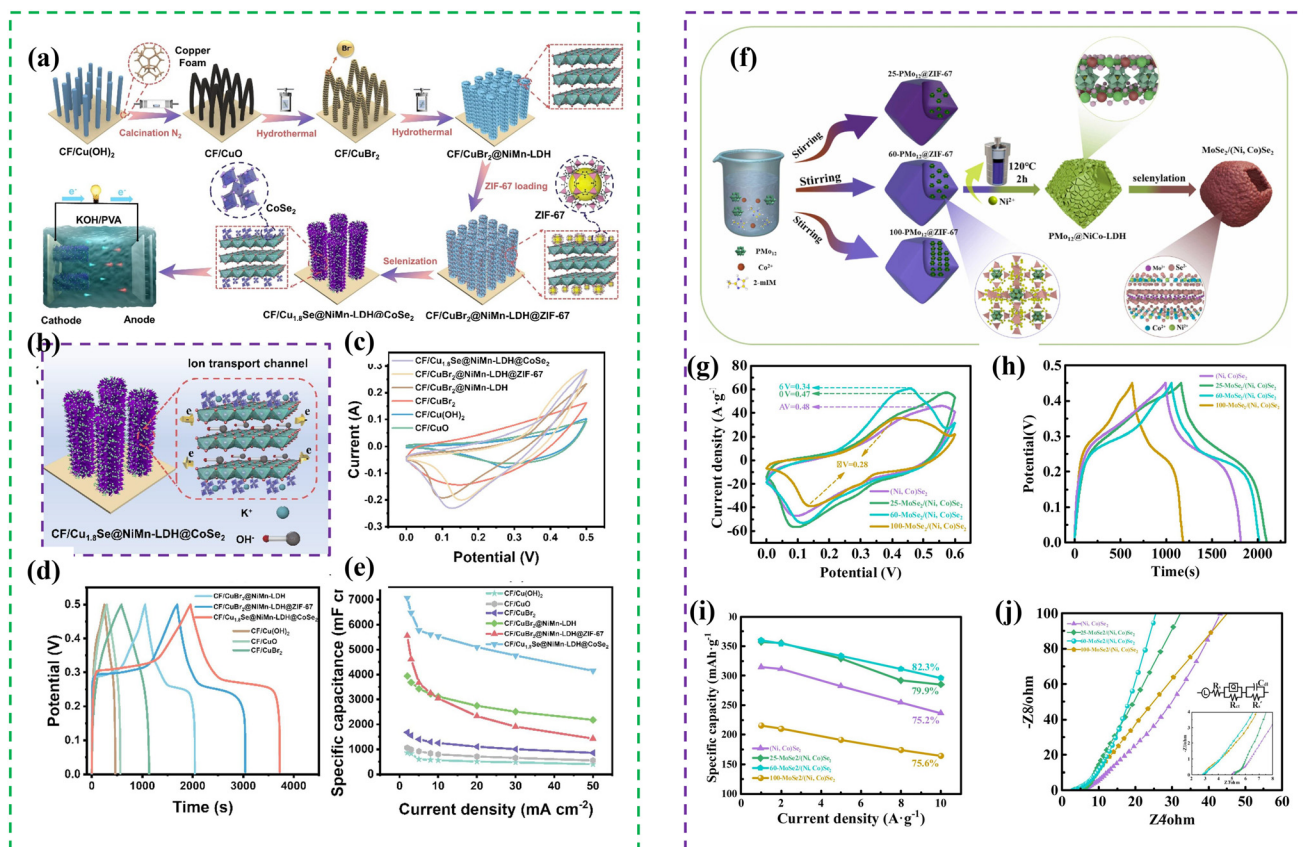


**Fig. 20** (a) Schematic depiction of the stepwise formation process of  $\text{CoSe}_2@NiMn-LDH@Cu_{1.8}Se/CF$  nanosheet arrays derived from ZIF-67-covered  $\text{CuBr}_2$  nanorod arrays via selective phase pseudomorphic transformation; (b) schematic of capacitance process of  $\text{CoSe}_2@NiMn-LDH@Cu_{1.8}Se/CF$ ; and (c) CV curves, (d) GCD curves and (e) specific capacitance of  $\text{CoSe}_2@NiMn-LDH@Cu_{1.8}Se/CF$ , ZIF-67@ $NiMn-LDH@CuBr_2/CF$ ,  $NiMn-LDH@CuBr_2/CF$ ,  $CuBr_2/CF$ ,  $Cu(OH)_2/CF$  and  $CuO/CF$ . Reprinted with permission from ref. 200, Copyright 2023, Elsevier Inc. (f) Schematic illustration of procedure for the preparation of  $\text{MoSe}_2/(Ni, Co)Se_2$  hollow nanomaterials; and (g) CV curves at  $15 \text{ mV s}^{-1}$ , (h) GCD curves at  $1 \text{ A g}^{-1}$ , (i) specific capacitance and (j) Nyquist plots of  $(Ni, Co)Se_2$ ,  $25\text{-MoSe}_2/(Ni, Co)Se_2$ ,  $60\text{-MoSe}_2/(Ni, Co)Se_2$  and  $100\text{-MoSe}_2/(Ni, Co)Se_2$ . Reprinted with permission from ref. 201, Copyright 2024, Elsevier B.V.

excellent electrochemical properties. The  $\text{CoSe}_2@NiMn-LDH@Cu_{1.8}Se$  hybrid electrode exhibited a superior specific areal capacitance of  $7064 \text{ mF cm}^{-2}$  at  $2 \text{ mA cm}^{-2}$  and a stable cyclic performance with 80.11% capacitance retention after 10 000 cycles (Fig. 20b–e). Furthermore, the assembled  $\text{CoSe}_2@NiMn-LDH@Cu_{1.8}Se/CF//AC$  (activated carbon) asymmetric supercapacitor (ASC) achieved an energy density of  $36.6 \text{ W h kg}^{-1}$  at the power density of  $760.6 \text{ W kg}^{-1}$  and retained 87.35% of its initial capacitance after 5000 cycles. Also, Guo *et al.*<sup>201</sup> synthesized  $\text{MoSe}_2/(Ni, Co)Se_2$  hollow structures derived from  $\text{PMo}_{12}/\text{ZIF-67}$  precursor by an  $\text{Ni}^{2+}$  etching and selenization process (Fig. 20f). In the three-electrode test, as shown in Fig. 20g–j, the developed  $60\text{-MoSe}_2/(Ni, Co)Se_2$  electrode material exhibited an excellent specific capacity of  $359.9 \text{ mA h g}^{-1}$  at a current density of  $1 \text{ A g}^{-1}$ , and a capacitance retention rate of 83.7% after 10 000 cycles. In addition, the asymmetric supercapacitor (ASC) assembled with  $60\text{-MoSe}_2/(Ni, Co)Se_2$  as the positive electrode and activated carbon as the negative electrode exhibited an excellent energy density of  $40.3 \text{ W h kg}^{-1}$  at a power density of  $800.9 \text{ W kg}^{-1}$ .

## 5. ZIF-67-derived transition metal tellurides

Similar to sulfides and selenides, tellurides are a newly explored class of chalcogenides in supercapacitors, which exhibit improved metallic properties, larger lattice parameters and higher degree of covalency in anion–metal bonding than sulfides and selenides.<sup>203</sup> Therefore, ZIF-67-derived transition metal tellurides are also new materials worth exploring.

Kshetri *et al.*<sup>204</sup> reported the fabrication of a ZIF-67-derived  $\text{CoTe}$ –carbon porous-structured composite on nickel foam ( $\text{CoTe}@C\text{-NiF}$ ) by high-temperature treatment (Fig. 21a). As shown in Fig. 21b–e, in the negative potential regions, the  $\text{CoTe}@C\text{-NiF}$  hybrid electrode exhibited a maximum areal capacitance of  $307.5 \text{ mF cm}^{-2}$  at a current density of  $1 \text{ mA cm}^{-2}$  and retained  $162.0 \text{ mF cm}^{-2}$  at a high current density of  $20 \text{ mA cm}^{-2}$ , resulting in a rate capability of 52.03%. However, in the positive potential region, the same electrode showed

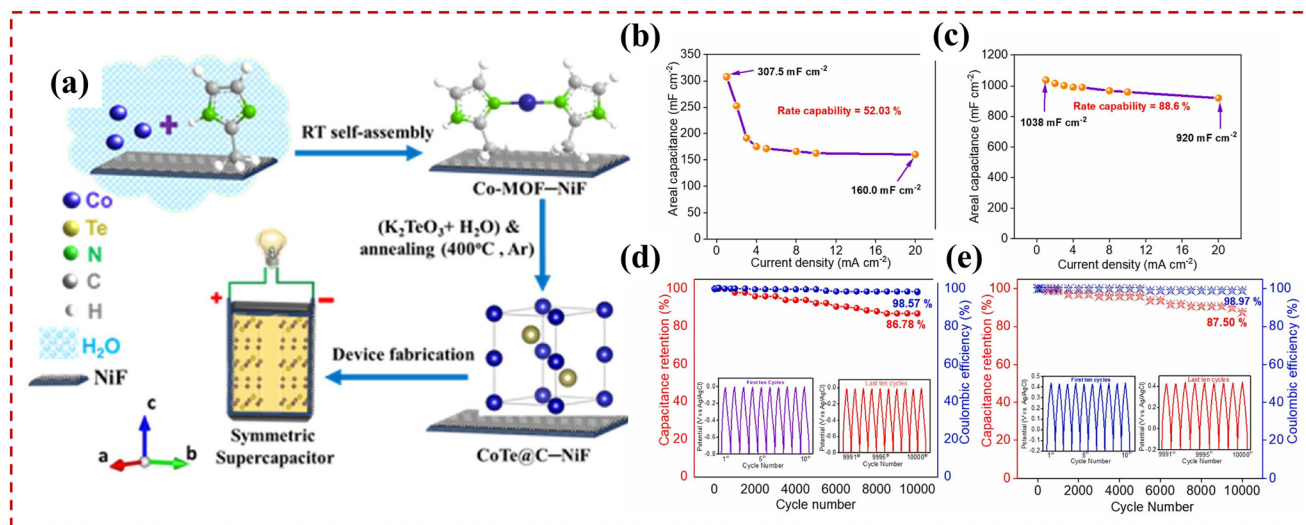


Fig. 21 (a) Schematic for the synthesis of CoTe@C-NiF hybrid electrode; and (b and c) specific capacitance and (d and e) cycling stability of CoTe@C-NiF in the negative and positive potential window, respectively. Reprinted with permission from ref. 204, Copyright 2021, Elsevier Ltd.

areal capacitances of 1038 mF cm<sup>-2</sup> and 920 mF cm<sup>-2</sup>, respectively, at the same current densities, resulting in a rate capability of 88.63%. In addition, CoTe@C-NiF showed long-term electrochemical stability during the charge-discharge process in both the negative and positive potential window. In the negative potential window, it showed 86.78% and 98.57% retention of areal capacitance and coulombic efficiency, respectively. Similarly, in the positive window, 87.50% and 98.97% retention of areal capacitance and coulombic efficiency was observed after 10 000 charge-discharge cycles, respectively.

## 6. Summary and perspectives

### 6.1 Summary

Supercapacitors (SCs) are generally regarded as promising electrochemical devices in the field of energy storage due to their advantages of fast charge-discharge rate and long cyclic term. However, the low energy density of SCs limits their further application. In this case, electrode materials, as one of the components of SCs, play an important role in the electrochemical performance of energy storage devices. Thus, to improve the energy density of SC devices, it is essential to look for or synthesize new electrode materials. Recently, ZIF-67 has attracted considerable attention as an electrode material for SC application because of its controllable pore rate, constant cavity and large specific area. Also, pristine ZIF-67 and ZIF-67 derivatives such as porous carbon, metal-doped carbon, hydroxides (Table S3†), phosphides (Table S4†) and chalcogenides (including oxides, sulfides, selenides and tellurides) have shown exemplary performances in supercapacitors but still have some challenges that need to be overcome. Therefore, in this review, we discussed ZIF-67-derived chalcogenides as electrode materials for SCs

including their preparation strategies, micro structure and electrochemical properties. Generally, as a typical pseudocapacitor materials, ZIF-67-derived chalcogenides have a larger specific capacitance and higher energy density than pristine ZIF-67 and ZIF-67-derived carbon materials. However, that still have some disadvantages such as the slightly lower capacity for oxides with high structural stability and volume expansion and structural destruction during long-term cycling for sulfides, selenides and tellurides. Therefore, researchers have developed many strategies to solve these questions. For instance, from single metal compounds to multi-metal compounds, the specific capacitance of chalcogenides can be improved greatly due to the changes in their chemical properties. Also, doping metal ions can provide more active sites for electrochemical reactions. Additionally, combining chalcogenides with other materials such as carbon materials (carbon nanotubes and graphene), conductive polymers (PPy, PANI, and PEDOT), 2D MXenes and other transition metal compounds is also an effective way to improve their conductivity and structural stability. Many of the studies mentioned herein have proven the feasibility of these methods.

### 6.2 Perspectives

ZIF-67 is desirable for a wide range of applications owing to its tailorable surface area, porosity, precise pore size and composition control as key considerations. However, the weak inherent conductivity and structural instability of pristine ZIF-67 restricts its usage in electrochemical applications. ZIF-67-derived chalcogenides have emerged as viable materials for supercapacitor applications due to the strong control of their morphology, functionalization, doping of heteroatoms, enhanced surface area and structural modification. However, there is still many aspects of ZIF-67-derived chalcogenides for SC application worth researching.

- ZIF-67-derived tellurides exhibit excellent electrochemical properties because of their improved metallic properties, large lattice parameters and high degree of covalency in anion-metal bonding. However, there are still few studies about ZIF-67-derived transition metal tellurides. Therefore, more work on tellurides needs further research in the future.

- There are still certain shortcomings in the current common preparation methods, as follows: (1) the coprecipitation method is the simultaneous precipitation of soluble and micro-components from the same solution by adsorption, encapsulation or mechanical trapping to form mixed crystals. However, ZIF-67 prepared by this method has poor uniformity unless premium solvents and surfactant are used. (2) The hydrothermal/solvothermal method is a synthesis process in which chemical reagents and solvents are heated inside a high-pressure steel vessel, but has lower yields. (3) Annealing/carbonization is a high-temperature procedure that requires a strict atmosphere and sometimes destroys the structure of ZIF-67. Therefore, it is imperative to improve existing methods and adopt new methods. Surfactants are essential for the coprecipitation method; optimization of the parameters for the hydrothermal/solvothermal and annealing/carbonization methods, such as time, temperature and atmosphere, should be evaluated; and microwave/ultrasonic wave-assisted techniques have become increasingly popular because they cause atoms and molecules to oscillate, effectively initiating chemical processes. Moreover, the electrochemical method is also a good synthesis process due to its quicker synthesis conditions and greater control. Hence, there is a need to evaluate the synthesis of ZIF-67 and its derivatives.

- ZIF-67-derived chalcogenides have a complex composition, including local crystal/amorphous inorganic compounds and organic frameworks/carbon, which increases the difficulty of characterizing the microstructure of these materials. Thus, to further analyze the evolution of substances and structures in material synthesis and electrochemical reactions, organic/inorganic characterization methods should be combined for comprehensive analysis.

- Similarly, due to the complex composition of ZIF-67-derived chalcogenides, they are different from pure chalcogenides in the mechanism of energy storage/conversion systems. Therefore, *in situ* measurements, such as Raman spectroscopy, X-ray diffraction, X-ray absorption spectroscopy, ambient-pressure XPS and electrochemical mass spectrometry, may be useful. Meanwhile, in the process of theoretical calculation, compared to pure chalcogenides, the construction of the model must also consider the existence of frameworks, which may increase the complexity of the work.

- Flexible and wearable micro-supercapacitors and micro-batteries based on ZIF-67-derived chalcogenides with controlled properties together with safe, reliable and intelligent electronic properties also need to be further investigated.

Overall, we believe that the further design and synthesis of ZIF-67-derived chalcogenides need to be studied for meeting the requirements of supercapacitor application.

## Author contributions

Lidong Jiao: investigation, formal analysis, writing-original draft, and visualization. Mingshu Zhao: conceptualization, methodology, supervision, funding acquisition, and writing-review & editing. Qingyang Zheng: investigation. Qingyi Ren: investigation and validation. Zhou Su: validation. Min Li: investigation. Feng Li: formal analysis.

## Data availability

No primary research results, software or code has been included and no new data were generated or analysed as part of this review.

## Conflicts of interest

There are no conflicts to declare.

## Acknowledgements

The authors acknowledge Hunan Province Natural Science Fund-Regional Joint Fund (2024JJ7029) and Horizontal Project of Chinese Academy of Science Institute of Metals-Xi'an Jiaotong University (20241068). The authors also thank Mr Jun Li at Changde Collaborative Innovation Research Institute Co., Ltd for the collaborative support.

## References

- 1 T. M. I. Mahlia, T. J. Saktisandan, A. Jannifar, M. H. Hasan and H. S. C. Matseelar, *Renewable Sustainable Energy Rev.*, 2014, **33**, 532–545.
- 2 Lichchhavi, A. Kanwade and P. M. Shirage, *J. Energy Storage*, 2022, **55**, 105692.
- 3 S. Y. Liu, J. Yang, P. Chen, M. Wang, S. J. He, L. Wang and J. S. Qiu, *Electrochem. Energy Rev.*, 2024, **7**, 25.
- 4 Z. Yu, L. Tetard, L. Zhai and J. Thomas, *Energy Environ. Sci.*, 2015, **8**, 702–730.
- 5 N. Choudhary, C. Li, J. Moore, N. Nagaiah, L. Zhai, Y. Jung and J. Thomas, *Adv. Mater.*, 2017, **29**, 1605336.
- 6 Z. Wu, L. Li, J.-M. Yan and X.-B. Zhang, *Adv. Sci.*, 2017, **4**, 1600382.
- 7 Poonam, K. Sharma, A. Arora and S. K. Tripathi, *J. Energy Storage*, 2019, **21**, 801–825.
- 8 P. Forouzandeh, V. Kumaravel and S. C. Pillai, *Catalysts*, 2020, **10**, 969.
- 9 Reenu, Sonia, L. Phor, A. Kumar and S. Chahal, *J. Energy Storage*, 2024, **84**, 110698.
- 10 A. Afir, S. M. H. Rahman, A. T. Azad, J. Zaini, M. A. Islan and A. K. Azad, *J. Energy Storage*, 2019, **25**, 100852.
- 11 P. Lamba, P. Singh, P. Singh, P. Singh, Bharti, A. Kumar, M. Gupta and Y. Kumar, *J. Energy Storage*, 2022, **48**, 103871.



- 12 W. J. Fan, F. X. Wang, X. S. Xiong, B. Y. Song, T. Wang, X. B. Cheng, Z. Zhu, J. R. He, Y. K. Liu and Y. P. Wu, *NPG Asia Mater.*, 2024, **16**, 18.
- 13 K. Chhetri, A. Adhikari, J. Kunwar, D. Acharya, R. M. Bhattarai, Y. S. Mok, A. Adhikari, A. P. Yadav and H. Y. Kim, *Int. J. Energy Res.*, 2023, **2023**, 8885207.
- 14 W. Zuo, R. Li, C. Zhou, Y. Li, J. Xia and J. Liu, *Adv. Sci.*, 2017, **4**, 1600539.
- 15 Y. Jiang and J. Liu, *Energy Environ. Mater.*, 2019, **2**, 30–37.
- 16 A. Muzaffar, M. B. Ahamed, K. Deshmukh and J. Thirumalai, *Renewable Sustainable Energy Rev.*, 2019, **101**, 123–145.
- 17 Q. Wu, T. He, Y. Zhang, J. Zhang, Z. Wang, Y. Liu, L. Zhao, Y. Wu and F. Ran, *J. Mater. Chem. A*, 2021, **9**, 24094–24147.
- 18 M. Z. Iqbal and U. Aziz, *J. Energy Storage*, 2022, **46**, 103823.
- 19 V. Augustyn, P. Simon and B. Dunn, *Energy Environ. Sci.*, 2014, **7**, 1597–1614.
- 20 J. Yan, Q. Wang, T. Wei and Z. Fan, *Adv. Energy Mater.*, 2014, **4**, 1300816.
- 21 Y. Zeng, M. Yu, Y. Meng, P. Fang, X. Lu and Y. Tong, *Adv. Energy Mater.*, 2016, **6**, 1601053.
- 22 W. Raza, F. Ali, N. Raza, Y. Luo, K.-H. Kim, J. Yang, S. Kumar, A. Mehmood and E. E. Kwon, *Nano Energy*, 2018, **52**, 441–473.
- 23 D. P. Chatterjee and A. K. Nandi, *J. Mater. Chem. A*, 2021, **9**, 15880–15918.
- 24 S. Zheng, X. Li, B. Yan, Q. Hu, Y. Xu, X. Xiao, H. Xue and H. Pang, *Adv. Energy Mater.*, 2017, **7**, 1602733.
- 25 Y. Li, Y. Xu, W. Yang, W. Shen, H. Xue and H. Pang, *Small*, 2018, **14**, 1704435.
- 26 B. Xu, H. Zhang, H. Mei and D. Sun, *Coord. Chem. Rev.*, 2020, **420**, 213438.
- 27 K.-B. Wang, Q. Xun and Q. Zhang, *EnergyChem*, 2020, **2**, 100025.
- 28 L. Xu, Y. K. Xi, W. B. Li, Z. L. Hua, J. H. Peng, J. H. Hu, J. J. Zhou, P. L. Zhang, J. J. Wang, W. W. Wang, H. L. Ding, W. Q. Wang, W. X. Ji, Y. Yang, X. C. Xu, L. Y. Chen and X. F. Li, *Nano Energy*, 2022, **91**, 106630.
- 29 R. R. Salunkhe, Y. V. Kaneti, J. Kim, J. H. Kim and Y. Yamauchi, *Acc. Chem. Res.*, 2016, **49**, 2796–2806.
- 30 J. A. Feng, J. Y. Li, H. W. Zhang, W. D. Liu, Z. H. Lin, T. Y. Wang, B. Sun, X. X. Zhao, F. Y. Wang and J. J. Song, *Energy Mater.*, 2023, **3**, 300001.
- 31 R. R. Salunkhe, Y. V. Kaneti and Y. Yamauchi, *ACS Nano*, 2017, **11**, 5293–5308.
- 32 Q. Wang, F. Gao, B. Xu, F. Cai, F. Zhan, F. Gao and Q. Wang, *Chem. Eng. J.*, 2017, **327**, 387–396.
- 33 S. Karingula, S. Kummari, Y. G. Kotagiri, T. Bhokya and K. V. Gobi, *Small*, 2024, **20**, 2400812.
- 34 C. Lamiel, I. Hussain, H. Rabiee, O. R. Ogunsakin and K. Zhang, *Coord. Chem. Rev.*, 2023, **480**, 215030.
- 35 Y. Peng, J. Xu, J. Xu, J. Ma, Y. Bai, S. Cao, S. Zhang and H. Pang, *Adv. Colloid Interface Sci.*, 2022, **307**, 102732.
- 36 A. Zhang, Q. Zhang, H. Fu, H. Zong and H. Guo, *Small*, 2023, **19**, 2303911.
- 37 Q. Cheng, C. Yang, K. Tao and L. Han, *Electrochim. Acta*, 2020, **341**, 136042.
- 38 K. Qu, Z. Sun, C. Shi, W. Wang, L. Xiao, J. Tian, Z. Huang and Z. Guo, *Adv. Compos. Hybrid Mater.*, 2021, **4**, 670–683.
- 39 J. X. Zhao, Y. Zhang, H. Y. Lu, Y. F. Wang, X. D. Liu, H. M. K. Sari, J. H. Peng, S. F. Chen, X. F. Li, Y. J. Zhang, X. L. Sun and B. G. Xu, *Nano Lett.*, 2022, **22**, 1198–1206.
- 40 L. Jiao, M. Zhao, Z. Su, M. Shi, M. Li and F. Li, *Electrochim. Acta*, 2024, **479**, 143888.
- 41 J. Qin, Z. Yang, F. Xing, L. Zhang, H. Zhang and Z. Wu, *Electrochem. Energy Rev.*, 2023, **6**, 9.
- 42 A. M. Mohamed, M. Ramadan and N. K. Allam, *J. Energy Storage*, 2021, **34**, 102195.
- 43 D. G. Wang, Z. B. Liang, S. Gao, C. Qu and R. G. Zou, *Coord. Chem. Rev.*, 2020, **404**, 213093.
- 44 K. B. Wang, Q. Xun and Q. C. Zhang, *EnergyChem*, 2020, **2**, 100025.
- 45 A. Phan, C. J. Doonan, F. J. Uribe-Romo, C. B. Knobler, M. O'Keeffe and O. M. Yaghi, *Acc. Chem. Res.*, 2010, **43**, 58–67.
- 46 Y. Xie, Z. Yang, M. Cao, Y. Feng and J. Yao, *Electrochim. Acta*, 2024, **488**, 144222.
- 47 N. L. Torad, R. R. Salunkhe, Y. Li, H. Hamoudi, M. Imura, Y. Sakka, C.-C. Hu and Y. Yamauchi, *Chem. – Eur. J.*, 2014, **20**, 7895–7900.
- 48 S. A. Delbari, L. S. Ghadimi, R. Hadi, S. Farhoudian, M. Nedaei, A. Babapoor, A. S. Namini, L. Quyet Van, M. Shokouhimehr, M. S. Asl and M. Mohammadi, *J. Alloys Compd.*, 2021, **857**, 158281.
- 49 R. R. Salunkhe, J. Tang, Y. Kamachi, T. Nakato, J. H. Kim and Y. Yamauchi, *ACS Nano*, 2015, **9**, 6288–6296.
- 50 Y.-Z. Zhang, Y. Wang, Y.-L. Xie, T. Cheng, W.-Y. Lai, H. Pang and W. Huang, *Nanoscale*, 2014, **6**, 14354–14359.
- 51 D. Yu, L. Ge, B. Wu, L. Wu, H. Wang and T. Xu, *J. Mater. Chem. A*, 2015, **3**, 16688–16694.
- 52 X. Deng, J. Li, S. Zhu, F. He, C. He, E. Liu, C. Shi, Q. Li and N. Zhao, *J. Alloys Compd.*, 2017, **693**, 16–24.
- 53 B. Wang, W. Tan, R. Fu, H. Mao, Y. Kong, Y. Qin and Y. Tao, *Synth. Met.*, 2017, **233**, 101–110.
- 54 C. Wei, K. Liu, J. Tao, X. Kang, H. Hou, C. Cheng and D. Zhang, *Chem. – Asian J.*, 2018, **13**, 111–117.
- 55 G. Wei, Z. Zhou, X. Zhao, W. Zhang and C. An, *ACS Appl. Mater. Interfaces*, 2018, **10**, 23721–23730.
- 56 B. Xue, K. Li, S. Gu and J. Lu, *J. Colloid Interface Sci.*, 2018, **530**, 233–242.
- 57 J.-J. Zhou, X. Han, K. Tao, Q. Li, Y.-L. Li, C. Chen and L. Han, *Chem. Eng. J.*, 2018, **354**, 875–884.
- 58 S. Guo, X. Xu, J. Liu, Q. Zhang and H. Wang, *J. Electrochem. Soc.*, 2019, **166**, A960–A967.
- 59 M. Zhu, Q. Chen, J. Kan, J. Tang, W. Wei, J. Lin and S. Li, *Energy Technol.*, 2019, **7**, 1800963.
- 60 G. Lin, Y. Jiang, C. He, Z. Huang, X. Zhang and Y. Yang, *Dalton Trans.*, 2019, **48**, 5773–5778.
- 61 G. Lee and J. Jang, *J. Power Sources*, 2019, **423**, 115–124.
- 62 X. Han, S. Liu, L. Shi, S. Li, Y. Li, Y. Wang, W. Chen, X. Zhao and Y. Zhao, *Ceram. Int.*, 2019, **45**, 14634–14641.

- 63 F. Wei, W. Liu, X. Zhang, X. Liu, Y. Sui and J. Qi, *Mater. Lett.*, 2019, **255**, 126534.
- 64 F. Saleki, A. Mohammadi, S. E. Moosavifard, A. Hafizi and M. R. Rahimpour, *J. Colloid Interface Sci.*, 2019, **556**, 83–91.
- 65 X. Dai, Y. Dai, J. Lu, L. Pu, W. Wang, J. Jin, F. Ma and N. Tie, *Ionics*, 2019, **26**, 2501–2511.
- 66 Y. Ding, Y. Peng, S. Chen, Z. Li, X. Zhang, P. Falaras and L. Hu, *Appl. Surf. Sci.*, 2019, **495**, 163502.
- 67 J. Xu, C. Xu, Y. Zhao, J. Wu and J. Hu, *Front. Chem.*, 2019, **7**, 831.
- 68 M. Wang, J. Zhang, X. Yi, B. Liu, X. Zhao and X. Liu, *Beilstein J. Nanotechnol.*, 2020, **11**, 240–251.
- 69 D. Chu, D. Guo, B. Xiao, L. Tan, H. Ma, H. Pang, X. Wang and Y. Jiang, *Chem. – Asian J.*, 2020, **15**, 1750–1755.
- 70 K. Le, M. Gao, D. Xu, Z. Wang, G. Wang, G. Lu, W. Liu, F. Wang and J. Liu, *Inorg. Chem. Front.*, 2020, **7**, 3646–3656.
- 71 X. Zha, Z. Wu, Z. Cheng, W. Yang, J. Li, Y. Chen, L. He, E. Zhou and Y. Yang, *Energy*, 2021, **220**, 119696.
- 72 L. Cheng, Q. Zhang, M. Xu, Q. Zhai and C. Zhang, *J. Colloid Interface Sci.*, 2021, **583**, 299–309.
- 73 A. Rashti, X. Lu, A. Dobson, E. Hassani, F. Feyzbar-Khalkhali-Nejad, K. He and T.-S. Oh, *ACS Appl. Energy Mater.*, 2021, **4**, 1537–1547.
- 74 W. Hong, Y. Li, Y. Wu, G. Li and L. Jia, *Mater. Chem. Front.*, 2021, **5**, 1438–1447.
- 75 J. Mao, M. Ge, I. W. P. Chen, Y. H. Ng, T. Zhu, H. Liu, J. Huang, W. Cai and Y. Lai, *Mater. Chem. Front.*, 2021, **5**, 2742–2748.
- 76 L. Xiao, H. Qi, K. Qu, C. Shi, Y. Cheng, Z. Sun, B. Yuan, Z. Huang, D. Pan and Z. Guo, *Adv. Compos. Hybrid Mater.*, 2021, **4**, 306–316.
- 77 T. Shu, H. Wang, Q. Li, Z. Feng, F. Wei, K. X. Yao, Z. Sun, J. Qi and Y. Sui, *Chem. Eng. J.*, 2021, **419**, 129631.
- 78 L. Zhu, C. Hao, S. Zhou, X. Wang, T. Zhou and Y. Guo, *J. Materiomics*, 2021, **7**, 708–720.
- 79 L. Wang, X. Li, S. Xiong, H. Lin, Y. Xu, Y. Jiao and J. Chen, *J. Colloid Interface Sci.*, 2021, **600**, 58–71.
- 80 R. K. Devi, G. Muthusankar, S.-M. Chen and G. Gopalakrishnan, *Microchim. Acta*, 2021, **188**, 196.
- 81 Y. Li, H. Xie, J. Li, Y. Yamauchi and J. Henzie, *ACS Appl. Mater. Interfaces*, 2021, **13**, 41649–41656.
- 82 Y.-F. Ren, Z.-L. He, H.-Z. Zhao and T. Zhu, *Rare Met.*, 2022, **41**, 830–835.
- 83 H. Zhang, B. Yan, C. Zhou, J. Wang, H. Duan, D. Zhang and H. Zhao, *Energy Fuels*, 2021, **35**, 16925–16932.
- 84 S. A. Al khey and H. N. Abdelhamid, *J. Energy Storage*, 2022, **55**, 105449.
- 85 L. Xie, M. Li, P. Zhu, X. Xiao, Z. Jia, Z. Wei and J. Jiang, *J. Alloys Compd.*, 2022, **898**, 162861.
- 86 A. Mateen, M. S. Javed, S. Khan, A. Saleem, M. K. Majeed, A. J. Khan, M. F. Tahir, M. A. Ahmad, M. A. Assiri and K.-Q. Peng, *J. Energy Storage*, 2022, **49**, 104150.
- 87 C. Li, D. Ma and Q. Zhu, *Nanomaterials*, 2022, **12**, 848.
- 88 Z. Duan, X.-R. Shi, C. Sun, W. Lin, S. Huang, X. Zhang, M. Huang, Z. Yang and S. Xu, *Electrochim. Acta*, 2022, **412**, 140139.
- 89 A. G. El-Deen, M. K. Abdel-Sattar and N. K. Allam, *Appl. Surf. Sci.*, 2022, **587**, 152548.
- 90 H. Gong, S. Bie, J. Zhang, X. Ke, X. Wang, J. Liang, N. Wu, Q. Zhang, C. Luo and Y. Jia, *Nanomaterials*, 2022, **12**, 1571.
- 91 K. Venkatesh, C. Karuppiah, R. Palani, G. Periyasamy, S. K. Ramaraj and C.-C. Yang, *Mater. Lett.*, 2022, **323**, 132609.
- 92 L. Chen, J. Wan, X. Feng, H. Shi and P. Liu, *J. Alloys Compd.*, 2022, **918**, 165769.
- 93 S. K. Babu, B. Gunasekaran, M. Sridharan and T. Vijayakumar, *RSC Adv.*, 2022, **12**, 28818–28830.
- 94 Y. He, F. Hu, D. Liu, X. He, Q. Li, Y. Sui, J. Qi and Y. Wang, *J. Energy Storage*, 2023, **58**, 106377.
- 95 H. Wang, W. Li, D. Liu, G. Liu, X. An, J. Liu, C. Zhou, H. Zhang and G. Wang, *J. Electroanal. Chem.*, 2023, **930**, 117152.
- 96 H. Su, Q. Wang, J. Dai and W. Li, *J. Mater. Sci.: Mater. Electron.*, 2023, **34**, 403.
- 97 L. Xiao, J. Zhou, Z. Yu, H. Dong and Y. Chen, *J. Mater. Sci.: Mater. Electron.*, 2023, **34**, 474.
- 98 C. Yang, W. Li, X. Liu, X. Song, H. Li and L. Tan, *Molecules*, 2023, **28**, 3177.
- 99 J. Wang, Y. Huang, X. Du, S. Zhang and M. Zong, *Chem. Eng. J.*, 2023, **464**, 142741.
- 100 M. He, G. J. H. Melvin, M. Wang, W. Fan, J. Lin, X. Chen, K. Xu, C. Yuan, Y. Zhang, F. Zhang and Z. Wang, *J. Energy Storage*, 2023, **70**, 108055.
- 101 J. Liu, Y. N. Meng, D. Yu, C. Guo, L. Liu and X. Liu, *ChemistrySelect*, 2023, **8**, e202301597.
- 102 H. Xu, Q. Hu, T. Zhao, J. Zhu, Z. Lian and X. Jin, *Carbohydr. Polym.*, 2024, **326**, 121641.
- 103 D. Liu, J. Wang, M. Wang, R. Sultana, L. Cui, X. Zhang and Y. Han, *J. Electroanal. Chem.*, 2024, **961**, 118236.
- 104 B. Joshi, S. Kim, E. Samuel, J. Huh, M. S. Almoqli, K. N. Alharbi and S. S. Yoon, *J. Mater. Sci. Technol.*, 2024, **200**, 83–92.
- 105 S. Prabu, M. Vinu, K.-Y. Chiang and M. R. Pallavolu, *J. Colloid Interface Sci.*, 2024, **669**, 624–636.
- 106 L. Zheng, S. Gao, S. Yao, Y. Huang, S. Zhai, J. Hao, X. Fu, Q. An and Z. Xiao, *J. Colloid Interface Sci.*, 2024, **674**, 735–744.
- 107 Z. Li, J. Zhou, L. Xiao, Y. Wang, S. Zhou and Y. Chen, *J. Alloys Compd.*, 2024, **1003**, 175553.
- 108 F. Semerci and H. Esgin, *J. Electroanal. Chem.*, 2024, **970**, 118550.
- 109 L. Zhu, H.-Y. Xia, C.-Y. Zhang, Y. Geng, Z. Li, L. Shu, J.-R. Bai and Y.-P. Wen, *Int. J. Electrochem. Sci.*, 2024, **19**, 100752.
- 110 S. Rao, G. Ali, S. Khalid, R. Naz, F. J. Iftikhar and S. Bashir, *Inorg. Chem. Commun.*, 2024, **170**, 113211.
- 111 S. Y. Cheng, T. H. Wang, Z. Zhang, L. Li, Y. Qing and Y. Q. Wu, *Chem. Eng. Sci.*, 2025, **306**, 121234.

- 112 T.-Y. Chen, L.-Y. Lin, D.-S. Geng and P.-Y. Lee, *Electrochim. Acta*, 2021, **376**, 137986.
- 113 X.-Y. Yu, L. Yu and X. W. Lou, *Adv. Energy Mater.*, 2016, **6**, 1501333.
- 114 H. Hu, B. Y. Guan and X. W. Lou, *Chem*, 2016, **1**, 102–113.
- 115 X. Hou, Y. Zhang, Q. Dong, Y. Hong, Y. Liu, W. Wang, J. Shao, W. Si and X. Dong, *ACS Appl. Energy Mater.*, 2018, **1**, 3513–3520.
- 116 D. Guo, X. Song, L. Tan, H. Ma, H. Pang, X. Wang and L. Zhang, *ACS Appl. Mater. Interfaces*, 2018, **10**, 42621–42629.
- 117 S.-L. Jian, L.-Y. Hsiao, M.-H. Yeh and K.-C. Ho, *J. Mater. Chem. A*, 2019, **7**, 1479–1490.
- 118 H. Niu, Y. Zhang, Y. Liu, B. Luo, N. Xin and W. Shi, *J. Mater. Chem. A*, 2019, **7**, 8503–8509.
- 119 X. Wang, F. Huang, F. Rong, P. He, R. Que and S. P. Jiang, *J. Mater. Chem. A*, 2019, **7**, 12018–12028.
- 120 G. Liu, H. Zhang, J. Li, Y. Liu and M. Wang, *J. Mater. Sci.*, 2019, **54**, 9666–9678.
- 121 H. Jia, Z. Wang, X. Zheng, Y. Cai, J. Lin, H. Liang, J. Qi, J. Cao, J. Feng and W. Fei, *Electrochim. Acta*, 2019, **312**, 54–61.
- 122 Z. Yang, Q. Ma, L. Han and K. Tao, *Inorg. Chem. Front.*, 2019, **6**, 2178–2184.
- 123 X. Guan, M. Huang, L. Yang, G. Wang and X. Guan, *Chem. Eng. J.*, 2019, **372**, 151–162.
- 124 X. Liu, L. Ye, Y. Du and L. Zhao, *Mater. Lett.*, 2020, **258**, 126812.
- 125 P. Cai, T. Liu, L. Zhang, B. Cheng and J. Yu, *Appl. Surf. Sci.*, 2020, **504**, 144501.
- 126 Y. Zhao, C. Huang, Y. He, X. Wu, R. Ge, X. Zu, S. Li and L. Qiao, *J. Power Sources*, 2020, **456**, 228023.
- 127 S. Hou, Y. Lian, Y. Bai, Q. Zhou, C. Ban, Z. Wang, J. Zhao and H. Zhang, *Electrochim. Acta*, 2020, **341**, 136053.
- 128 X. Wei, H. Wu and L. Li, *J. Taiwan Inst. Chem. Eng.*, 2020, **111**, 198–204.
- 129 V. Shrivastav, S. Sundriyal, P. Goel, V. Shrivastav, U. K. Tiwari and A. Deep, *Electrochim. Acta*, 2020, **345**, 136194.
- 130 X. Li, Y. Fu, H. Ma, X. Liu, L. Li, J. Ma, C. Liang, M. Jin, Y. Hua and C. Wang, *J. Chem. Sci.*, 2020, **132**, 101.
- 131 A. M. Mohamed, A. O. A. El Naga, T. Zaki, H. B. Hassan and N. K. Allam, *ACS Appl. Energy Mater.*, 2020, **3**, 8064–8074.
- 132 M. Xu, H. Guo, T. Zhang, J. Zhang, X. Wang and W. Yang, *J. Energy Storage*, 2021, **35**, 102303.
- 133 C.-L. Wu and D.-H. Chen, *J. Alloys Compd.*, 2021, **872**, 159702.
- 134 X. Zhao, Q. Ma, K. Tao and L. Han, *ACS Appl. Energy Mater.*, 2021, **4**, 4199–4207.
- 135 A. M. Zardkhoshoui, B. Ameri and S. S. H. Davarani, *Chem. Eng. J.*, 2021, **422**, 129953.
- 136 Z. Peng, H. Zou, W. Yang, Z. Feng and S. Chen, *J. Energy Storage*, 2021, **40**, 102697.
- 137 C. Ruan, D. Zhu, J. Qi, Q. Meng, F. Wei, Y. Ren, Y. Sui and H. Zhang, *Surf. Interfaces*, 2021, **25**, 101274.
- 138 Z. Li, Y. Huang, Z. Zhang, J. Wang, X. Han, G. Zhang and Y. Li, *J. Colloid Interface Sci.*, 2021, **604**, 340–349.
- 139 L. Chen, J. Wan, L. Fan, Y. Wei and J. Zou, *Appl. Surf. Sci.*, 2021, **570**, 151174.
- 140 J. Zhou, Y. Wang, J. Zhou, K. Chen and L. Han, *Dalton Trans.*, 2021, **50**, 15129–15139.
- 141 E. S. Goda, A. U. Rehman, B. Pandit, A. A.-S. Eissa, S. E. Hong and K. R. Yoon, *Chem. Eng. J.*, 2022, **428**, 132470.
- 142 L. Ma, Y. Miao, M. Zhang, Y. Sui, J. Qi, F. Wei, Q. Meng, L. Pang, Y. Ren, B. Xiao, X. Xue and Z. Sun, *J. Mater. Sci.: Mater. Electron.*, 2022, **33**, 1930–1941.
- 143 S. Yang, Z. Hao, S. Zhang, Y. Gao, X. Li, J. Peng, L. Li and X. Li, *ACS Appl. Energy Mater.*, 2022, **5**, 1436–1446.
- 144 L. Luo, Y. Zhou, W. Yan, G. Du, M. Fan and W. Zhao, *J. Colloid Interface Sci.*, 2022, **615**, 282–292.
- 145 X. Wu, C. Wang, Z. Wang, Y. Qin and Y. Kong, *Synth. Met.*, 2022, **286**, 117034.
- 146 J. Pan, S. Li, L. Zhang, T. Yu, F. Li, W. Zhang, J. Wang, D. Zhang, Y. Yu and X. Li, *J. Energy Storage*, 2022, **47**, 103550.
- 147 X. Wang, W. Li, Y. Xue, J. Liu, Y. Yue, C. Zhou, K. Zhu, D. Cao, Y. Chen and G. Wang, *J. Energy Storage*, 2022, **50**, 104220.
- 148 Y. Li, H. Wang, T. Shu, J. Yuan, G. Lu, B. Lin, Z. Gao, F. Wei, C. Ma, J. Qi and Y. Sui, *J. Energy Storage*, 2022, **51**, 104299.
- 149 S. Zhang, K. Wang, H. Chen, H. Liu, L. Yang, Y. Chen and H. Li, *Carbon*, 2022, **194**, 10–22.
- 150 X. Liu, X. Zhang, Q. Yin, R. Liu, N. Liu, J. Hu, F. Shen and X. Zhu, *CrystEngComm*, 2022, **24**, 3621–3629.
- 151 S. Li, Y. Yang, Z. Hu, S. Li, F. Ding, X. Xiao, P. Si and J. Ulstrup, *Electrochim. Acta*, 2022, **424**, 140604.
- 152 Z. Xue, K. Tao and L. Han, *Appl. Surf. Sci.*, 2022, **600**, 154076.
- 153 J.-Q. Qi, M.-Y. Huang, C.-Y. Ruan, D.-D. Zhu, L. Zhu, F.-X. Wei, Y.-W. Sui and Q.-K. Meng, *Rare Met.*, 2022, **41**, 4116–4126.
- 154 W. Zhang, Z. Shi, H. Wang, S. Sun and S. Yao, *J. Alloys Compd.*, 2022, **919**, 165828.
- 155 Q. Chen, Z. Huang, W. Zhao, K. Tao, G. Li and L. Han, *J. Alloys Compd.*, 2023, **937**, 168279.
- 156 C. Qu, J. Cao, Y. Chen, M. Wei, H. Fan, X. Liu, X. Li, Q. Wu, B. Feng and L. Yang, *Int. J. Hydrogen Energy*, 2023, **48**, 648–661.
- 157 A. Mohammadi Zardkhoshoui, B. Ameri and S. Saeed Hosseiny Davarani, *Chem. Eng. J.*, 2023, **470**, 144132.
- 158 F. Wei, Y. Li, H. Wang, T. Shu, J. Yuan, G. Lu, B. Lin, Z. Gao, Q. Wang, J. Qi and Y. Sui, *J. Energy Storage*, 2023, **60**, 106551.
- 159 G. Wang, Z. Xu, Z. Li, Y. Ding, R. Ge, M. Xiang, G. Wang and Z. Yan, *Electrochim. Acta*, 2023, **443**, 141980.
- 160 X. Wang, Y. Xu, X. An, E. Xu, J. Liu, C. Zhou, W. Li, Y. Chen and G. Wang, *Int. J. Hydrogen Energy*, 2023, **48**, 9945–9956.



- 161 S. Wu, X. Xu, X. Sun, S. Zhou, C. Liu, P. Zhang, S. Fu, H. Zhang, S. Pang, X. Wang and Q. Yang, *Diamond Relat. Mater.*, 2023, **136**, 109946.
- 162 P. A. K. Reddy, H. Han, K. C. Kim and S. Bae, *Chem. Eng. J.*, 2023, **471**, 144608.
- 163 F. Cao, X.-R. Shi, P. Wang, W. Zhao, M. Huang, J. Hu, S. Xu and G. Zhao, *Vacuum*, 2023, **216**, 112461.
- 164 S. K. Kaverlavani, S. E. Moosavifard, Y. K. Mishra, F. Gity, M. Sadeghipari, S. Y. Hosseini, R. A. Pour and M. Hajmirzaheydarali, *J. Energy Storage*, 2023, **72**, 108793.
- 165 Y. Li, Z. Qiu, M. Qu, Y. Wang, H. Wang and J. Jiang, *J. Energy Storage*, 2023, **73**, 108997.
- 166 J. Chen, X. Sun, W. Kong, Q. Yu, Y. Long, T. Zhou, C. Hu, Y. Dai, J. Gong, L. Pu, H. Zhang and W. Wang, *J. Energy Storage*, 2023, **73**, 109164.
- 167 M. Yan, W. Yao, R. K. Kankala, M. Xiao, J. Ye, Y. Huang, Y. Yang and X. Zhang, *Appl. Surf. Sci.*, 2024, **645**, 158757.
- 168 S. Mohapatra, H. T. Das, B. Chandra Tripathy and N. Das, *ACS Appl. Nano Mater.*, 2024, **7**, 3249–3259.
- 169 J. Xu, H. Guo, M. Wang, Y. Hao, J. Tian, H. Ren, Y. Liu, B. Ren and W. Yang, *Dalton Trans.*, 2024, **53**, 4479–4491.
- 170 B. Li, L. Zhang, Z. Zhao, Y. Zou, B. Chen, X. Fu, F. Wang, S. Long, W. Guo, J. Liang and M. Ye, *Chem. Eng. J.*, 2024, **487**, 150730.
- 171 M. Raza, N. Iqbal, T. Noor, I. Shaukat, R. Ahmad, J. Gao and Z. A. Ghazi, *Mater. Res. Bull.*, 2024, **176**, 112830.
- 172 M. Zhu, Y. Yang, X. Zhang, Y. Liang and J. Tang, *Appl. Organomet. Chem.*, 2024, **38**, e7533.
- 173 J. Qi, H. Duan, Z. Peng, J. Wang, B. Ma, Z. Yuan and H. Zhang, *Energy Fuels*, 2024, **38**, 13379–13389.
- 174 S. Saha, M. Kandasamy, D. Potphode, C. S. Sharma, B. Chakraborty, N. Hameed and N. Salim, *J. Energy Storage*, 2024, **99**, 113294.
- 175 S. Yang, M. Xiao, M. Xiao, W. Zhang, X. Niu, X. Du, X. Hui, Z. Song and X. Gao, *J. Power Sources*, 2024, **623**, 235424.
- 176 S. Ramesh, I. Rabani, K. Senthilkumar, Y. Haldorai, M. Selvaraj, Y. S. Seo, J. H. Kim and H. S. Kim, *J. Electroanal. Chem.*, 2024, **974**, 118749.
- 177 X. B. Mao, H. T. Guan, J. F. Zhou, W. W. Zhou, X. B. Shi, X. Xu and Y. F. Gao, *J. Energy Storage*, 2025, **105**, 114751.
- 178 S. Liu, X. J. Liu, K. Chen and C. G. Xue, *Mater. Lett.*, 2025, **382**, 137930.
- 179 Y. F. Mo, T. Feng, C. H. Zhang, Z. S. Zhang, P. Zhao, Z. H. Liu and G. Liu, *J. Energy Storage*, 2025, **108**, 115136.
- 180 C. Hao, J. Z. Tan, Z. J. Lv, M. J. Jiang, C. H. Ni, Y. R. Shen and X. H. Wang, *J. Colloid Interface Sci.*, 2025, **684**, 262–276.
- 181 B. Li, J. Li, P. T. Li, N. Zhang, H. S. Shang and B. Zhang, *J. Alloys Compd.*, 2025, **1017**, 179128.
- 182 Y.-X. Lai, R.-Y. Li and C. Young, *ChemPhysChem*, 2025, e202400910, DOI: [10.1002/cphc.202400910](https://doi.org/10.1002/cphc.202400910).
- 183 R. Ma, Z. Chen, D. Zhao, X. Zhang, J. Zhuo, Y. Yin, X. Wang, G. Yang and F. Yi, *J. Mater. Chem. A*, 2021, **9**, 11501–11529.
- 184 L.-P. Lv, C. Zhi, Y. Gao, X. Yin, Y. Hu, D. Crespy and Y. Wang, *Nanoscale*, 2019, **11**, 13996–14009.
- 185 L. C. Tan, D. X. Guo, D. W. Chu, J. Yu, L. L. Zhang, J. Yu and J. Wang, *J. Electroanal. Chem.*, 2019, **851**, 6.
- 186 G. Qu, X. Zhang, G. Xiang, Y. Wei, J. Yin, Z. Wang, X. Zhang and X. Xu, *Chin. Chem. Lett.*, 2020, **31**, 2007–2012.
- 187 Q. Zong, Y. L. Zhu, Q. Q. Wang, H. Yang, Q. L. Zhang, J. H. Zhan and W. Du, *Chem. Eng. J.*, 2020, **392**, 123664.
- 188 L. Sun, Y. Liu, M. Yan, Q. J. Yang, X. Y. Liu and W. D. Shi, *Chem. Eng. J.*, 2022, **431**, 133472.
- 189 C. Wang, W. Zheng, Z. Wang, Z.-Z. Yin, Y. Qin and Y. Kong, *J. Electroanal. Chem.*, 2021, **901**, 115759.
- 190 H. Wang, T. Shu, J. Yuan, Y. Li, B. Lin, F. Wei, J. Qi and Y. Sui, *Colloids Surf., A*, 2022, **633**, 127789.
- 191 C. Wang, Z. Wang, D. Wu, W. Cai, Y. Qin and Y. Kong, *J. Electroanal. Chem.*, 2022, **905**, 115976.
- 192 M. Amiri, S. S. H. Davarani, S. E. Moosavifard and Y.-Q. Fu, *J. Colloid Interface Sci.*, 2022, **616**, 141–151.
- 193 Z. Andikaey, A. A. Ensafi, B. Rezaei and J.-S. Hu, *Electrochim. Acta*, 2022, **417**, 140388.
- 194 Y. Yang, X. Huang, C. Sheng, Y. Pan, Y. Huang and X. Wang, *J. Alloys Compd.*, 2022, **920**, 165908.
- 195 P. Salehan, A. A. Ensafi, Z. Andikaey and B. Rezaei, *Sci. Rep.*, 2023, **13**, 2070.
- 196 J. Fan, Z. Peng, M. Chen, W. Yang, H. Zou and S. Chen, *Dalton Trans.*, 2023, **52**, 6782–6790.
- 197 X. Wang, C. Qian, T. Zou, H. Ding, F. Jiang, H. Li, H. Cao, Z. Fang, Y. Xu, J. Liu and Y. Zhu, *J. Electroanal. Chem.*, 2023, **943**, 117612.
- 198 I. Shaukat, N. Iqbal, T. Noor, M. Raza and R. Ahmad, *Energy Fuels*, 2023, **37**, 16150–16159.
- 199 L. Sun, Y. Liu, B. F. Luo, F. R. Yan, X. Y. Liu, F. F. Zhu and W. D. Shi, *Chem. Eng. J.*, 2023, **454**, 140088.
- 200 Q. Zhang, S. Liu, J. Huang, H. Fu, Q. Fan, H. Zong, H. Guo and A. Zhang, *J. Colloid Interface Sci.*, 2024, **655**, 273–285.
- 201 H. Guo, H. Ren, J. Tian, J. Xu, Y. Hao, L. Peng, Y. Liu and W. Yang, *J. Alloys Compd.*, 2024, **1000**, 175107.
- 202 W. Dong, X. Y. Li, E. R. Ye, X. C. Xu, X. Zhang, F. Yang, D. Shen, X. D. Hong and S. B. Yang, *J. Energy Storage*, 2025, **114**, 115870.
- 203 L. Hu, L. Li, Y. Y. Zhang, X. H. Tan, H. Yang, X. M. Lin and Y. X. Tong, *J. Mater. Sci. Technol.*, 2022, **127**, 124–132.
- 204 T. Kshetri, T. I. Singh, Y. S. Lee, D. D. Khumujam, N. H. Kim and J. H. Lee, *Composites, Part B*, 2021, **211**, 108624.